Chapter 4

Hydriding / Dehydriding Studies on Magnesium Based Compositions

Abstract

This chapter presents results obtained on the ternary/quaternary Magnesium based alloy compositions studied. Pure Mg (without milling) shows reversible 0.43 mass% of H_2 *uptake at a charging temperature of 303 ℃. After 40 h milling, pure Mg shows 3.81 mass% of reversible* H_2 *uptake at a charging temperature of 303 ℃. The ternary Mg–V–Ni alloy compositions show maximum 5.02 mass% of reversible* H_2 *at a charging temperature of 265 ℃. It is also seen that 95% of hydrogen is absorbed within first 3 to 5 minutes. The ternary Mg–Pd–Ni alloy compositions show maximum 3.98 mass% of reversible* H_2 *at a charging temperature of 202 ºC and pressure of 10 bar. The quaternary Mg–Zr–Mn–Ni alloy compositions indicate fast kinetics, with 95% of hydrogen absorbed within the first 6 to 10 minutes. These compositions also indicate very high hydrogen storage capacity greater than 7 mass% of hydrogen stored reversibly, at a charging temperature of 201 ℃. The reaction kinetics model of each of the systems studied is also presented. Further, the formation enthalpy and entropy of each system is computed using Van't Hoff relationship and also by DSC technique.*

4.1 Introduction

Mg based alloy compositions using a combination of metal alloying (addition of V, Pd, Fe, Zr, Mn and Ni) have been synthesized by high energy planetary ball milling for hydrogen storage application. The major role of catalysts (V, Pd, Fe, Zr, Mn and Ni) is to improve absorption temperature and kinetics [1 – 11]. This chapter deals with the hydriding / dehydriding studies on following Mg based alloy compositions:

(i) Mg–V–Ni alloy compositions
(ii) Mg–Pd–Ni alloy compositions
(iii) Mg–Zr–Mn–Ni alloy compositions

Properties and preparation of alloy compositions have been discussed in chapter 3. The detailed characterization and kinetics studies of the developed ternary/quaternary Mg based alloy compositions are presented in this chapter.

4.2 Preliminary Study on Magnesium

4.2.1 Pure Magnesium

Micrograph showing the morphology of pure Mg is shown in Fig. 4.1. The mean particle size of Magnesium particles is measured as 470 ± 159 µm without milled and after 40 h milling, it is obtained as 22.6 ± 8.6 µm (by lineal analysis of SEM micrographs).

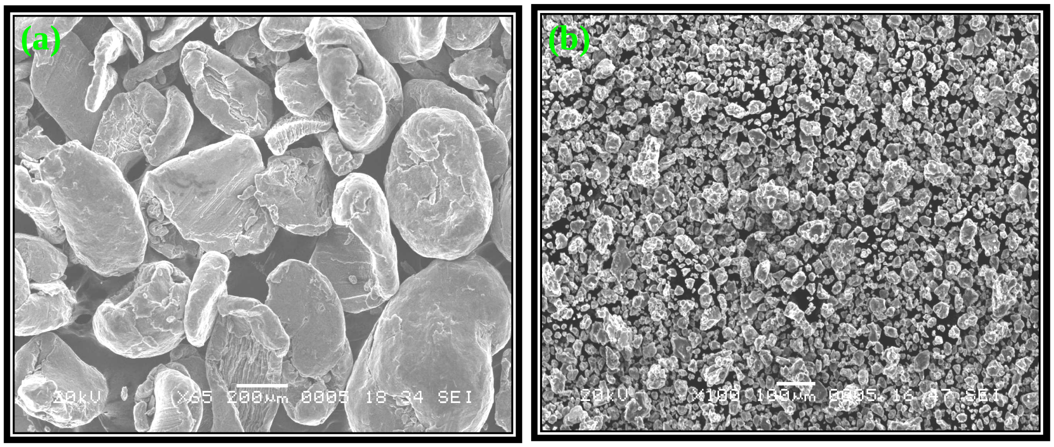

Fig. 4.1: SEM micrograph of pure Mg: (a) Without milling and (b) With 40 h milling

EDS analysis is conducted in SEI (secondary electron image) mode at accelerating voltage of 20 kV on pure Mg. Results indicate that 99.94 at% Mg and only 0.06 at% Cr is presence. An EDS spectrum of the pure Mg is shown in Fig. 4.2.

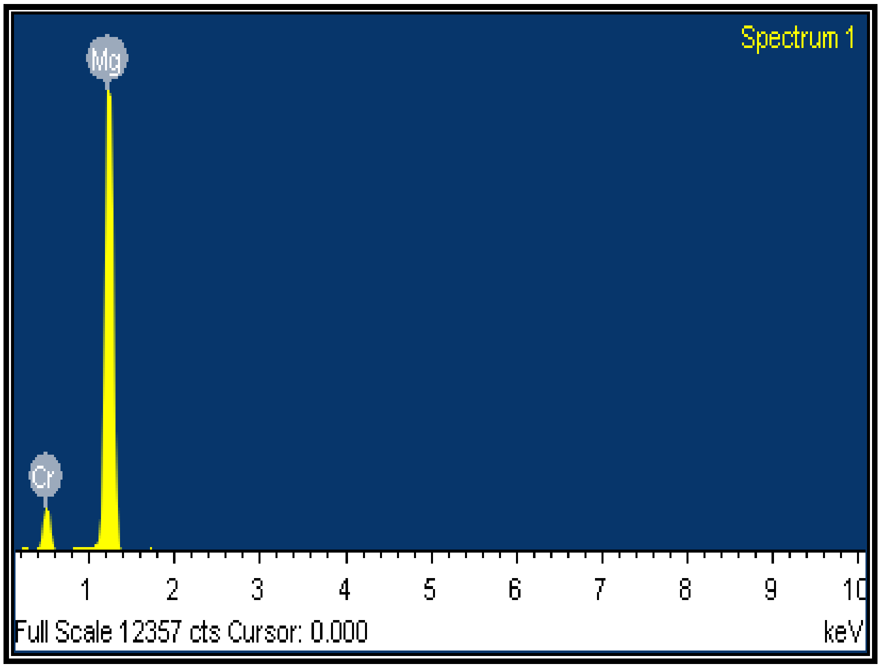

Fig. 4.2: EDS spectra of pure Mg

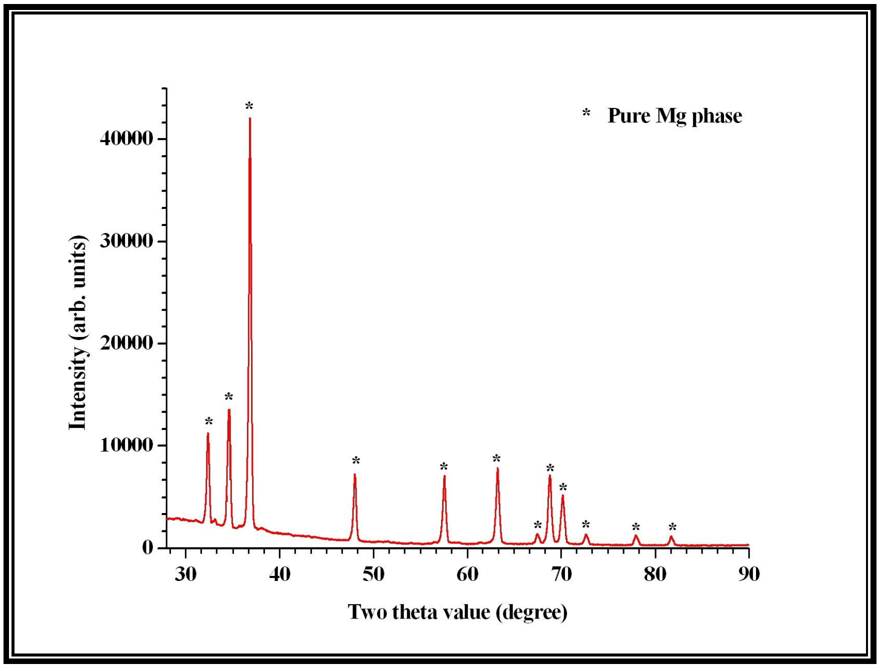

Fig. 4.3: XRD spectra of pure Mg

The XRD spectrum of the pure Mg is presented in Fig. 4.3. All the predominant peaks corresponding to Mg phase are seen. The various diffraction peaks could be accurately indexed and correlated with Mg phase. The Bravais lattice system of this phase being hexagonal (cell parameters, a: 3.2022 Å & c: 5.1991 Å). Further, the mean crystallite/grain size of this phase is obtained as 36.5 nm (determined using the Scherrer equation).

Fig. 4.4(a) shows the kinetics of pure Mg without milling. Note that the hydrogen up-take capacity of the pure Mg is very low (nearly, 60 to 70 minutes) and reversibly only 0.43 mass % of H_2 is up-taken at charging temperature of 303 °C and discharging temperature of 365 °C. Similarly, Fig. 4.4(b) shows the hydriding / dehydriding reaction kinetics of pure Mg after 40 h milling. This graph clearly indicates rapid hydrogen up-take / release capacity (within first 10 to 15 minutes). The maximum reversible hydrogen uptake of 3.81 mass % is obtained at charging temperature of 303 °C and discharging temperature of 365 °C.

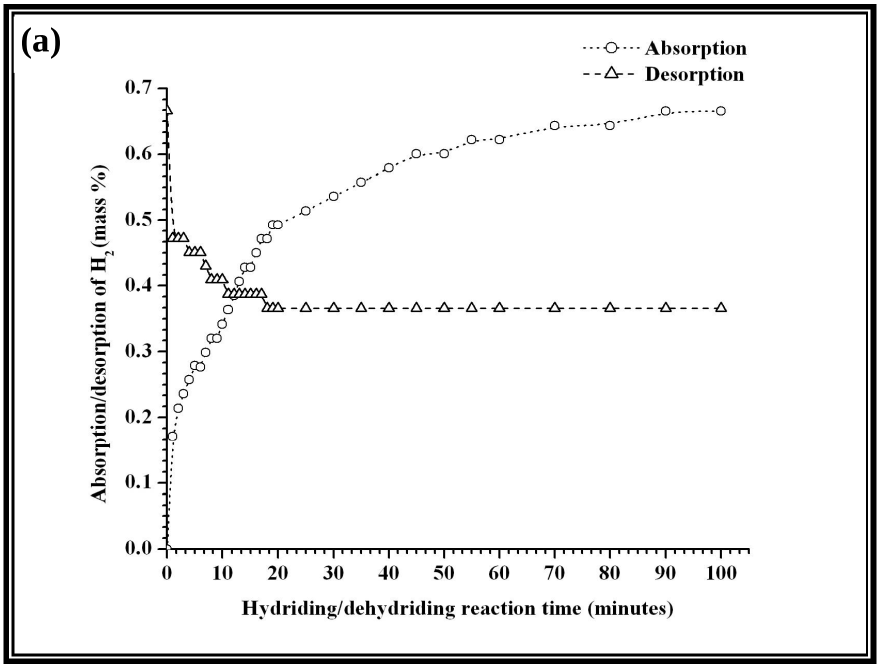

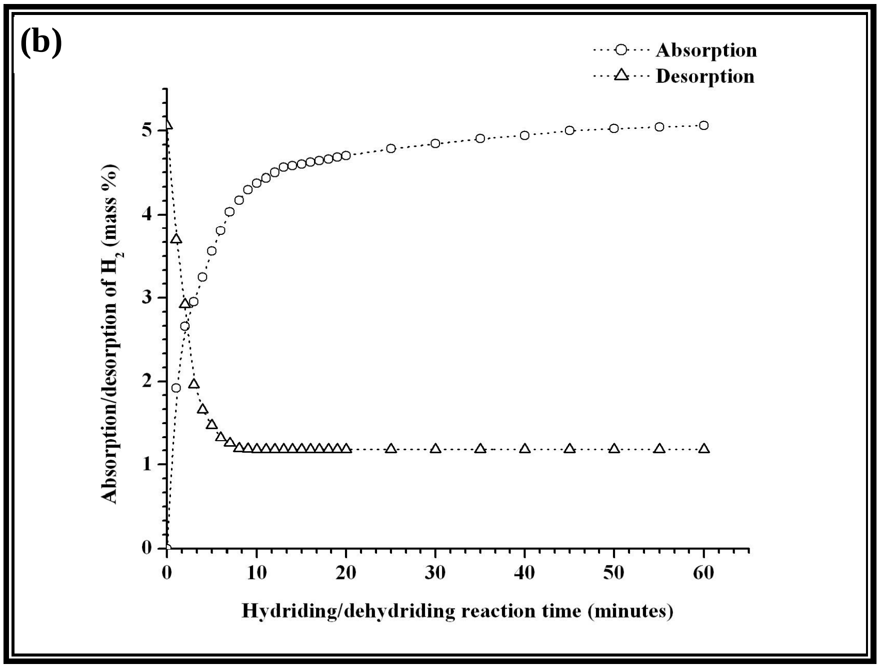

Fig. 4.4: Kinetics curve of pure Mg at 303 °C charging and 365 °C discharging temperatures: (a) Without milling and (b) With 40 h milling

4.2.2 Mg_2Ni Alloy Composition

Micrograph showing the morphology of pure Ni and synthesized Mg_2Ni alloy is shown in Fig. 4.5. The mean particle size of Nickel is measured as 296 ± 66 μm by lineal analysis of SEM micrographs. The mean particle size of Mg_2Ni phase is measured as 2.94 ± 0.8 μm.

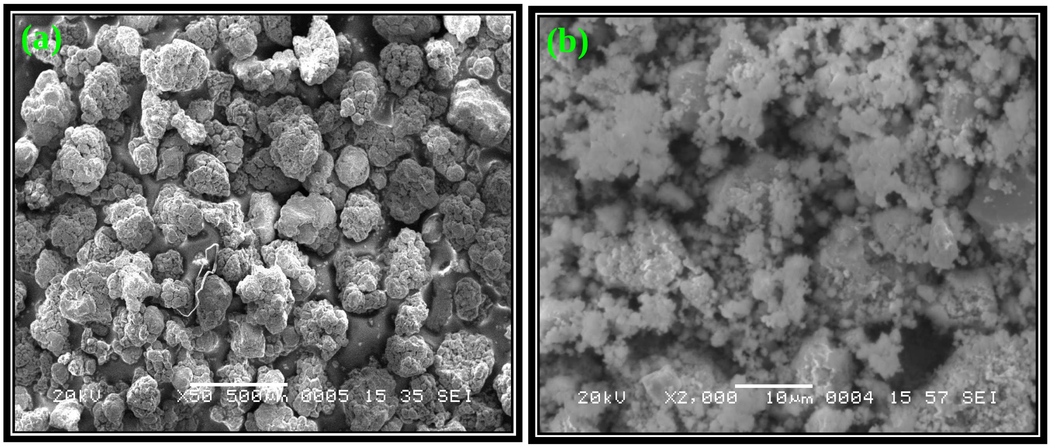

Fig. 4.5: SEM micrographs: (a) Pure Ni without milling and (b) Mg_2Ni alloy at 40 h milling

EDS spectrum of this alloy is shown in Fig. 4.6. Results indicate the synthesized alloy contains 70.58 at% Magnesium and 29.42 at% Nickel, which are closely matched with targeted compositions (66.67 at% for Mg and 33.33 at% for Ni).

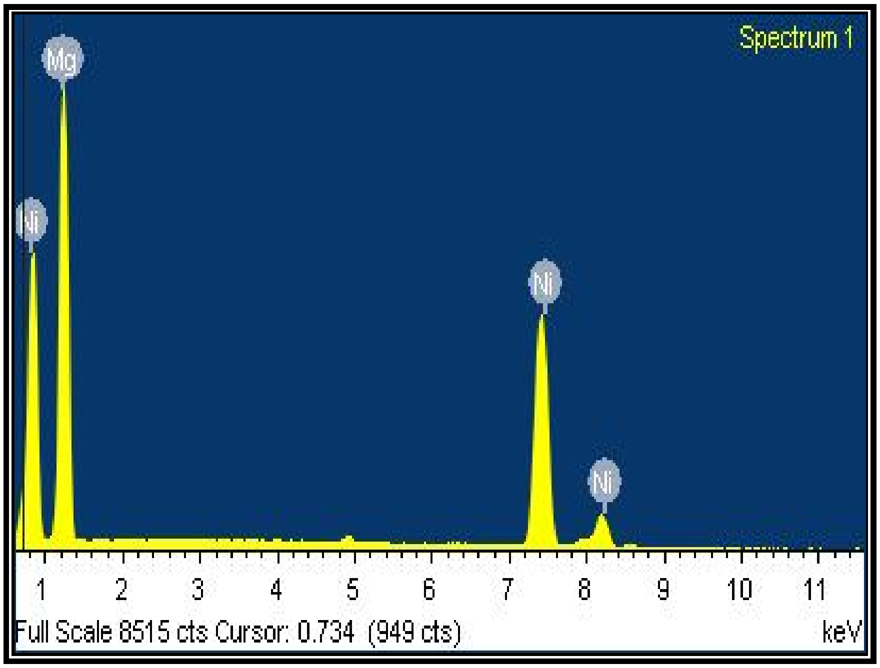

Fig. 4.6: EDS spectra of Mg_2Ni alloy

The XRD spectrum of Mg_2Ni alloy showing a plot of intensity in arbitrary units as a function of diffraction angle, 2θ, is presented in Fig. 4.7. Predominant peaks corresponding to Mg_2Ni, Ni and MgO·NiO are seen. These phases are identified by comparing experimental XRD patterns with standard ICDD (International Centre for Diffraction Data) cards. The diffraction peaks could be accurately indexed and correlated with Mg_2Ni phase, Ni phase and MgO·NiO phase. The Bravais lattice system of these phases being hexagonal (cell parameters, a: 5.2100 Å & c: 13.2300 Å), cubic (cell parameter a: 3.5175 Å) and cubic (cell parameter a: 4.2110 Å), respectively. Further, the mean crystallite/grain size of these phases was obtained as 8.8 nm for Mg_2Ni, 12.4 nm for Ni and 8.3 nm for MgO·NiO phase.

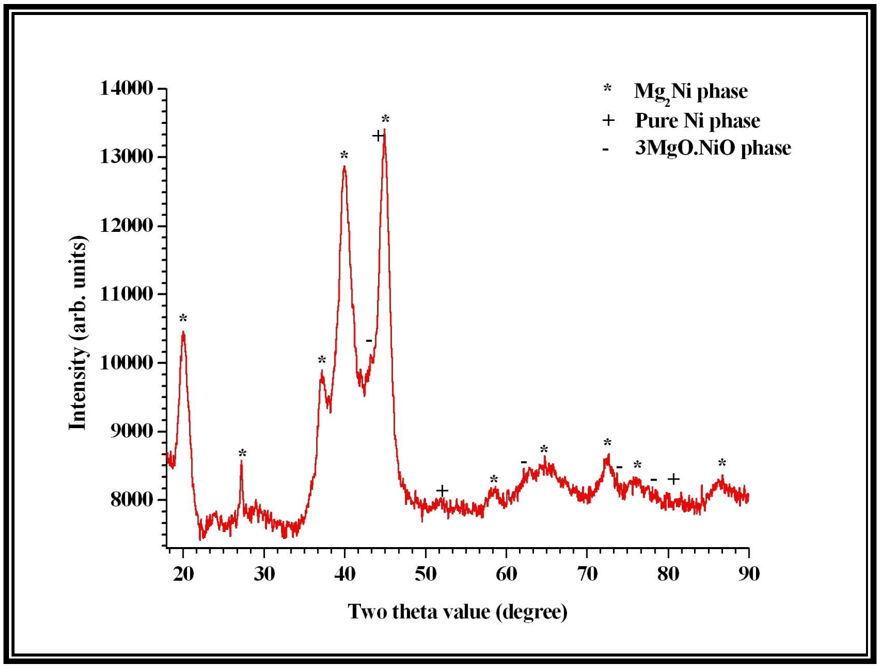

Fig. 4.7: XRD spectra of Mg_2Ni alloy

Fig. 4.8(a) shows the charging kinetics of 40 h milled Mg_2Ni alloy. The hydrogen up-take capacity of this alloy is seen to be rapid (within first 10 minutes). The maximum hydrogen up take is 3.31 mass % at 210 °C. Fig. 4.8(b) shows the dehydriding reaction kinetics of Mg_2Ni alloy (after 40 h milling) for different discharging temperatures. This graph clearly indicates that the hydrogen release capacity is increased with discharging temperature. Desorption of hydrogen is started at 201 ºC and the maximum hydrogen release is 2.28 mass % at discharging temperature of 375 °C [12]. The above results are also in line with the work of Dehouche et al. (1999) [13].

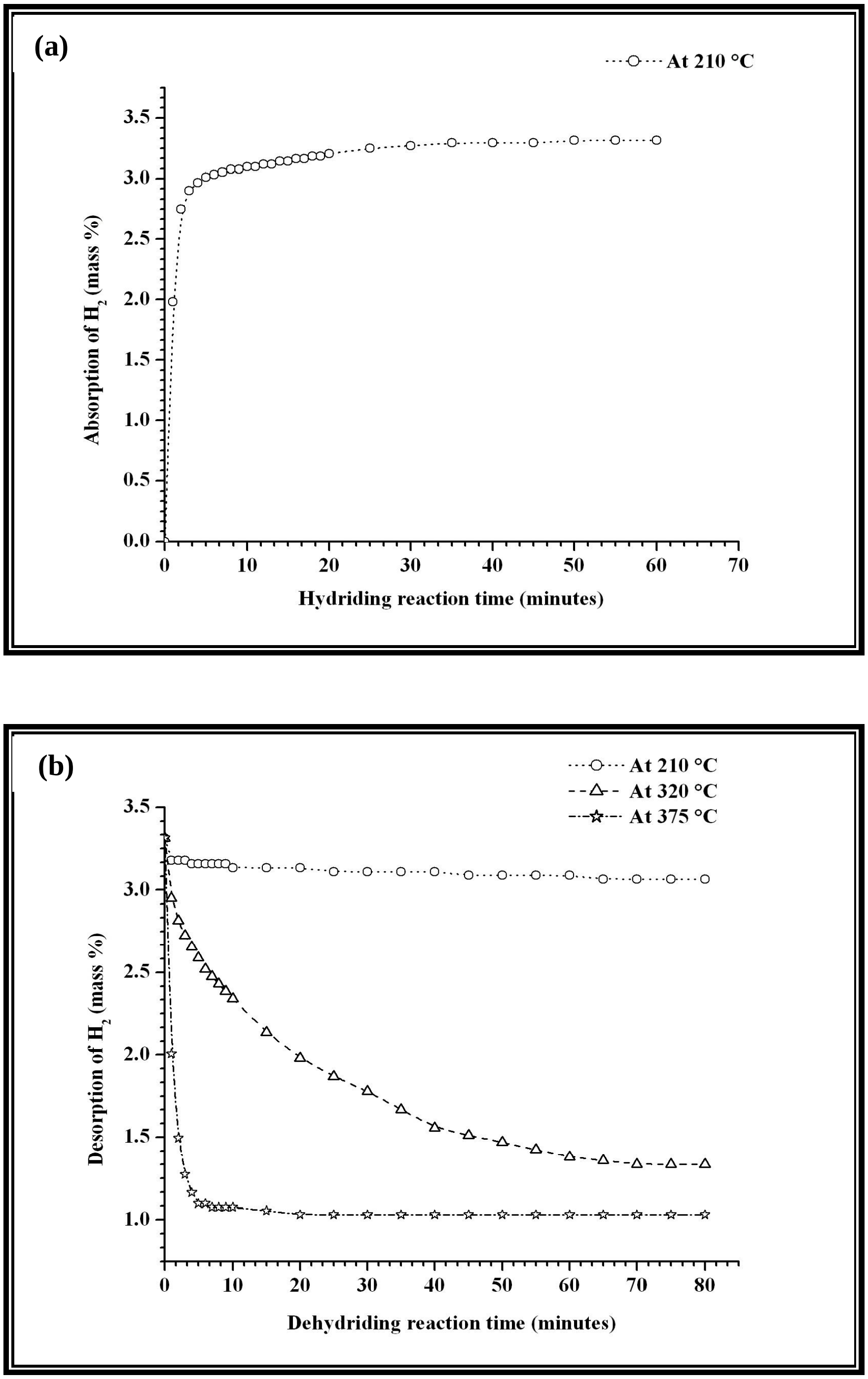

Fig. 4.8: Reaction kinetics curve of Mg_2Ni alloy: (a) Charging kinetics and (b) Discharging kinetics

4.2.3 Mg–Fe–Mn–Ni Composition

Backscattered micrograph showing the morphology of the synthesized Mg–Ni–Fe–Mn composition is shown in Fig. 4.9. This micrograph indicates the brighter particles to be elemental catalyst species (Fe, Mn and Ni). The mean particle size of Magnesium is measured as 9 ± 1 μm and mean particle size of the satellite catalyst particles is obtained as 1.25 ± 0.3 μm by lineal analysis of SEM micrographs. EDS analysis is conducted in SEI (secondary electron image) mode at accelerating voltage of 20 kV and 100 X magnification on the synthesized alloy. Results indicate that the synthesized alloy has 84.24 wt% Magnesium, 4.87 wt% Iron, 7.04 wt% Manganese and 3.85 wt% Nickel, which closely matched with target compositions (80 at% for Mg, 5 at% for Fe, 10 at% for Mn and 5 at% for Ni). A typical EDS spectrum of the synthesized alloy is shown in Fig. 4.10.

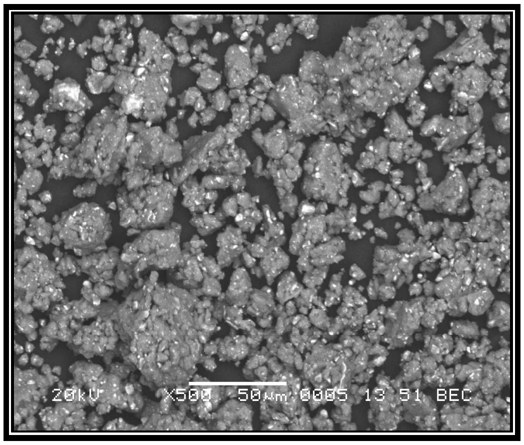

Fig. 4.9: SEM micrograph of Mg–Fe–Mn–Ni alloy composition

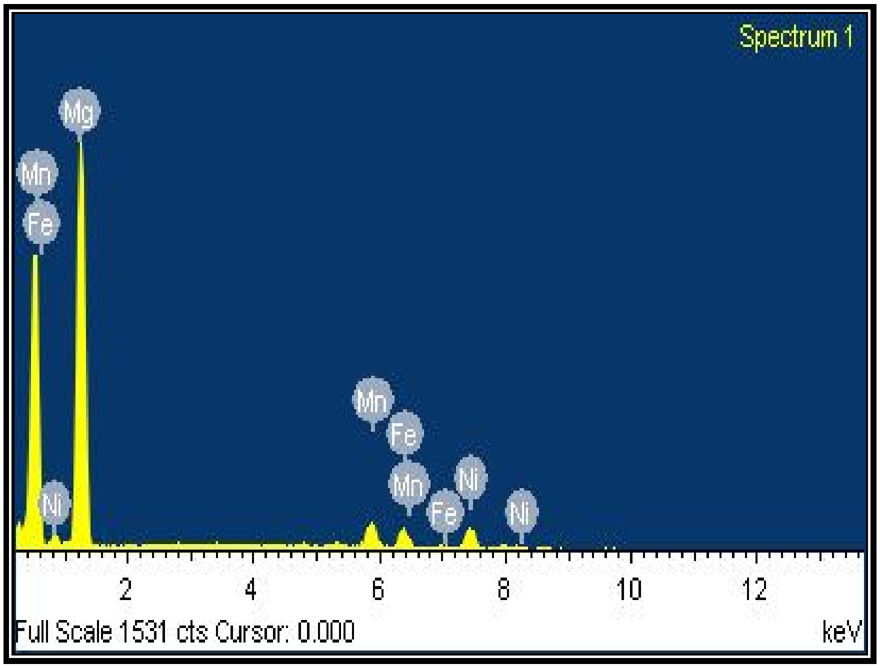

Fig. 4.10: EDS spectra of Mg–Fe–Mn–Ni alloy composition

The XRD spectrum of the Mg–Ni–Fe–Mn alloy showing a plot of intensity in arbitrary units as a function of diffraction angle, 2θ, is presented in Fig. 4.11. Predominant peaks corresponding to Mg, Ni and Fe, along with a peak corresponding to the phase, Fe19Mn are seen. These phases are identified by comparing experimental XRD patterns with standard ICDD (International Centre for Diffraction Data) cards. The diffraction peaks could be accurately indexed and correlated with Mg phase, Ni phase, Iron-Manganese phase and Iron phase. The Bravais lattice system of these phases being hexagonal (cell parameters, a: 3.2094 Å & c: 5.2102 Å), cubic (cell parameter a: 3.5240 Å), cubic (cell parameter a: 2.8708 Å) and cubic (cell parameter a: 2.8670 Å), respectively. Further, the mean crystallite/grain size of these phases was obtained as 21.7 nm for Mg, 23.3 nm for Ni, 26.6 nm for Fe19Mn and 8.1 nm for Fe phase (determined using the Scherrer equation). Hydride samples were also subjected to XRD analysis (see the Fig. 4.11(b)). This analysis indicated the presence of MgH_2 as the hydride forming phase which has tetragonal Bravias lattice system with cell parameter a: 4.5170 Å & c: 3.0205 Å.

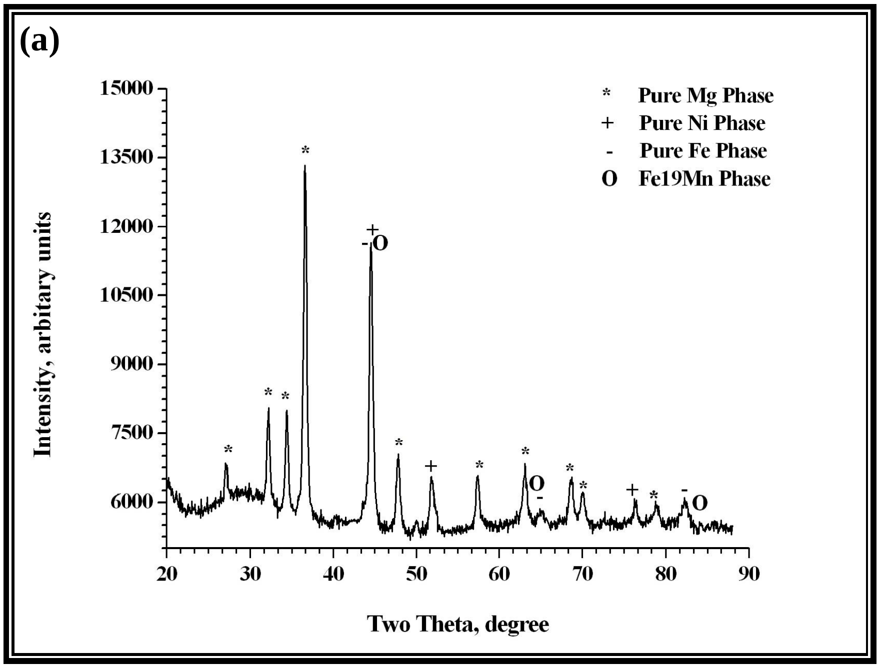

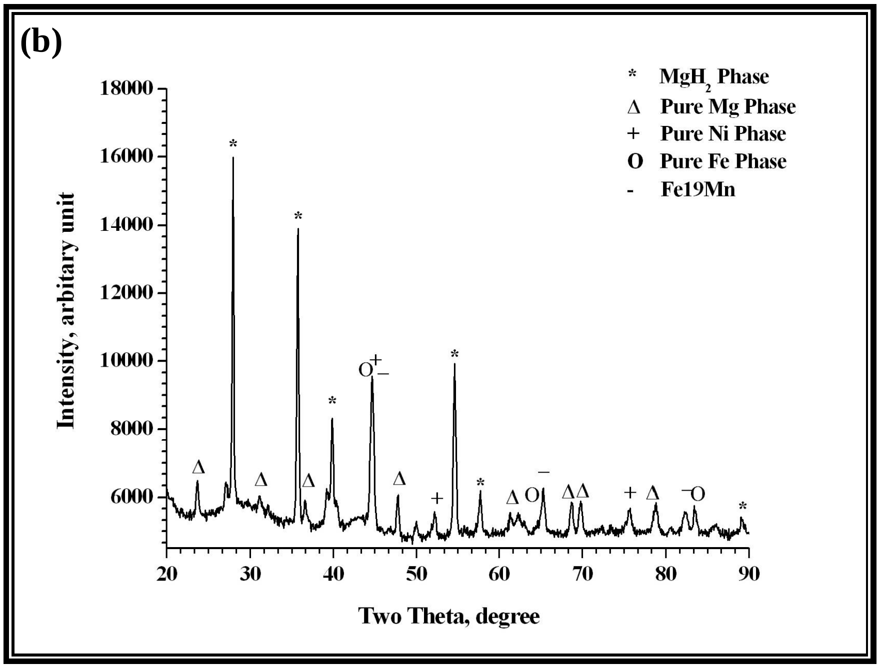

Fig. 4.11: XRD spectra of Mg–Fe–Mn–Ni alloy composition: (a) Unhydrided alloy composition and (b) Hydrided alloy composition

In Fig. 4.12 (a) and (b), the charging and discharging kinetics are presented, respectively, of the synthesized alloy at various temperatures. Specifically, Fig. 4.12(a) presents the kinetics plots of the hydriding reaction of the synthesized alloy at an initial hydrogen charging pressure of 30 bar. Note that as the hydriding temperature is increased, the maximum hydrogen absorption capacity increases up to a temperature of 325 ºC. However, beyond 325 ºC, the hydrogen up-take dramatically decreases. This graph clearly shows that 95% of hydrogen is absorbed within the first 3 to 5 minutes. This indicates reasonably high hydriding reaction rate.

In Fig. 4.12(b), dehydriding of hydrogen at different temperatures is presented, which shows that increase of temperature results in a monotonic increase of hydrogen released along with the dehydriding rate. This shows that 70%–75% of hydrogen is desorbed within 8 to 10 minutes for the synthesized alloy at 372 ºC. This again indicates fast dehydriding rate due to Mn catalyst addition, because Mn facilitates the discharging process as reported by Majchrzycki et al (2004) [14] and Spassov et al (2005) [15]. In general, the enhanced reaction kinetics appears to be associated with the catalytic effect of Ni, Fe and Mn [16].

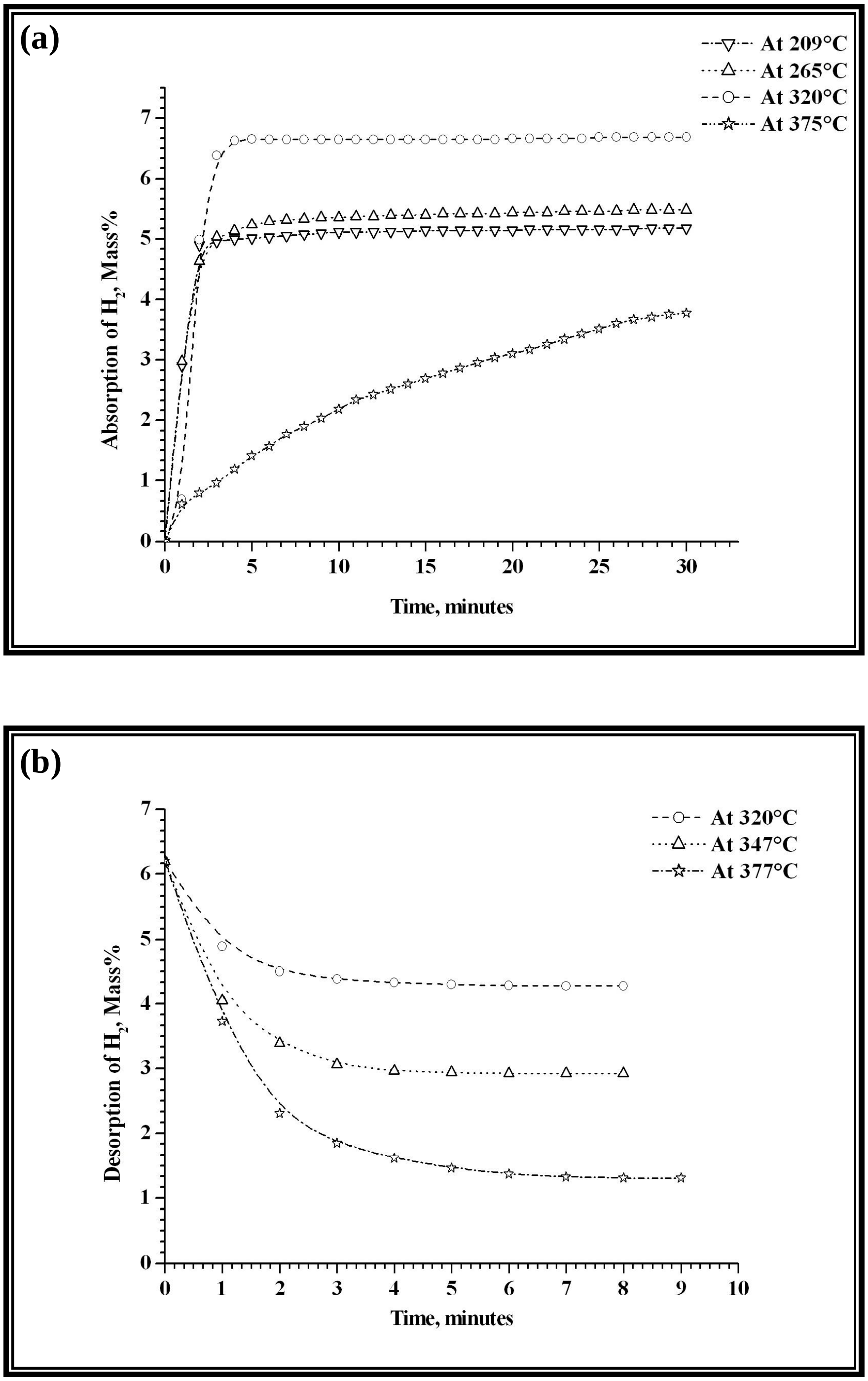

Fig. 4.12: Reaction kinetics curve of Mg–Fe–Mn–Ni composition for different temperatures: (a) Charging kinetics and (b) Discharging kinetics

4.3 Ternary Mg–V–Ni Alloy Compositions

4.3.1 Sample Preparation

The ternary Mg–V–Ni system compositions are synthesized using Mg, V and Ni powders with a minimum of 99% purity. The milling experiments are conducted in a planetary ball mill. The detail technical parameters of ball mill are presented in chapter 3. The chemical composition of various Mg–V–Ni compositions are prepared with greater than or equal to 85 at% of Magnesium, 5 at% of Nickel and 2.5 at% to 10 at% of Vanadium. The weight calculations of individual elements of these compositions are given as under:

The atomic fraction of each element in the $Mg_{92.5\%}V_{2.5\%}Ni_{5\%}$ composition is computed as below:

$$Mg^{af} = \frac{Mg^{w}/Mg^{aw}}{Mg^{w}/Mg^{aw} + V^{w}/V^{aw} + Ni^{w}/Ni^{aw}} \qquad \text{---------------------} \; (4.1)$$

$$V^{af} = \frac{V^{w}/V^{aw}}{Mg^{w}/Mg^{aw} + V^{w}/V^{aw} + Ni^{w}/Ni^{aw}} \qquad \text{---------------------} \; (4.2)$$

$$Ni^{af} = \frac{Ni^{w}/Ni^{aw}}{Mg^{w}/Mg^{aw} + V^{w}/V^{aw} + Ni^{w}/Ni^{aw}} \qquad \text{---------------------} \; (4.3)$$

Where, Mg^{af}, V^{af} and Ni^{af} are the atomic fraction of Mg, V and Ni, respectively; Mg^{w}, V^{w} and Ni^{w} are the weight of Mg, V and Ni, respectively; and Mg^{aw}, V^{aw} and Ni^{aw} are the atomic weight of Mg, V and Ni, respectively.

Next, using Eqns. 4.1 to 4.3, weight of each element in $Mg_{92.5\%}V_{2.5\%}Ni_{5\%}$ composition can be computed as:

$$Mg^{w} = \frac{Mg^{aw} \times Mg^{af}}{Mg^{af} + V^{af} + Ni^{af}} = 22.49 \qquad \text{---------------------} \; (4.4)$$

$$V^{w} = \frac{V^{aw} \times V^{af}}{Mg^{af} + V^{af} + Ni^{af}} = 1.27$$ --------------------- (4.5)

$$Ni^{w} = \frac{Ni^{aw} \times Ni^{af}}{Mg^{af} + V^{af} + Ni^{af}} = 2.94$$ --------------------- (4.6)

Therefore, for 20 gm composition, the weight of Mg is computed as 16.85 gm, the weight of V is 0.95 gm and Ni is 2.20 gm for $Mg_{92.5\%}V_{2.5\%}Ni_{5\%}$ composition. Similarly, for $Mg_{90\%}V_{5\%}Ni_{5\%}$ and $Mg_{85\%}V_{10\%}Ni_{5\%}$ compositions, the weights of elements are also computed (see the Table 4.1).

Table 4.1: Elemental mass (for 20 gm) of different Mg–V–Ni compositions

Sr. No.	**Compositions**		**Elements**		
			Mg	**V**	**Ni**
1	MV1	*Atomic %*	92.50	2.50	5.00
		Weight %	84.23	4.72	11.50
		Mass, gm	16.85	0.95	2.20
2	MV2	*Atomic %*	90.00	5.00	5.00
		Weight %	79.96	9.31	10.73
		Mass, gm	15.99	1.86	2.15
3	MV3	*Atomic %*	85.0	10.0	5.0
		Weight %	72.02	18.33	9.65
		Mass, gm	14.40	3.67	1.93

4.3.2 Characterization Study

Micrographs showing the morphology of pure Vanadium and the optimized Mg–V–Ni composition (code MV2) are shown at various magnifications in Fig. 4.13. The mean particle size of pure Vanadium, without milling, is measured as 516 ± 246 µm. These micrographs also show the presence of adherent secondary particulates (in the form of sub-microscopic satellites), on the much larger Mg particles. The mean particle size of magnesium phase is measured as 12.3 ± 2 µm and mean particle size of the satellite catalyst particles is found to fall in two classes, namely 1.69 ± 0.3 µm and 0.36 ± 0.1 µm. All measurements are made using lineal analysis of SEM micrographs. Fig. 4.14 shows backscattered images of the optimized material at different magnifications. These micrographs clearly indicate the brighter particles to be elemental catalyst species (V and Ni). These micrographs also clearly indicate the homogeneous distribution of various catalysts.

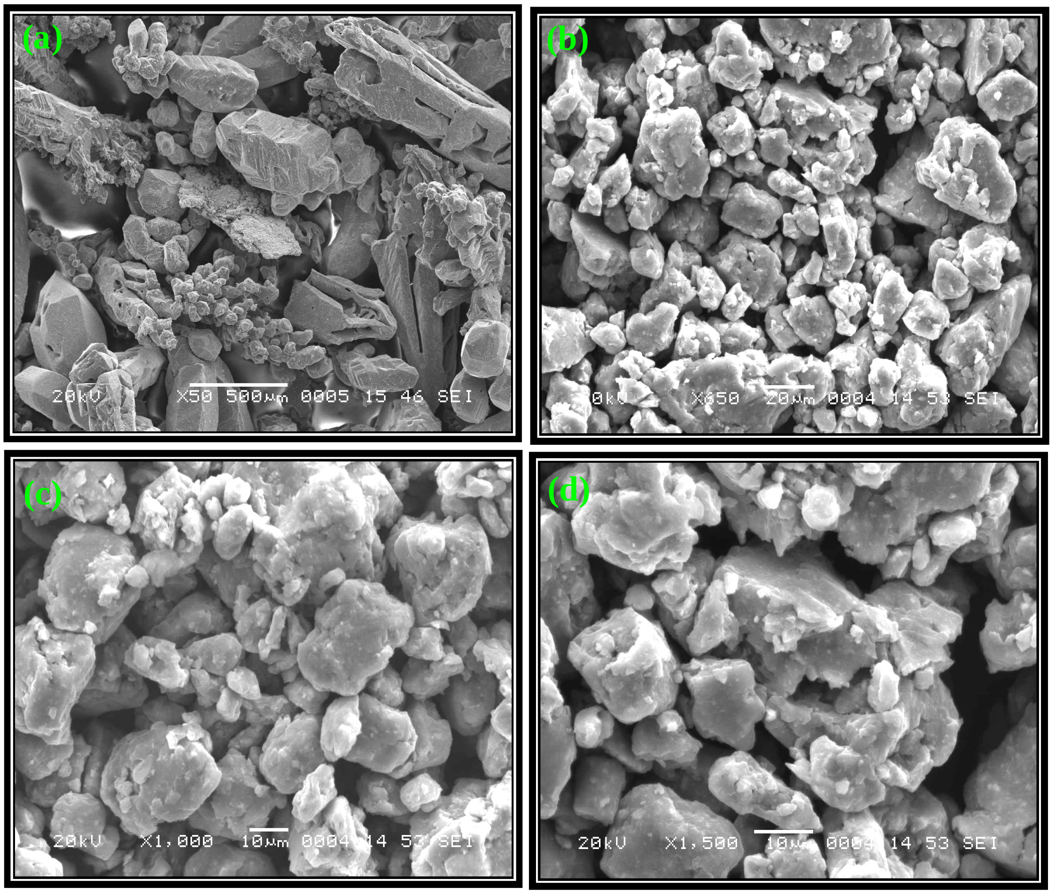

Fig. 4.13: SEM micrographs in secondary electron mode: (a) Pure V and optimized Mg–V–Ni composition (code MV2) at different magnifications: (b) 650 X, (c) 1000 X and (d) 1500 X

EDS analysis is conducted in SEI (secondary electron image) mode at an accelerating voltage of 20 kV and 100 X magnification on the three synthesized compositions. Results (presented in Table–4.2) indicate the measured elemental compositions match closely with the targeted compositions. Typical EDS spectra of the optimized (highest hydrogen storing) composition is shown in Fig. 4.15.

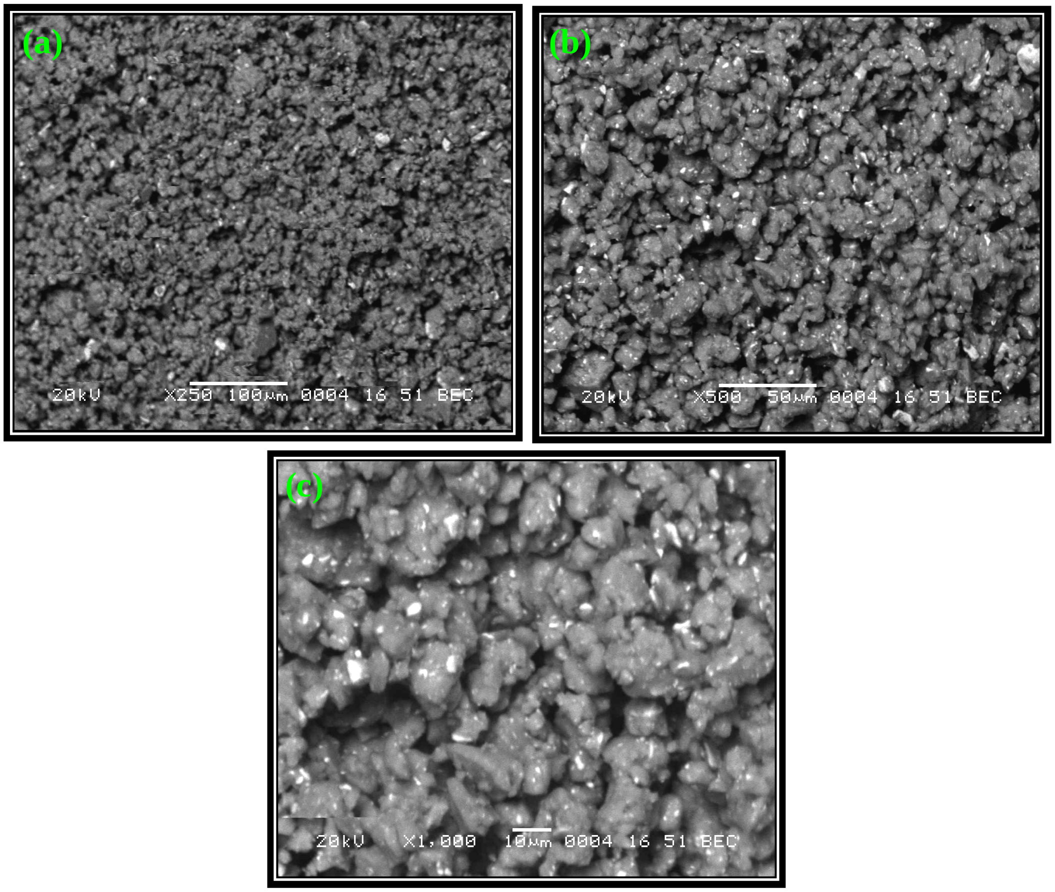

Fig. 4.14: SEM micrographs of the optimized Mg–V–Ni composition (code MV2), in back scattering mode at different magnifications: (a) 250 X, (b) 500 X and (c) 1000 X

Table–4.2: The elemental compositions of the synthesized Mg–Ni–V compositions

Sr. No.	**Alloy Code**	**Composition, Atomic %**					
		Mg		**Ni**		**V**	
		Target	**Obtained**	**Target**	**Obtained**	**Target**	**Obtained**
1	MV1	92.50	92.83	5.00	5.57	2.50	1.60
2	MV2	90.00	90.64	5.00	5.44	5.00	3.92
3	MV3	85.00	84.17	5.00	5.35	10.00	10.48

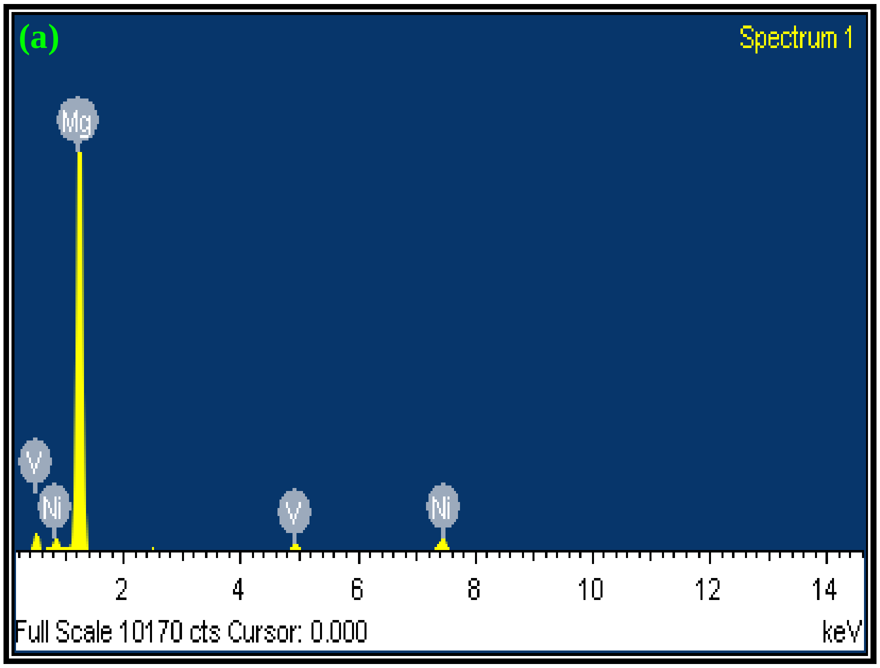
(a)
Spectrum 1
Mg
V
Ni
V
Ni
2
4
6
8
10
12
14
Full Scale 10170 cts Cursor: 0.000
keV

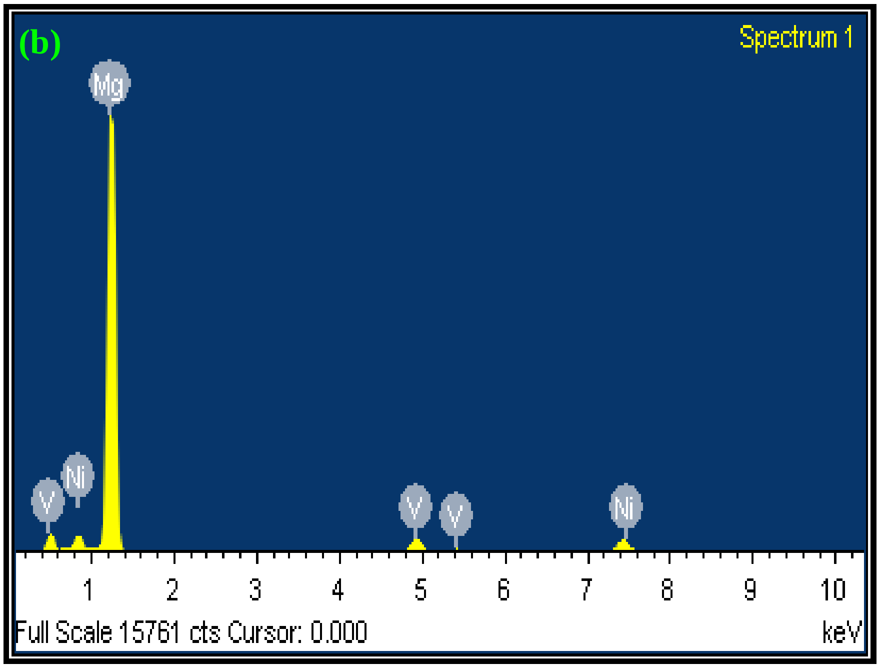
(b)
Spectrum 1
Mg
Ni
V
V
V
Ni
1
2
3
4
5
6
7
8
9
10
Full Scale 15761 cts Cursor: 0.000
keV

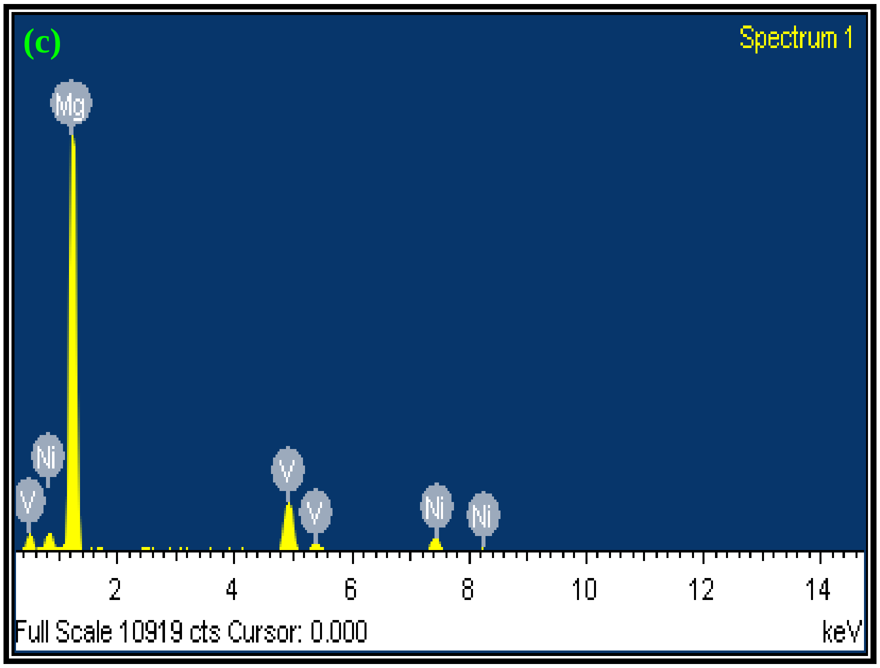

Fig. 4.15: EDS spectra of synthesized Mg–V–Ni compositions: (a) MV1, (b) MV2 and (c) MV3

The XRD spectra of the synthesized Mg–V–Ni compositions are presented in Fig. 4.16 (a). All the predominant peaks corresponding to Mg, Ni and V are seen. The diffraction peaks could be accurately indexed and correlated with Mg phase, Ni phase and V phase. The Bravais lattice system of these phases being hexagonal (cell parameters, a: 3.2022 Å & c: 5.1991 Å), cubic (cell parameter a: 3.5175 Å), and cubic (cell parameter a: 3.0400 Å), respectively. Further, the FWHM (full width – half maxima), the mean crystallite/grain sizes and relative intensity ratio of the highest intense peak of unhydrided Mg–V–Ni compositions are computed and shown in Table–4.3. This data indicates that as the Vanadium concentration increases, the FWHM spread increases, indicating crystallite size is decreased for same milling time (40 h milled sample).

Fig. 4.16 (b) presents the XRD spectra of the MV2 composition for different milling times. The phases present are seen to be the same as those indicated in Fig. 4.16 (a). The FWHM (full width – half maxima), the mean crystallite/grain size and relative intensity of the highest intensity peak of unhydrided Mg–V–Ni compositions, at various milling times, are presented in Table–4.4. The data shown in this table clearly indicates the presence of effect of milling on the crystallite size.

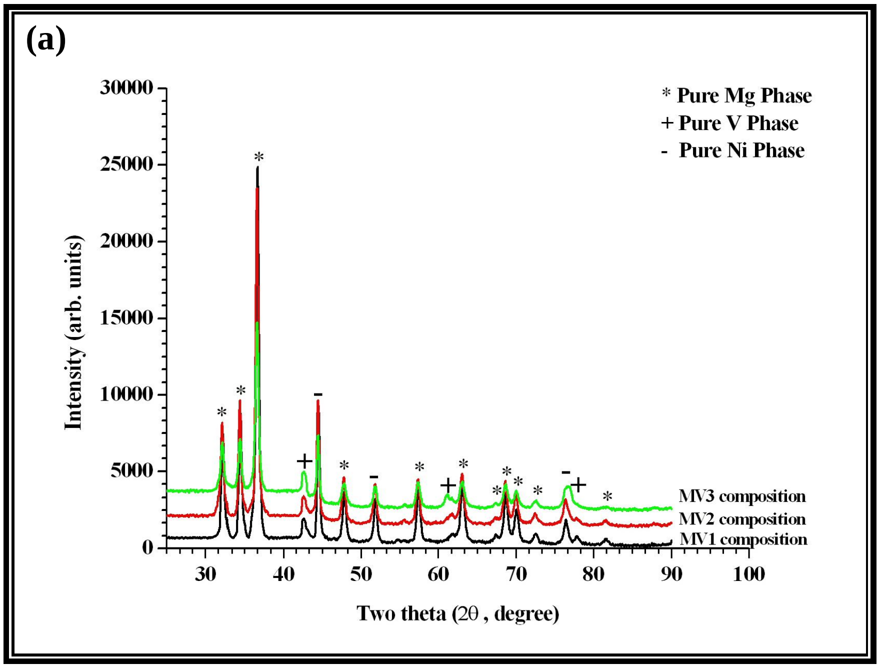

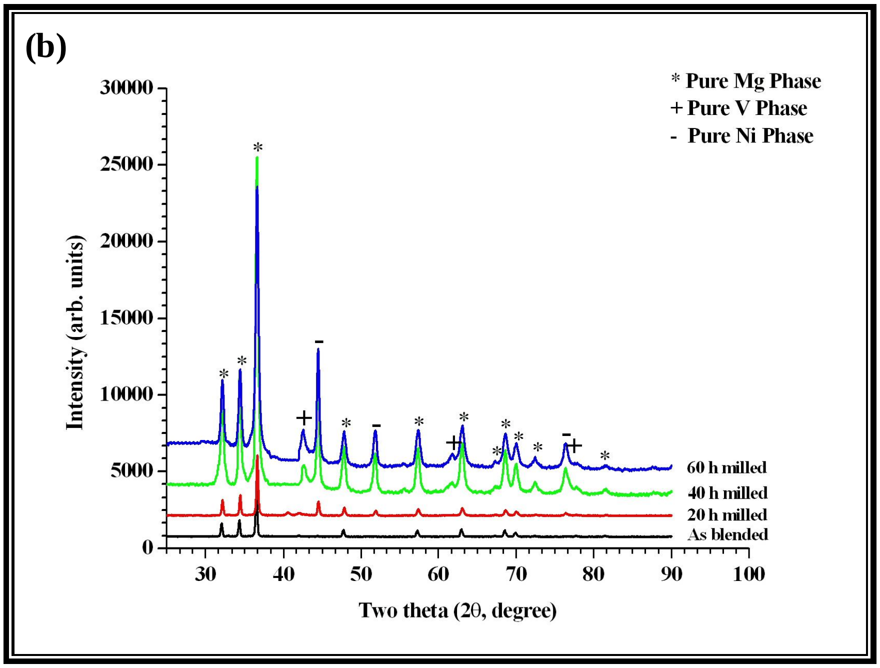

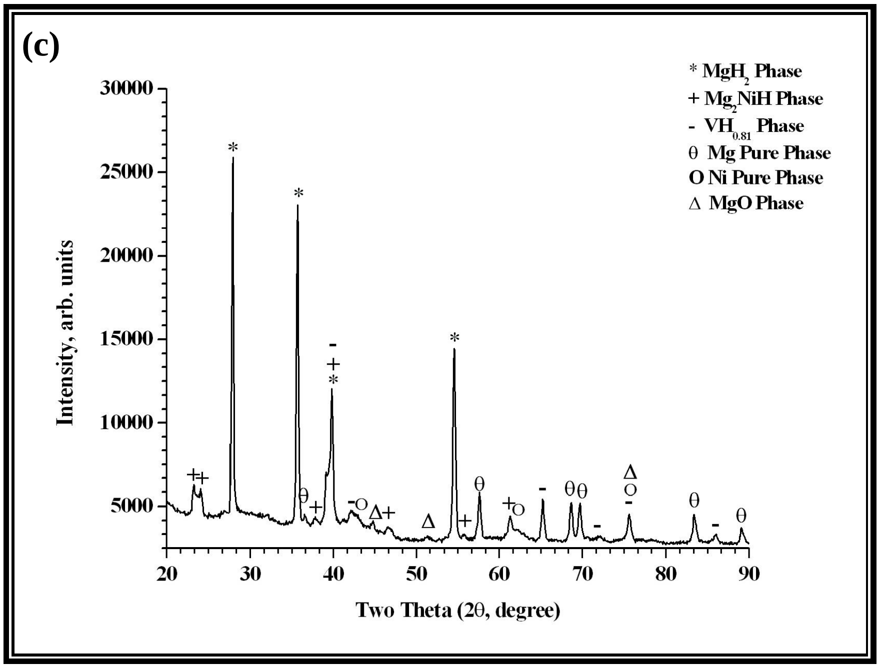

Fig. 4.16: XRD spectra: (a) Unhydrided Mg–V–Ni compositions (40 h milled), (b) Unhydrided MV2 composition for various milling times and (c) Hydrided composition of MV2

Table–4.3: Crystallite parameters of different Mg–V–Ni compositions for 40 h milling time

Sr. No.	Compositions code	FWHM, degree	Crystallite size, nm	Relative intensity ratio
1	MV1	0.378°	24.03	10
2	MV2	0.402°	23.18	9
3	MV3	0.486°	19.10	7

Table–4.4: Crystallite parameters of MV2 composition for different milling times

Sr. No.	Milling time, h	FWHM, degree	Crystallite size, nm	Relative intensity ratio
1	0 h (As blended)	0.167°	48.67	124
2	20 h	0.289°	31.72	26
3	40 h	0.402°	23.18	9
4	60 h	0.412°	19.76	7

The hydrided sample corresponding to the optimized composition was also subjected to XRD analysis. Fig. 4.16 (c) shows the diffraction spectra of this composition. It is seen that the hydrided composition contains various hydrided phases such as MgH_2, Mg_2NiH, $VH_{0.81}$, as well as unhydrided phases such as MgO, pure Mg and Ni. The Bravais lattice system of these phases is determined to be tetragonal (cell parameters, a: 4.5170 Å & c: 3.0205 Å), monoclinic (cell parameter a: 6.6020 Å, b: 6.4150 Å & c: 6.4530 Å), tetragonal (cell parameters, a: 3.0280 Å & c: 3.4000 Å), cubic (cell parameter a: 4.2030 Å), hexagonal (cell parameters, a: 3.2022 Å & c: 5.1991 Å), and cubic (cell parameters, a: 3.5175 Å), respectively. Further, the mean crystallite/grain sizes of these phases are 38.95 nm for MgH_2, 21.19 nm for Mg_2NiH, 8.55 nm for $VH_{0.81}$, 9.68 nm for MgO, 17.92 nm for Mg, and 10.16 nm for the Ni phase. Note that the mean crystallite/grain size of the hydrided MgH_2 phase is larger by nearly 15 nm with respect to the unhydrided Mg phase.

4.3.3 Hydriding and Dehydriding Analysis

Fig. 4.17 presents the effect of milling time on mass percent of hydrogen absorbed for composition MV2 at 265 °C. It can be seen that the compositions milled for 40 h shows significantly more hydrogen absorbed. This graph indicates that the mass percent of hydrogen absorption is less than 1 mass% for unmilled (blended only) V, Ni and Mg composition, with very poor kinetics (~ 1 hour absorption time). For 20 h milling, the hydrogen uptake increases and shows fast kinetics. It is also clearly seen that the composition MV2 up-takes greater than 95 % of hydrogen within first 3 to 5 minutes at 265 °C for 40 h milling time. Further, for 60 h milling time, hydrogen up-take capacity decreases.

In Fig. 4.18, the effect of different compositions on mass percent of hydrogen absorbed for 40 h milled samples are presented at 265 °C. This plot clearly shows that the highest absorption of Hydrogen occurs for composition coded MV2. It can be also seen from this plot that the mass% of absorbed Hydrogen of composition MV3 is lower with respect to MV1 and MV2 compositions. In light of the above, composition MV2 shows the highest Hydrogen uptake capacity in minimal time. Hence, within the framework of the experiments conducted, composition MV2 is deemed as the optimized composition.

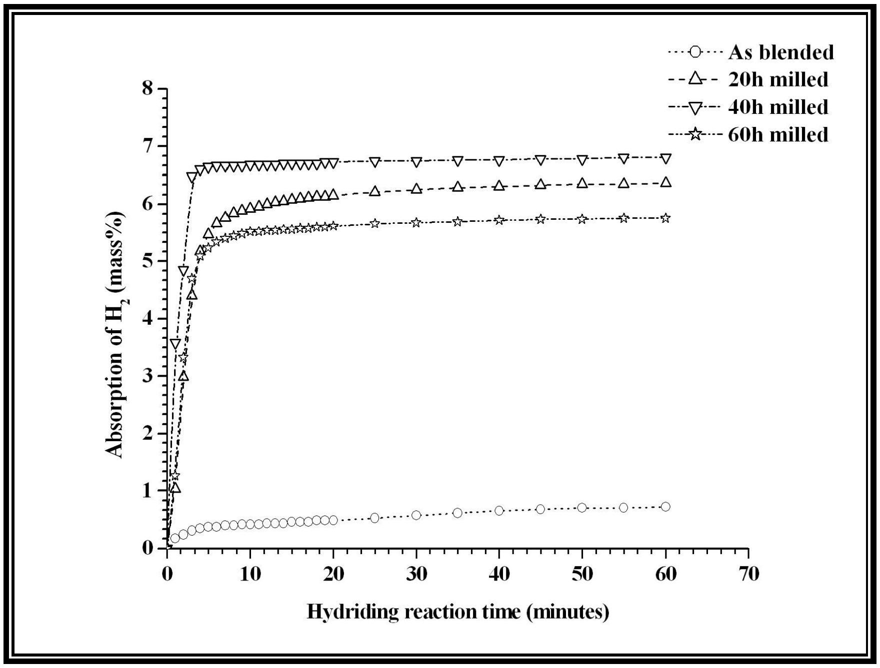

Fig. 4.17: Charging kinetics curve of MV2 composition for as blended and different milling times

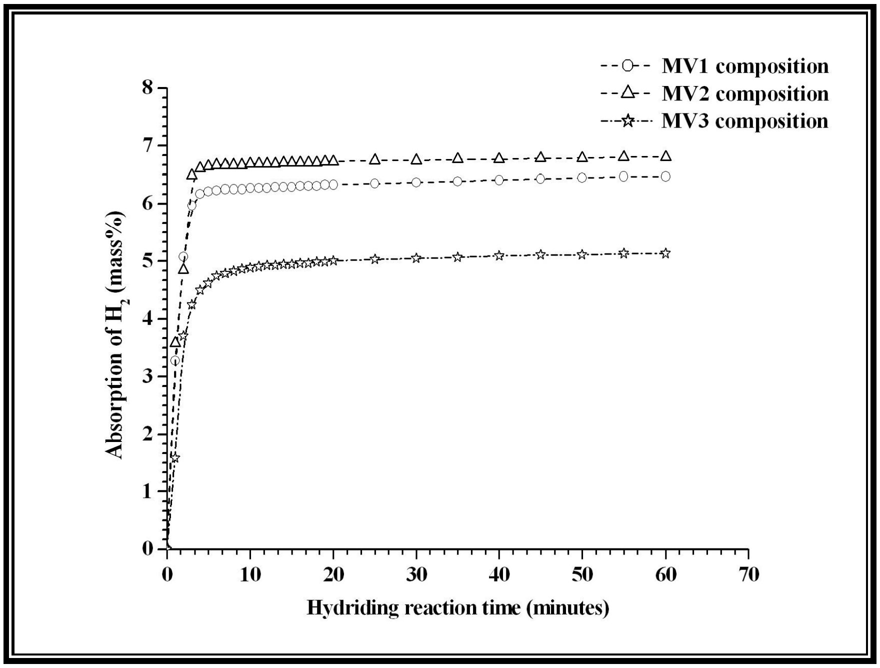

Fig. 4.18: Charging kinetics curve for different compositions

Fig. 4.19 shows the effect of hydriding temperature on mass% of absorbed Hydrogen for different compositions for a 40 h milled sample. Fig. 4.19 (a) presents plot of absorbed Hydrogen versus hydriding time for composition MV1 for different temperatures at 40 h milling. This graph indicates that the mass % of Hydrogen absorbed increases up to 265 °C and, thereafter, temperature ceases to have any effect on mass% absorption. Similarly, Figs. 4.19 (b) and (c) show the Hydriding kinetics for compositions coded MV2 and MV3, respectively. Specifically, Fig. 4.19 (b) clearly indicates that 90% – 95% hydrogen is absorbed within 3 to 5 minutes at 265 °C. Fig. 4.19 (c) shows that the composition MV3 has slow kinetics in comparison to compositions MV1 and MV2.

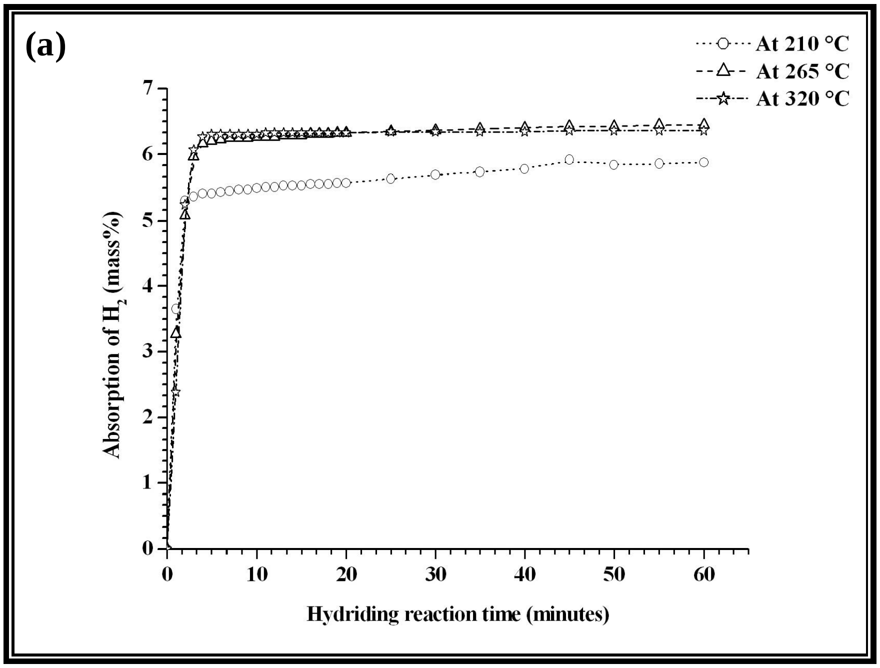

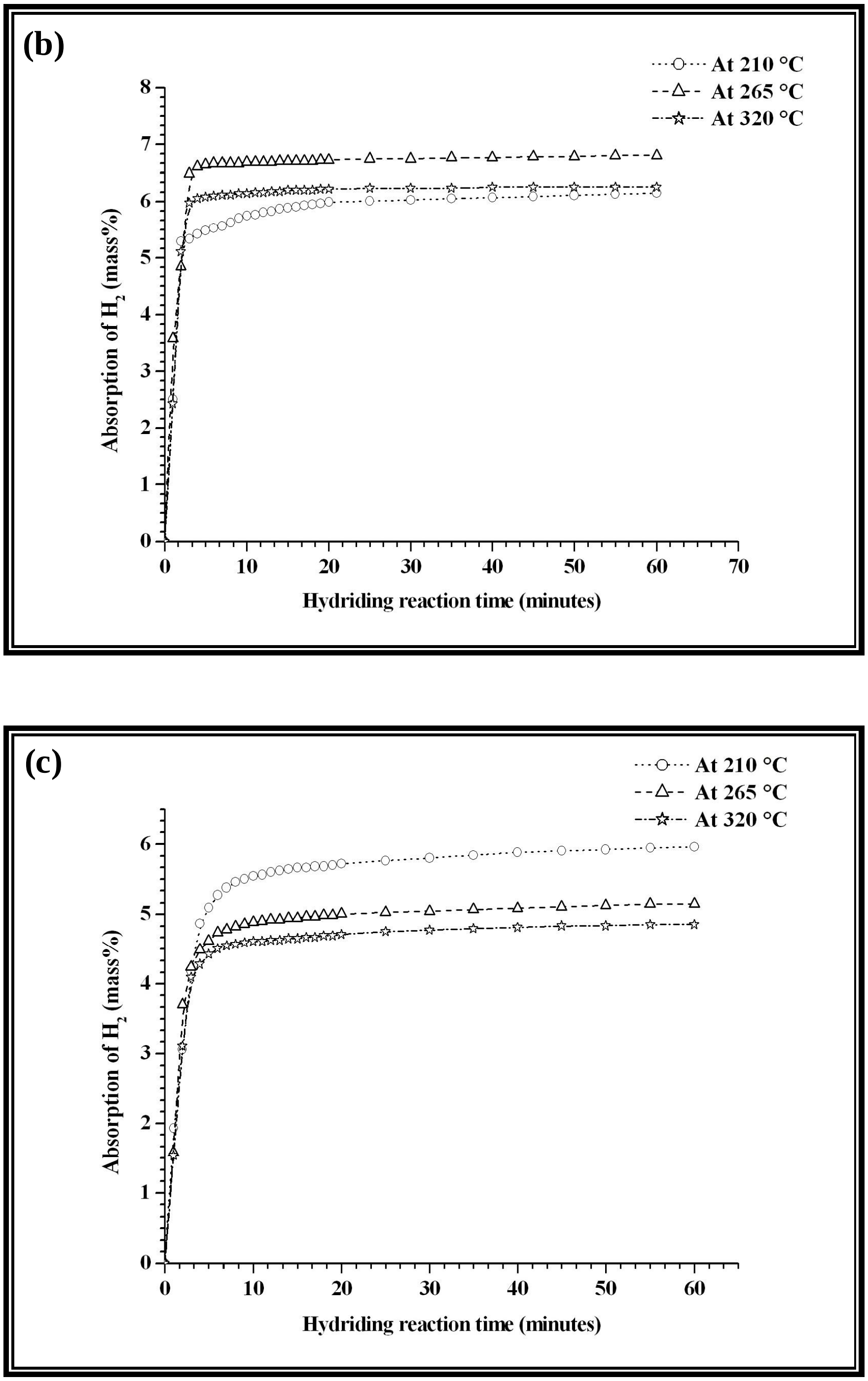

Fig. 4.19: Charging kinetics curve for different Mg–V–Ni compositions at different hydriding temperatures: (a) MV1, (b) MV2 and (c) MV3

Fig. 4.20 shows the effect of dehydriding temperature and alloy composition on mass percent of hydrogen desorbed for the 40 h milled samples. This graph indicates that the mass percent of hydrogen desorption increases with increasing temperature for all three compositions, with highest desorption occurring at 375 °C for all three compositions. The optimized MV2 coded composition shows 5.02 mass% of H_2 released at a discharging temperature of 375 °C. Note also that for compositions MV1 and MV2, the dehydriding time is nearly same (~ 6 to 8 minutes) at the three temperatures investigated. Further, for composition MV3, the dehydring time is slightly higher with respect to MV1 and MV2 (~ 8 to 10 minutes). The above results are in line with the work of Zaluska et al. (1999) [17] and Lototsky et al. (2009) [18], who have clearly demonstrated presence of “absorption rate” and “capacity” enhancement effects due to addition of Vanadium [19].

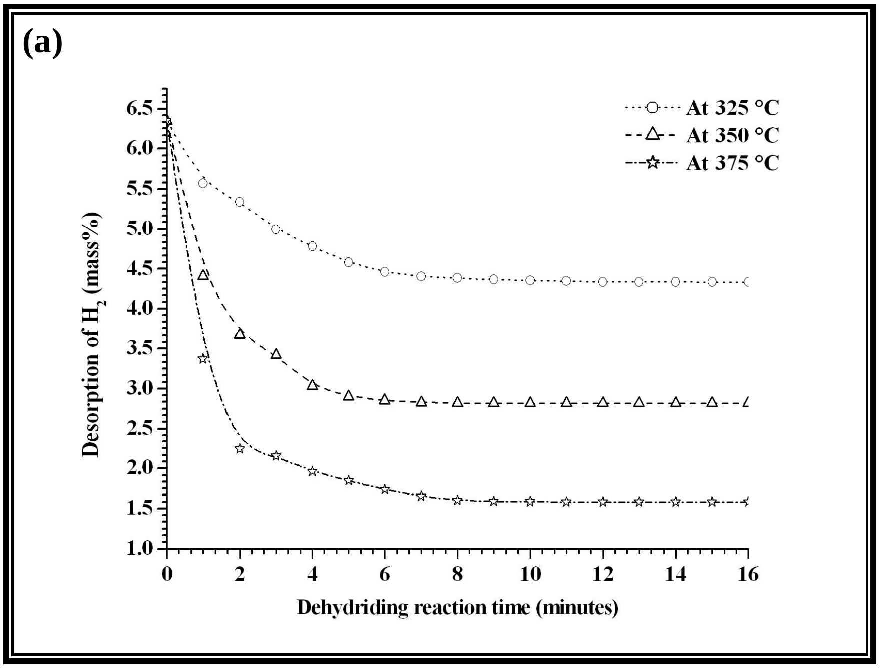

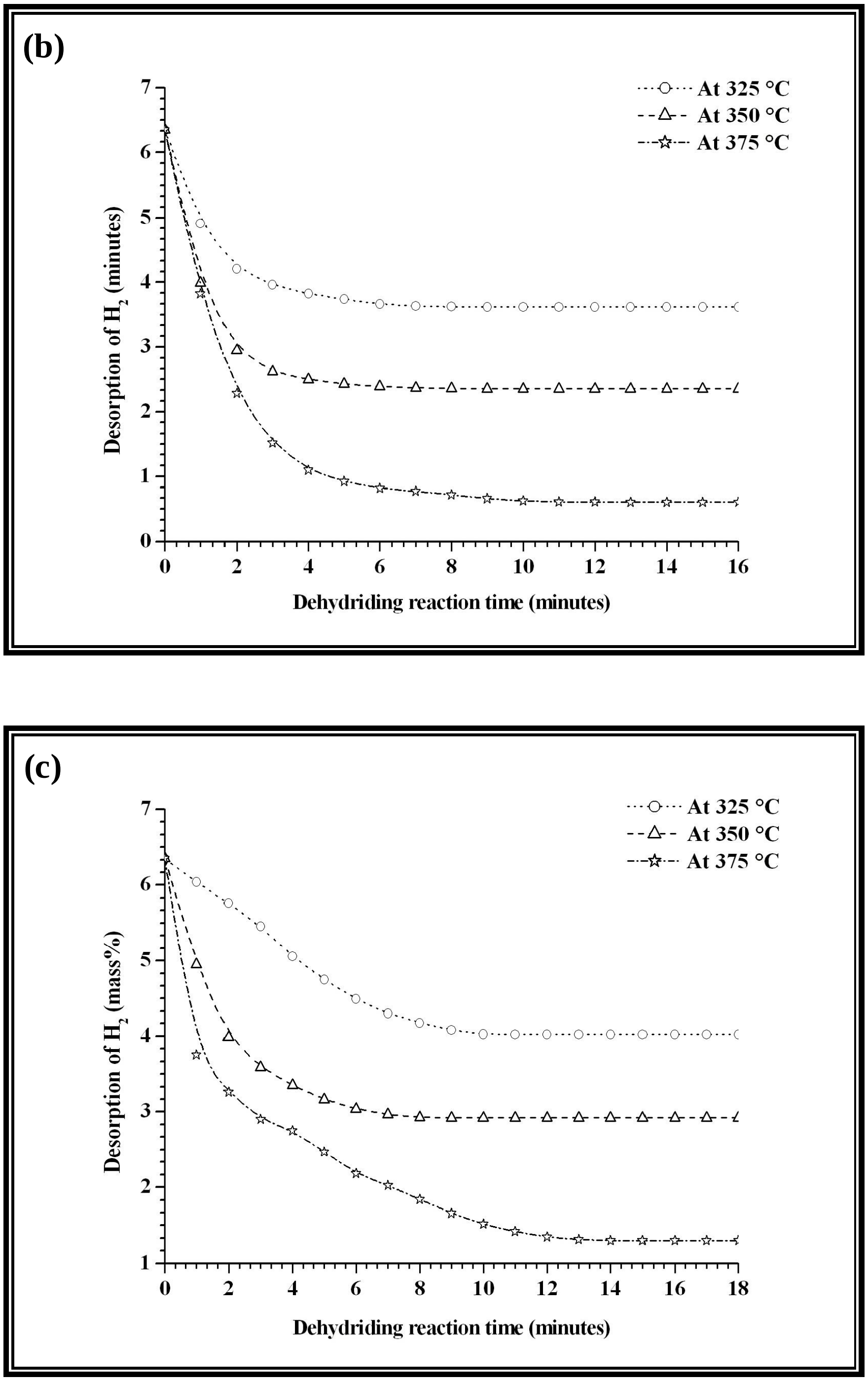

Fig. 4.20: Discharging kinetics curve for different Mg–V–Ni compositions at different dehydriding temperatures: (a) MV1, (b) MV2 and (c) MV3

4.3.4 Deviations in Hydriding and Dehydriding Kinetics due to Departure from Ideal Gas Behavior of Hydrogen

In Fig. 4.21 (a), the mass% of hydrogen absorbed versus time data, computed using the ideal gas equation as well the three real gas equations of state is presented for the optimized MV2 coded composition. For this alloy, the maximum absorption capacity is computed as 6.73 mass% using the ideal gas equation, and 6.51, 6.39 and 6.42 mass% using Van–der–Waal, Redlich–Kwong and Redlich-Kwong-Soave equations, respectively [20]. The percent deviations from ideal gas computations are plotted as a function of time in Fig. 4.21 (b). The percentage deviations in the hydriding kinetics data are obtained about 3.25%, 4.98% and 4.48% for Van–der–Waal, Redlich–Kwong and Redlich–Kwong–Soave equations, respectively. Clearly, significant deviation occurs in predicting the reacted mass of hydrogen using the ideal gas equation. If such errors are not properly accounted for, significant errors can propagate in large scale reactor design not only affecting the reaction kinetics, but also the reaction yield, in terms of total absorption obtained at end of the reaction as well as the total reaction time required for completing the reaction.

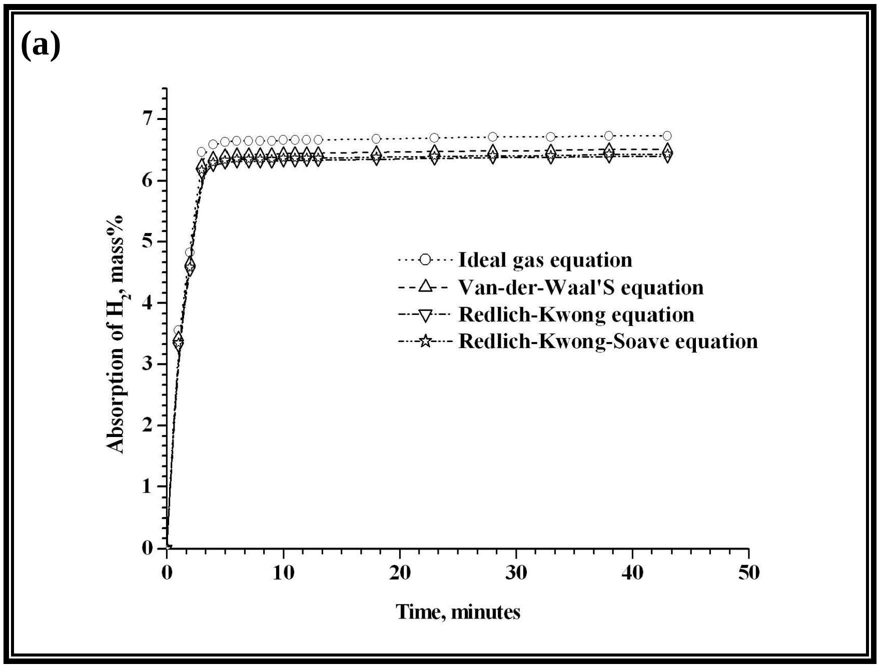

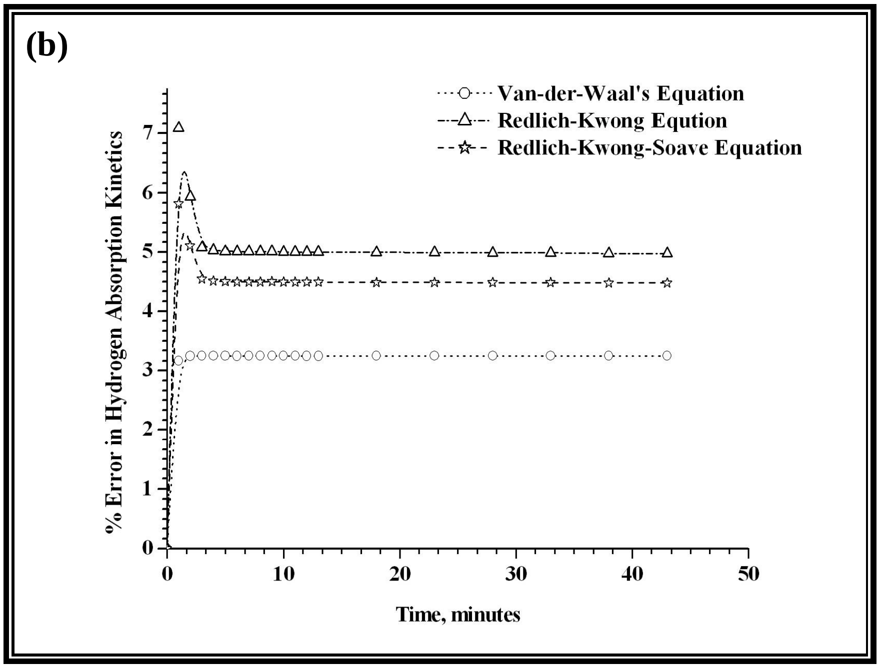

Fig. 4.21: Hydriding characterization of MV2 coded alloy composition using ideal and real gas equations: (a) H_2 absorption versus time and (b) Deviation in absorption from ideal gas equation

In Fig.4.22 (a), the mass % of hydrogen desorbed versus time data is computed using the ideal gas eqation as well as the three real gas equations of state for the optimized MV2 coded composition. For this composition, the maximum desorption capacity is computed as 5.68 mass% using the ideal gas equation and 5.58, 5.61 and 5.60 mass% using Van–der–Waal, Redlich–Kwong and Redlich-Kwong-Soave equations, respectively. The percent deviations are plotted as a function of time in Fig. 4.22 (b). The observed percentage deviation of hydrogen desorption using ideal gas equation with respect to the three real gas equations are obtained as 1.41%, 1.27% and 1.36% for Van–der–Waal, Redlich–Kwong and Redlich–Kwong–Soave equations, respectively. However, while this deviation due to the ideality assumption is smaller than that obtained for the absorption kinetics, it is still significant and not accurate enough for chemical reaction modelling as well as for optimal design of large scale reactors for conducting commercial scale hydriding.

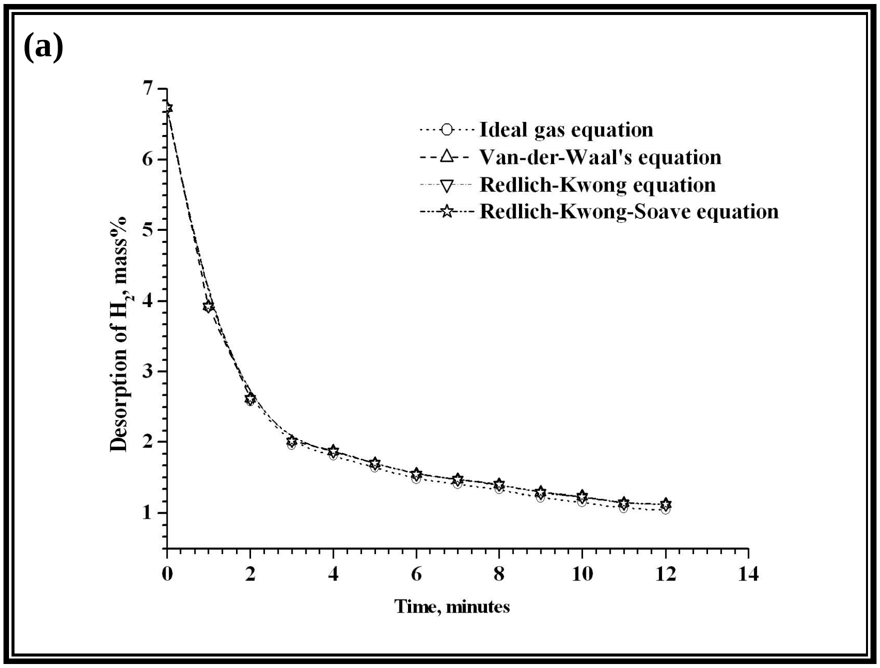

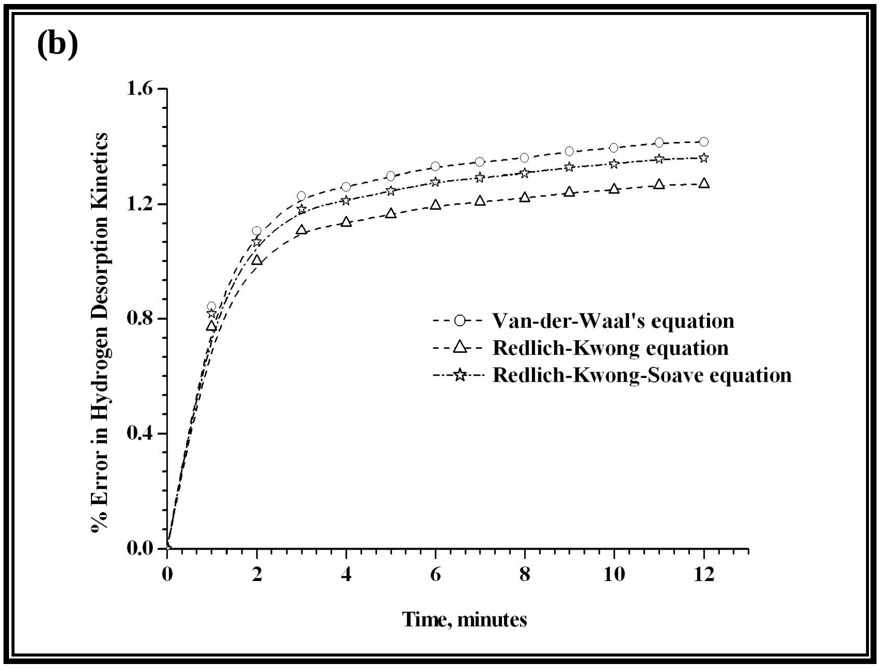

Fig. 4.22: Dehydriding characterization of MV2 coded alloy composition using ideal and real gas equations: (a) H_2 desorption versus time and (b) Deviation in desorption from ideal gas equation

4.3.5 Reaction Kinetics Modelling Analysis

The experimental data of the optimized MV2 coded alloy composition at 265 ºC is first modelled using a first-order lumped exponential response model of the form as presented in chapter 2 (section 2.5.1, Eqns. 2.16 and 2.20). The experimental constants in these two equations are determined using linear regression and predictions of the estimated models are compared with experimental data in Fig. 4.23 (a) and (b). For the charging model, the estimated values of the constants are determined as: $\hat{\alpha}_c = 6.54$ & $\hat{\beta}_c = 0.20$, with coefficient of correlation obtained as:

$$\left(R_0^2\right)_{Charging} = 0.81 \qquad \text{--------------------- (4.7)}$$

Similarly, for the discharging model, the estimated constants are determined as: $\hat{\alpha}_d = 6.06$ & $\hat{\beta}_d = 0.29$, with coefficient of correlation obtained as:

$$\left(R_0^2\right)_{Discharging} = 0.80 \qquad \text{--------------------- (4.8)}$$

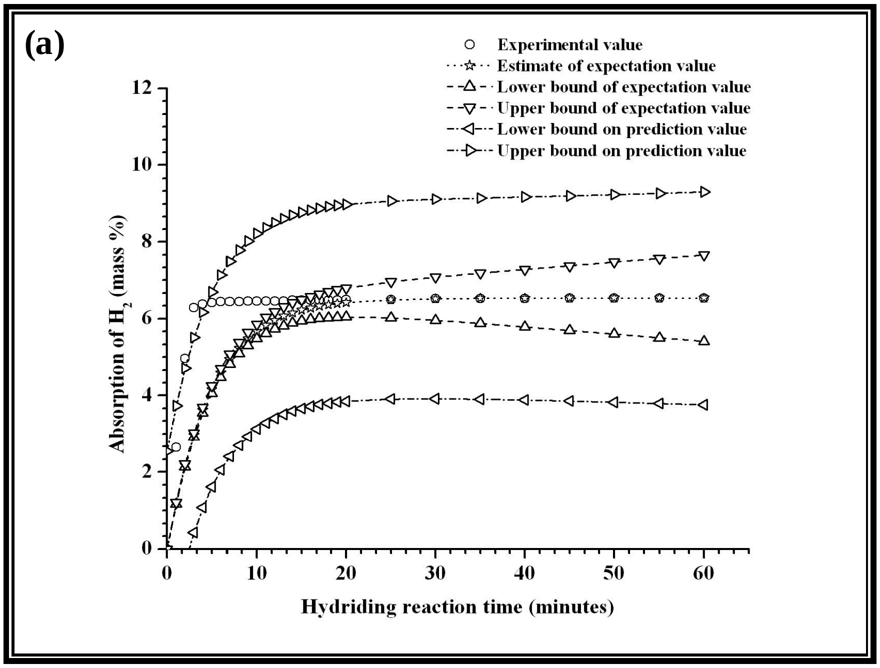

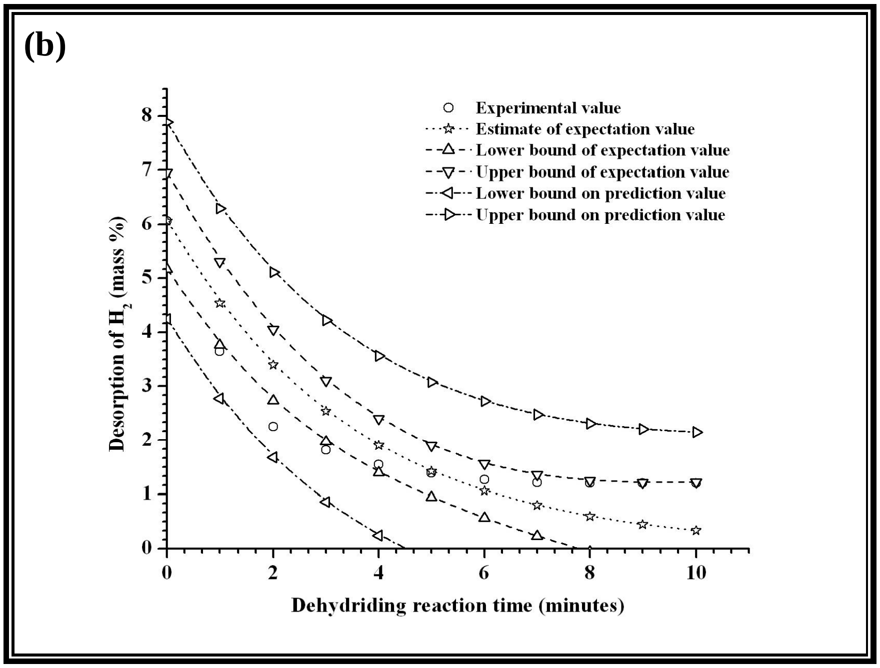

Fig. 4.23: Model fit for experimental data using lumped first order kinetics model for the optimized MV2 coded composition: (a) Charging kinetics and (b) Discharging kinetics

The value of $\left(R_0^2\right)_{Charging}$ indicates that the linear model used is not able to explain 19 % of charging data variability. Similarly, the value of $\left(R_0^2\right)_{Discharging}$ indicates that about 20 % of discharging data variability remains unexplained. While these values indicate reasonable fit, clearly the correlation can be improved by a more elaborate model. In the next section, we have attempted to explain the reaction kinetics by the more sophisticated shrinking core model.

Shrinking core model is used to describe situations in which solid particles are being consumed either by dissolution or reaction and, as a result, the amount of the material being consumed is ‘shrinking’. This model applies for fitting the hydrogen absorption data at 265 ºC. Equations described in chapter 2 (section 2.5.2, Eqns. 2.22, 2.23 and 2.24) are compared with the experimental results in Fig. 4.24 (a). This graph indicates that the full form, shrinking core model, given by Eq. (2.22) gives a better estimation of the experimental data. However, clearly both the individual purely chemical and purely diffusion control models, respectively, are not adequate to characterize the experimental data and the full model needs to be used. For this purpose, a numerical statistical factorial experiment in the dimensionless space of t^*, ϕ_1 and ϕ_2 is designed.

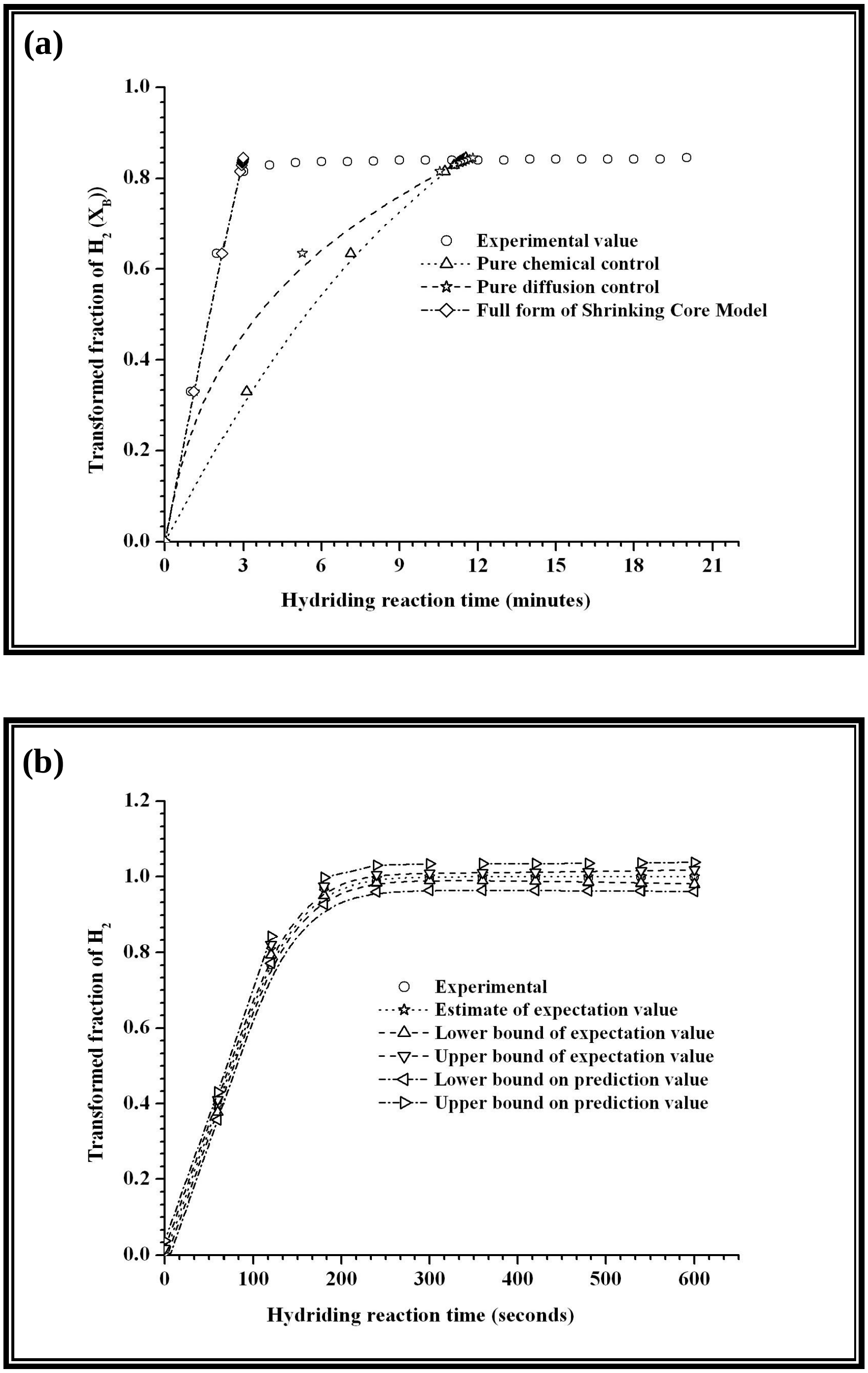

Fig. 4.24: Model fit for experimental data using different model for the optimized MV2 coded composition: (a) Shrinking core model and (b) Johnson–Mehl–Avrami model

Using a minimum variance non-linear optimization scheme, the best fit corresponding to mass transfer coefficient in gas phase, k_α as 1×10^{-6} m/s and reaction rate constant, k_r as 9×10^{-6} m/s has been obtained. For this optimization, value of the diffusion coefficient through species βH_2 of α, D_P is taken as 9.77×10^{-9} m^2/s (reported by Nishimura et al 1999) [21] and mean radius of spherical particles, r_p as 6.17×10^{-6} m (measured using SEM).

In Fig. 4.24(b), the Johnson–Mehl–Avrami (JMA) model is fitted, which represents a generalized case of random nucleation and growth in the optimized MV2 coded composition. In the JMA model, nucleation occurs randomly. The JMA equation has been given in chapter 2 (section 2.5.3, Eqns. 2.25 and 2.26). For the JMA full linear regression model a co-efficient of correlation, R^2 is obtained as 0.9981, and Avrami exponent, n is obtained as 1.72 [22]. Note also that in about 120 s, the transformed fraction of the hydride reaches about 77 %.

4.3.6 Prediction of Formation Enthalpy and Entropy

The formation of enthalpy and entropy during dehydriding reaction are estimated by Van't Hoff relation, which is presented in chapter 3. Using Van't Hoff relation, the enthalpy of formation (ΔH_0) of the optimized MV2 (40 h milled) composition is determined as 76.8 kJ/mole of H_2, and the entropy (ΔS_0) is computed as 135 J/mole of H_2 K. Using the experimental results and statistical error expressions, the uncertainty associated with enthalpy is obtained as 8.1 % and uncertainty associated with entropy is as 5.1 %. Therefore, the enthalpy of formation can be stated as 76.8 ± 6.2 kJ/mole of H_2, and the entropy can be stated as 135 ± 6.9 J/mole of H_2 K. The logarithmic plot of equilibrium pressure versus temperature (Van't Hoff relationship) is compared with experimental / values obtained (with the coefficient of correlation, R^2_0 as 0.9549, see Fig. 4.25).

The experimentally extracted value for $\overline{\Delta H}$ by the DSC method (see Fig. 4.26) is obtained as 71.6 ± 5.8 kJ per mole of hydrogen for optimized MV2 coded composition. Further, if one assumes the dehydriding reaction in the DSC to be close to equilibrium (which is thermodynamically unlikely), "pseudo specific entropy",

$\overline{\Delta S}_{pseudo}$ can be computed as 127.1 ± 6.5 kJ per (mole of H_2) K. It is to be noted that the pseudo entropy is computed under "far from equilibrium" conditions and, hence, is not expected to be close to the entropy obtained using Van't Hoff analysis.

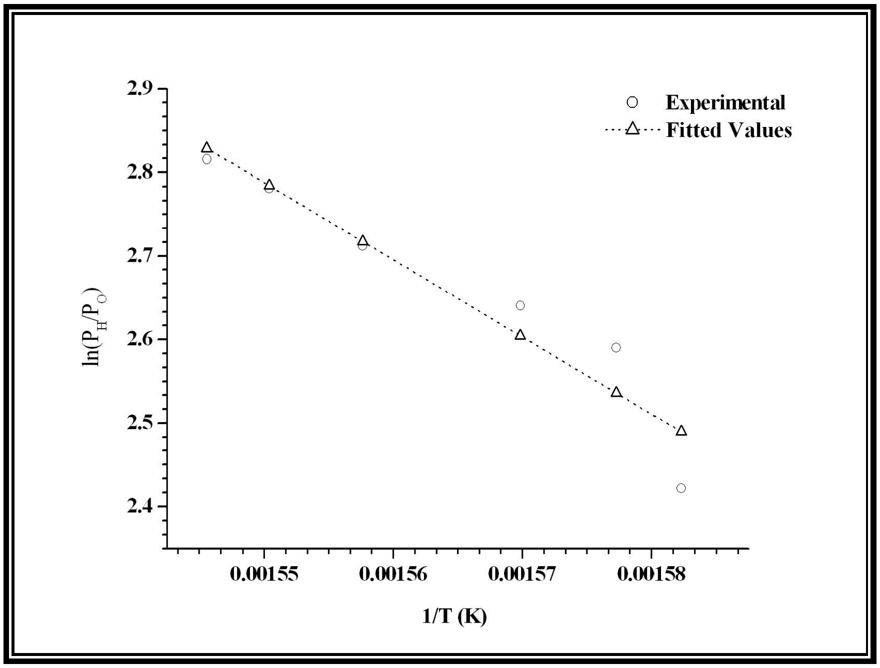

Fig. 4.25: Experimental and derived pressure ratio versus inverse temperature (using Van't Hoff equation) for optimized MV2 composition

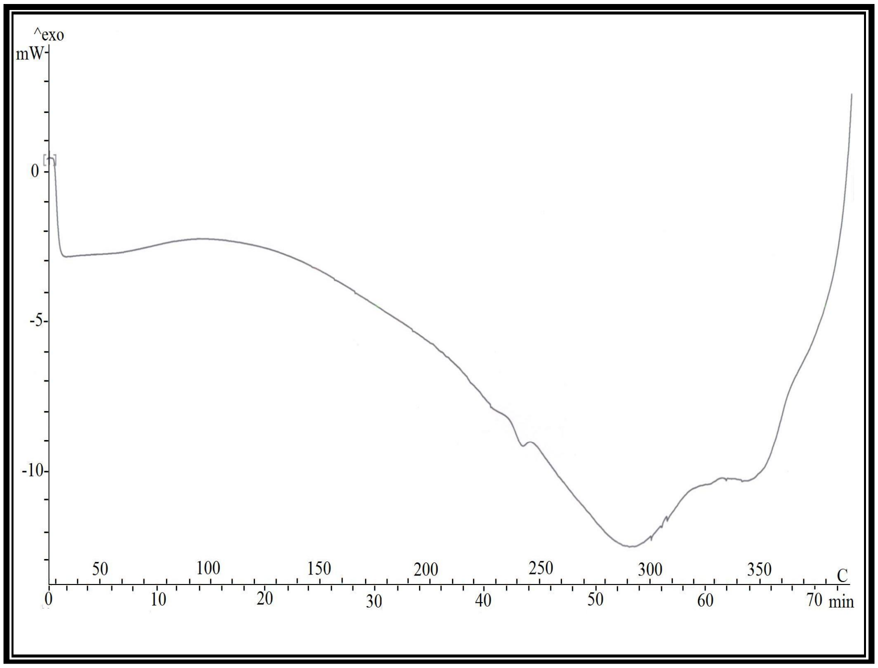

Fig. 4.26: Electrical power absorbed during DSC test versus time/temperature plot for hydrided MV2 coded composition

4.4 Ternary Mg–Pd–Ni Alloy Compositions

4.4.1 Sample Preparation

The ternary Mg–Pd–Ni system is synthesized using Mg, Pd and Ni powders with a minimum of 99% purity. The milling experiments are conducted in a planetary ball mill. The detailed technical parameters of ball mill are presented in chapter 3. The chemical composition of various Mg–Pd–Ni compositions are prepared with greater than or equal to 94 at% of Magnesium, 5 at% of Nickel and 0.1 at% to 1.0 at% of Palladium. The weight calculations of individual elements of these compositions are given as under:

The atomic fraction of each element in the $Mg_{94.9\%}Pd_{0.1\%}Ni_{5\%}$ composition is computed as below:

$$Mg^{af} = \frac{Mg^{w} / Mg^{aw}}{Mg^{w} / Mg^{aw} + Pd^{w} / Pd^{aw} + Ni^{w} / Ni^{aw}} \qquad \text{--------------------- (4.9)}$$

$$Pd^{af} = \frac{Pd^{w} / Pd^{aw}}{Mg^{w} / Mg^{aw} + Pd^{w} / Pd^{aw} + Ni^{w} / Ni^{aw}} \qquad \text{--------------------- (4.10)}$$

$$Ni^{af} = \frac{Ni^{w} / Ni^{aw}}{Mg^{w} / Mg^{aw} + Pd^{w} / Pd^{aw} + Ni^{w} / Ni^{aw}} \qquad \text{--------------------- (4.11)}$$

Where, Mg^{af}, Pd^{af} and Ni^{af} are the atomic fraction of Mg, Pd and Ni, respectively; Mg^{w}, Pd^{w} and Ni^{w} are the weight of Mg, Pd and Ni, respectively; and Mg^{aw}, Pd^{aw} and Ni^{aw} are the atomic weight of Mg, Pd and Ni, respectively.

Next, using Eqns. 4.7 to 4.9, weight of each element in the $Mg_{94.9\%}Pd_{0.1\%}Ni_{5\%}$ composition can be computed as:

$$Mg^{w} = \frac{Mg^{aw} \times Mg^{af}}{Mg^{af} + Pd^{af} + Ni^{af}} = 23.07 \qquad \text{--------------------- (4.12)}$$

$$Pd^{w} = \frac{Pd^{aw} \times Pd^{af}}{Mg^{af} + Pd^{af} + Ni^{af}} = 0.1064 \qquad \text{--------------------- (4.13)}$$

$$Ni^{w} = \frac{Ni^{aw} \times Ni^{af}}{Mg^{af} + Pd^{af} + Ni^{af}} = 2.94 \qquad \text{--------------------- (4.14)}$$

Therefore, for 20 gm composition, the weight of Mg is computed as 17.67 gm, the weight of Pd is 0.08 gm and Ni is 2.25 gm for $Mg_{94.9\%}Pd_{0.1\%}Ni_{5\%}$ composition. Similarly, for $Mg_{94.5\%}Pd_{0.5\%}Ni_{5\%}$ and $Mg_{94\%}Pd_{1\%}Ni_{5\%}$ compositions, the weights of elements are also computed (see the Table 4.5).

Table 4.5: Elemental mass (for 20 gm) of different Mg–Pd–Ni compositions

Sr. No.	**Compositions**		**Elements**		
			Mg	**Pd**	**Ni**
1	MP1	*Atomic %*	94.90	0.10	5.00
		Weight %	88.35	0.41	11.24
		Mass, gm	17.67	0.08	2.25
2	MP2	*Atomic %*	94.50	0.50	5.00
		Weight %	86.89	2.01	11.10
		Mass, gm	17.38	0.40	2.22
3	MP3	*Atomic %*	94.0	1.0	5.0
		Weight %	85.11	3.96	10.93
		Mass, gm	17.02	0.79	2.19

4.4.2 Characterization Study

Micrographs showing the morphology of the pure Palladium and the different Mg–Pd–Ni compositions are shown in Fig. 4.27. The mean particle size of the pure Pd is measured as 198 ± 74.5 μm. Micrographs of different Mg–Pd–Ni compositions in backscattering electron image mode show the presence of adherent secondary particulates (in the form of sub-microscopic satellites), on the much larger Mg particles and clearly indicate the brighter particles to be elemental catalyst species (Pd and Ni). The mean particle size of Magnesium phase is measured as 14.3 ± 2.9 μm, 12.8 ± 2.4 μm, and 11.3 ± 2.2 μm for MP1, MP2 and MP3 compositions, respectively.

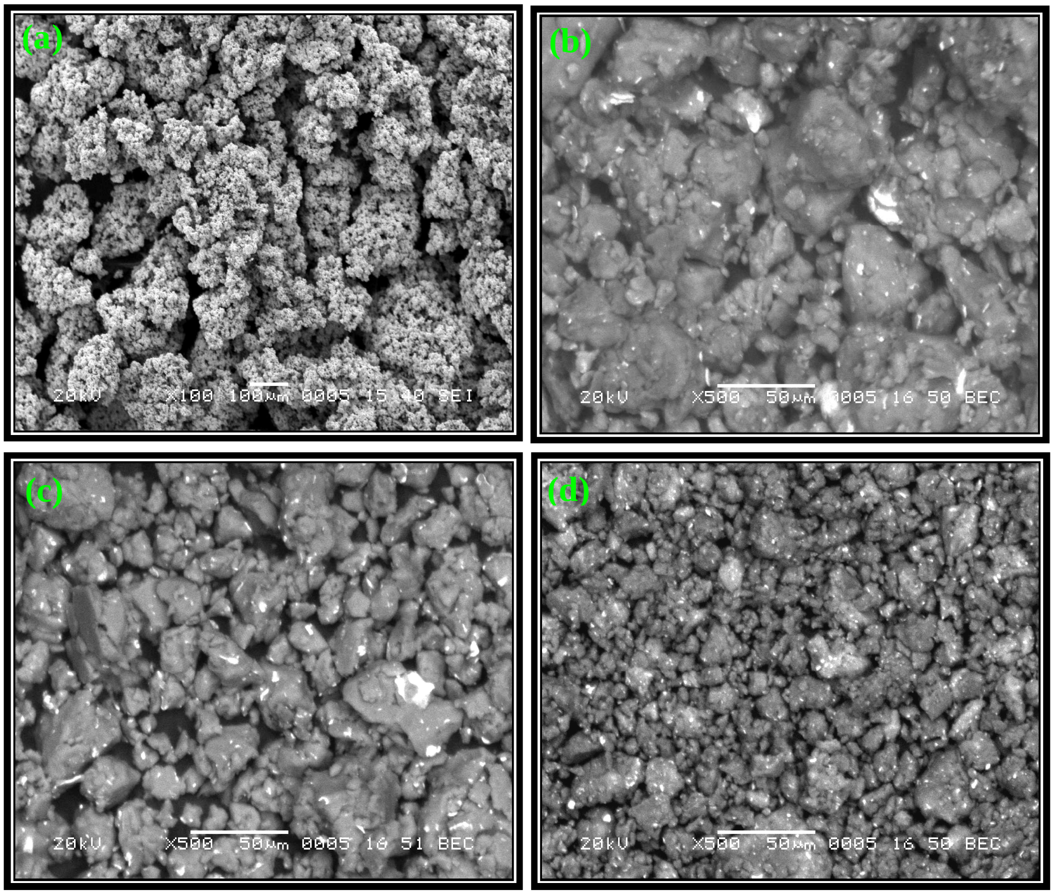

Fig. 4.27: SEM micrographs: (a) Pure Palladium and synthesized Mg–Pd–Ni compositions (b) MP1, (c) MP2 and (d) MP3

Table–4.6: The elemental compositions of the synthesized Mg–Pd–Ni compositions

Sr. No.	**Elements**	**Atomic %**	**Composition code**		
			MP1	**MP2**	**MP3**
1	Mg	Targeted	94.90	94.50	94.00
		Obtained	95.97	94.40	94.22
2	Pd	Targeted	0.10	0.50	1.00
		Obtained	0.18	0.62	1.27
3	Ni	Targeted	5.00	5.00	5.00
		Obtained	3.86	4.97	4.51

EDS analysis is conducted in SEI (secondary electron image mode) at an accelerating voltage of 20 kV and 100 X magnification on the three synthesized compositions. Results (presented in Table–4.6) indicate the measured elemental compositions match closely with the targeted compositions. Typical EDS spectra of these compositions are shown in Fig. 4.28

.

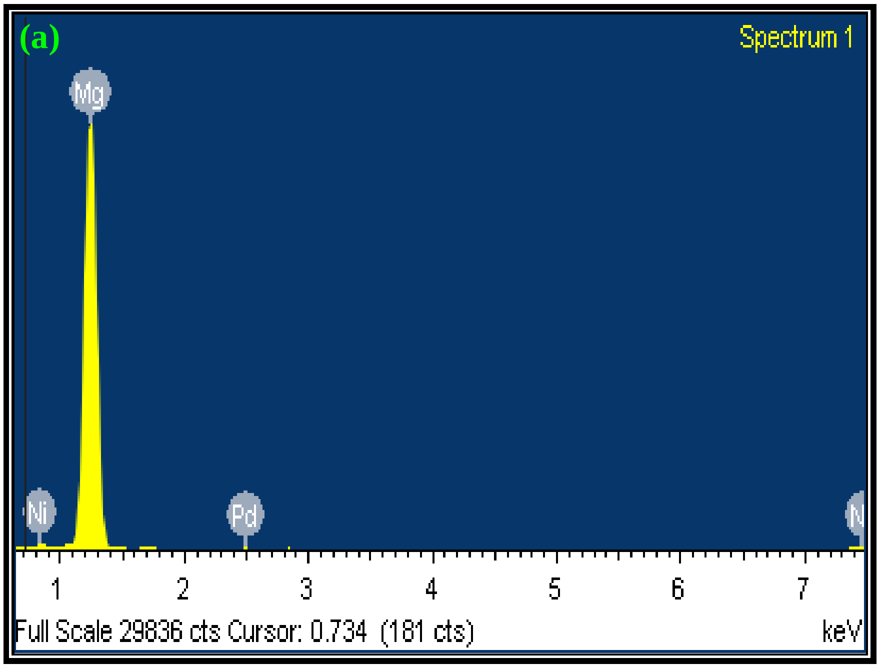

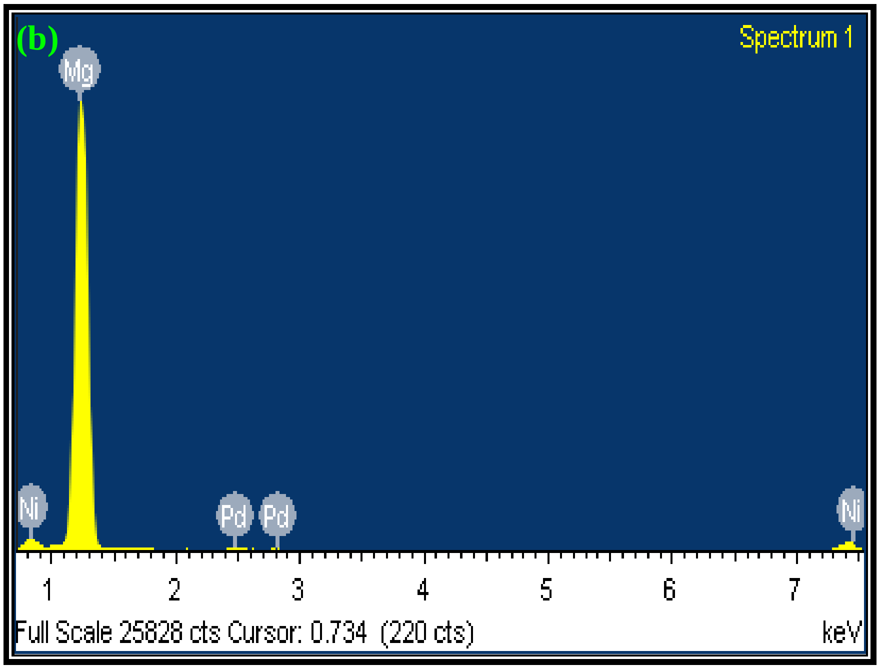

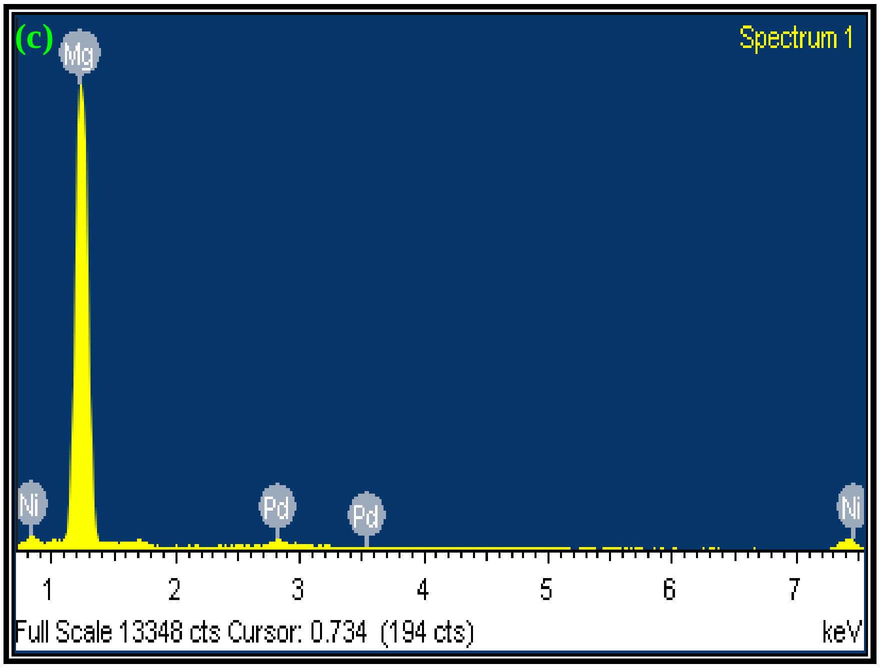

Fig. 4.28: EDS spectra of different Mg–Pd–Ni compositions for 40 h milled: (a) MP1, (b) MP2 and (c) MP3

The XRD spectra of the synthesized Mg–Pd–Ni compositions are presented in Fig. 4.29 (a). The diffraction peaks could be accurately indexed and correlated with Mg phase, Pd phase, Ni phase and Mg_6Pd phase. The Bravais lattice system of these phases being hexagonal (cell parameters, a: 3.2022 Å & c: 5.1991 Å), cubic (cell parameter a: 3.8898 Å), cubic (cell parameter a: 3.5175 Å) and cubic (cell parameter a: 20.1080 Å), respectively. Further, the FWHM (full width – half maxima) extent and the mean crystallite/grain sizes of unhydrided Mg–Pd–Ni compositions are computed and shown in Table–4.7. This data indicates that as the palladium concentration increases, the FWHM extent increases and crystallite size is decreased for same milling time (40 h milled sample). The FWHM (full width – half maxima), the mean crystallite/grain size and relative intensity of the highest intensity peak of unhydrided MP2 coded composition, at various milling times, are presented in Table–4.8. The data shown in this table clearly indicates the presence of effect of milling on the crystallite size. The hydrided sample corresponding to the optimized composition (coded MP2) was also subjected to XRD analysis.

Table–4.7: Crystallite parameters of different Mg–Pd–Ni compositions for 40 h milling time

Sr. No.	Compositions code	FWHM, degree	Crystallite size, nm	Relative intensity ratio
1	MP1	0.351°	23.85	16
2	MP2	0.371°	22.55	10
3	MP3	0.434°	19.28	6

Table–4.8: Crystallite parameters of MP2 composition for different milling times

Sr. No.	Milling time, h	FWHM, degree	Crystallite size, nm	Relative intensity ratio
1	20 h	0.356 °	23.50	14
2	40 h	0.371 °	22.55	10
3	60 h	0.388 °	21.57	8

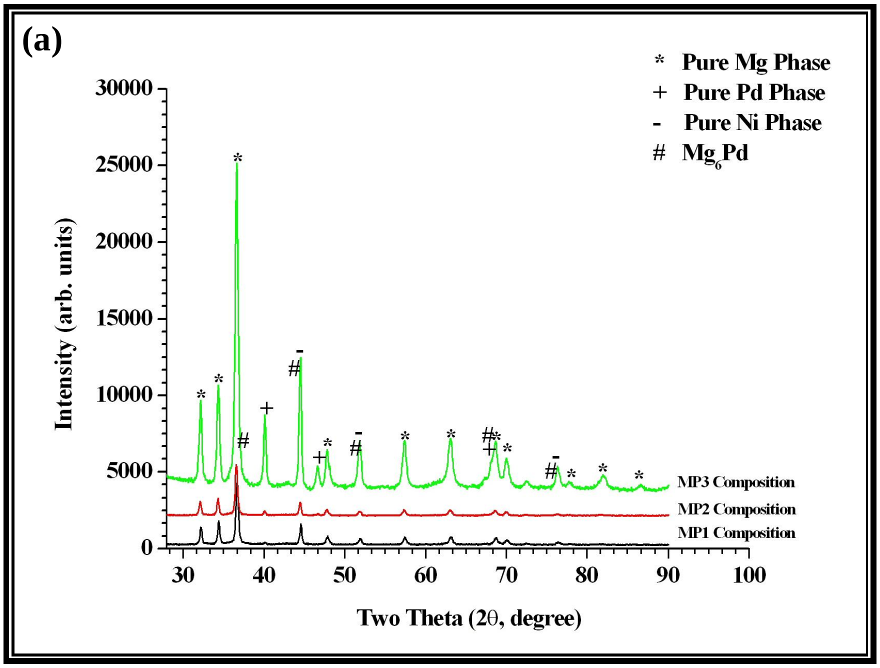

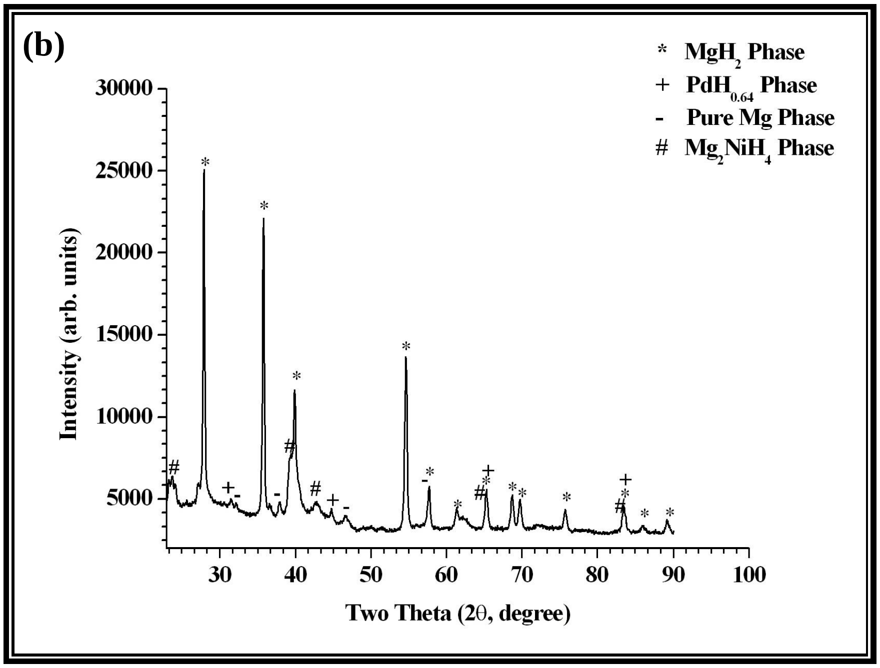

Fig. 4.29: XRD spectra of the different Mg–Pd–Ni compositions: (a) Unhydrided compositions and (b) Hydrided MP2 coded composition

Fig. 4.29 (b) shows the diffraction spectra of this composition. It is seen that the hydrided composition contains various hydrided phases such as MgH_2, Mg_2NiH_4, $PdH_{0.64}$, as well as non hydrided phase, pure Mg. The Bravais lattice system of these phases is determined to be tetragonal (cell parameters, a: 4.5170 Å & c: 3.0205 Å), orthorhombic (cell parameter a: 11.4340 Å, b: 11.2570 Å & c: 4.5190 Å), tetragonal (cell parameters, a: 4.0000 Å & c: 4.0000 Å), and hexagonal (cell parameters, a: 3.2022 Å & c: 5.1991 Å), respectively. Further, the mean crystallite/grain sizes of these phases are 34.62 nm for MgH_2, 9.41 nm for Mg_2NiH_4, 8.22 nm $PdH_{0.64}$, and 50.04 nm for Mg phase

4.4.3 Hydriding and Dehydriding Analysis

Fig. 4.30 presents the effect of different Mg–Pd–Ni compositions on mass percent of Hydrogen absorbed for a 40 h milled samples at 200 °C. These plots clearly show that the highest absorption of Hydrogen occurs for composition coded MP2. It can be also seen from this plot that the mass% of absorbed Hydrogen of composition MP1 is lower in comparison to MP2 and MP3 compositions.

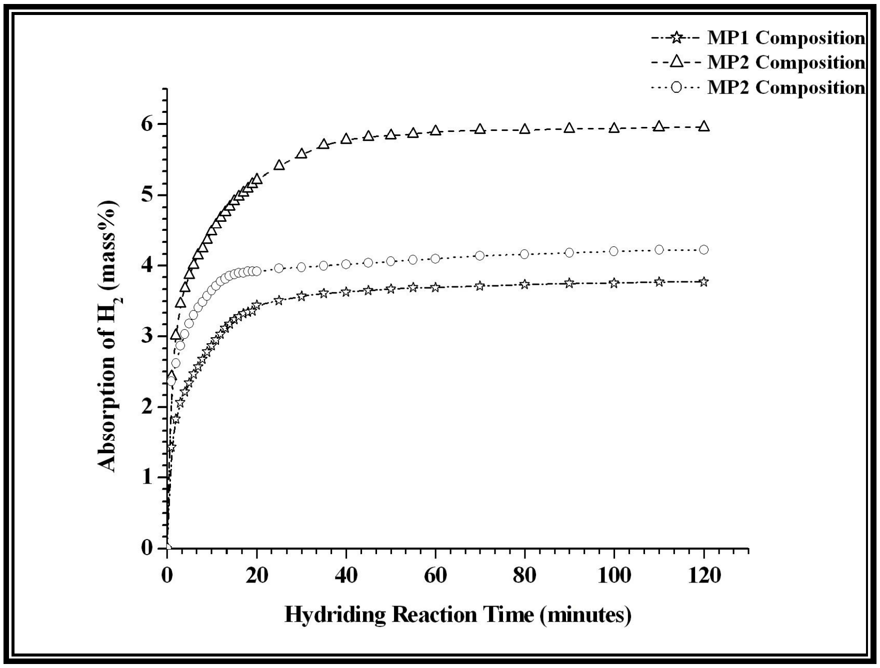

Fig. 4.30: Charging kinetics of the different Mg–Pd–Ni compositions

Fig. 4.31(a) presents the effect of milling time on mass percent of hydrogen absorbed for MP2 composition at 200 °C. This plot clearly shows that the highest absorption of Hydrogen occurs for the 40 h milled sample. Thus, hydrogen up take capacity is increased up to 40 h milling time followed by a decreasing trend beyond 40 h milling time.

Similarly, Fig. 4.31(b) is shown effect of charging pressure on H_2 absorption for MP2 coded composition at 200 °C. It is clearly indicated that the hydrogen absorption capacity increases up to 20 bar. MP2 coded composition shows 3.98 mass% of reversible H_2 storage at a charging temperature of 202 ºC and pressure of 10 bar. This enhancement is due to presence of Pd as catalyst as reported by Zaluska et al [17]. Beyond 20 bar, further hydrogen up-take capacity is decreased.

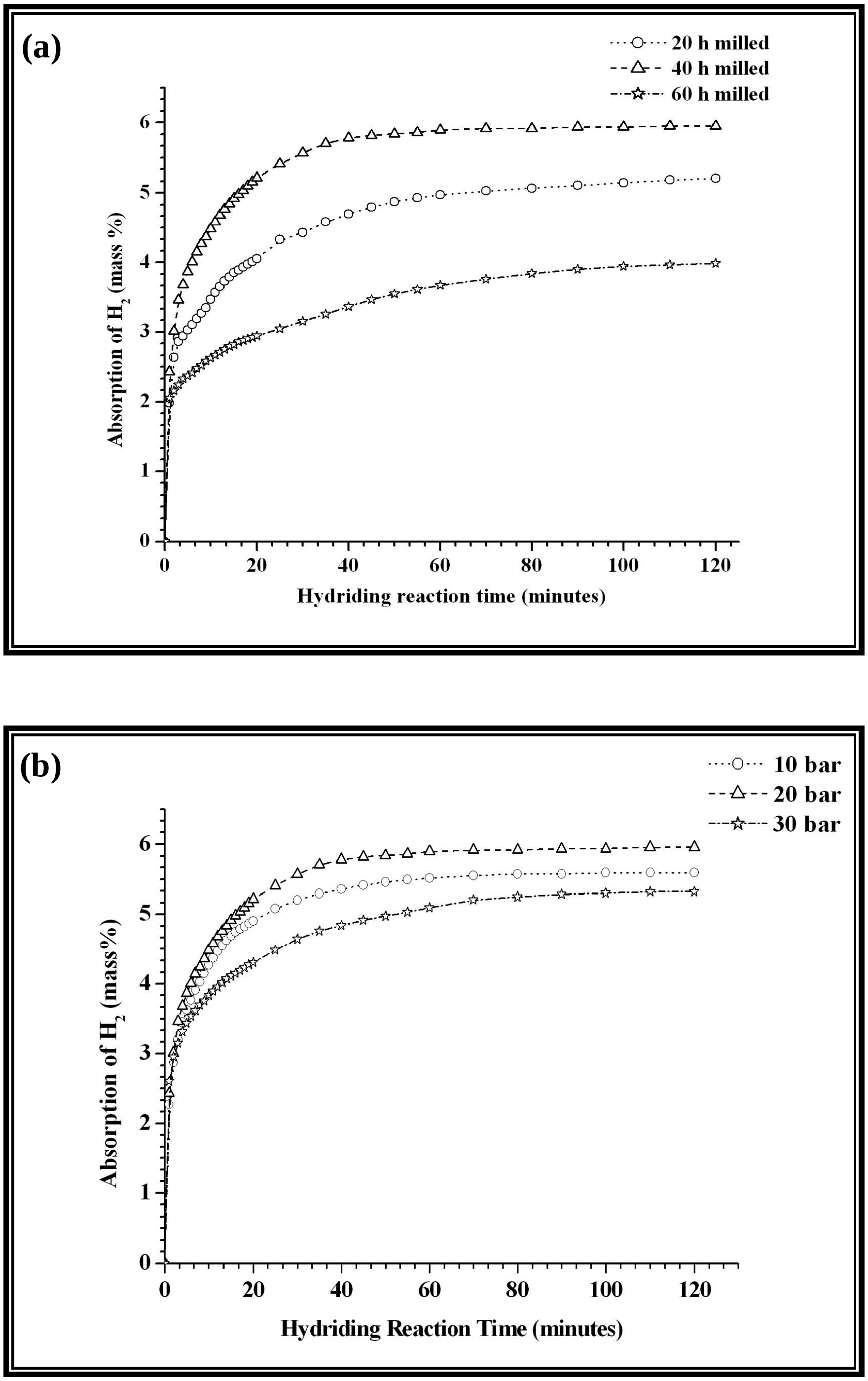

Fig. 4.31: Charging kinetics of MP2 coded composition: (a) Different milling time and (b) Different charging pressure

Fig. 4.32 shows the effect of hydriding temperature on mass% of absorbed Hydrogen for different compositions for a 40 h milled sample. Fig. 4.32(a) presents plots of absorbed Hydrogen versus hydriding reaction time for composition MP1 for different temperatures at 40 h milling. These graphs indicate that the mass % of Hydrogen absorbed increases up to 201 °C and, thereafter, H_2 storage capacity decreases with temperature. Similarly, Figs. 4.32(b) and 4.32(c) show the hydriding kinetics for compositions coded MP2 and MP3, respectively. It is also clearly indicated that 90% – 95% Hydrogen is absorbed within first 15 to 20 minutes. In general, the enhanced reaction kinetics appears to be associated with the catalytic effect of Pd and Ni [23, 24].

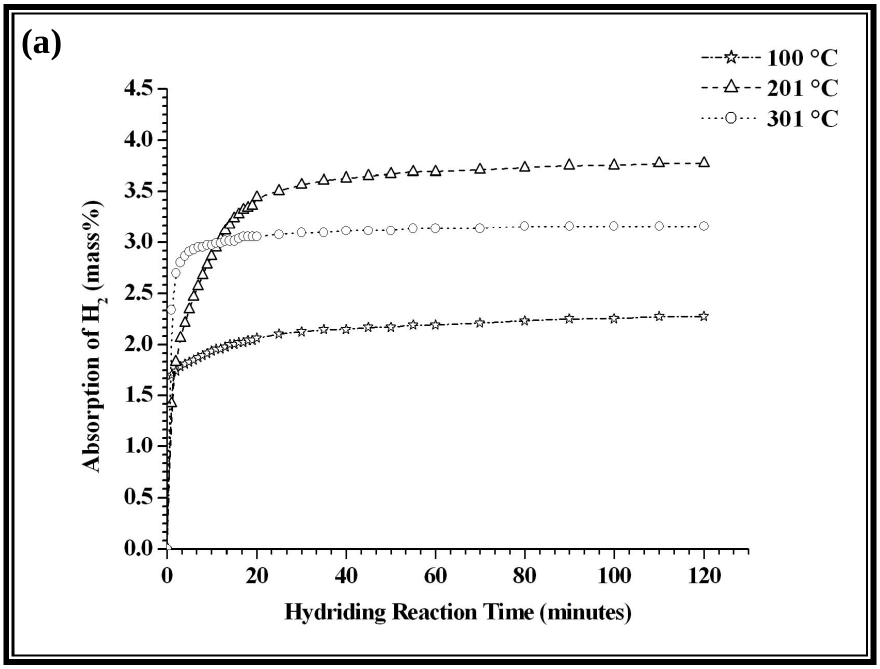

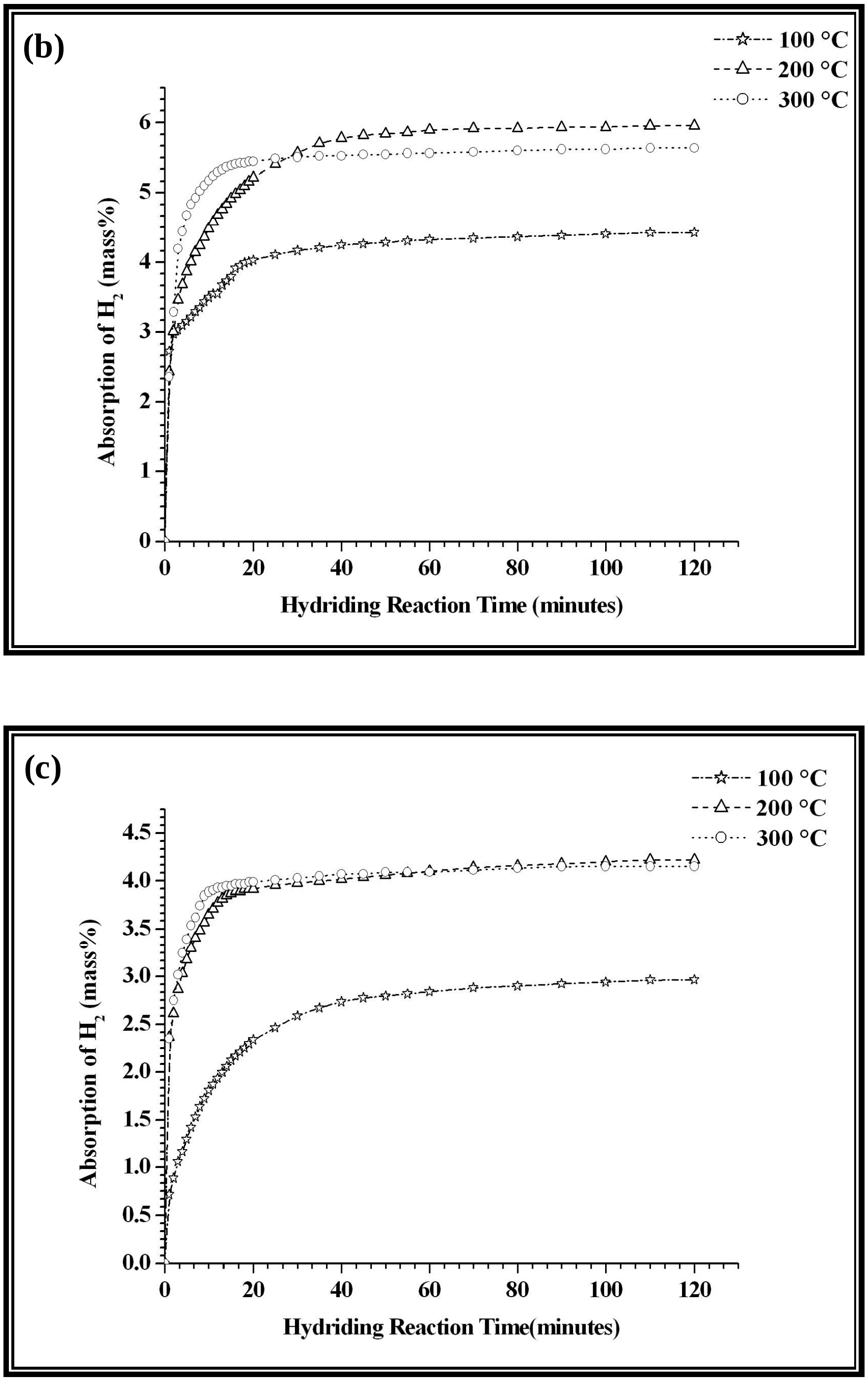

Fig. 4.32: Charging kinetics of the different Mg–Pd–Ni compositions: (a) MP1, (b) MP2 and (c) MP3

Fig. 4.33 shows the effect of dehydriding temperature and alloy composition on mass percent of Hydrogen desorbed for the 40 h milled samples. This graph indicates that the mass percent of Hydrogen desorption increases with increasing temperature for all three compositions. Specifically, note that the maximum mass % of hydrogen is desorbed at 350 °C. Note also that for all three compositions, the dehydriding time is nearly same (~ 8 to 10 minutes) at the three temperatures investigated.

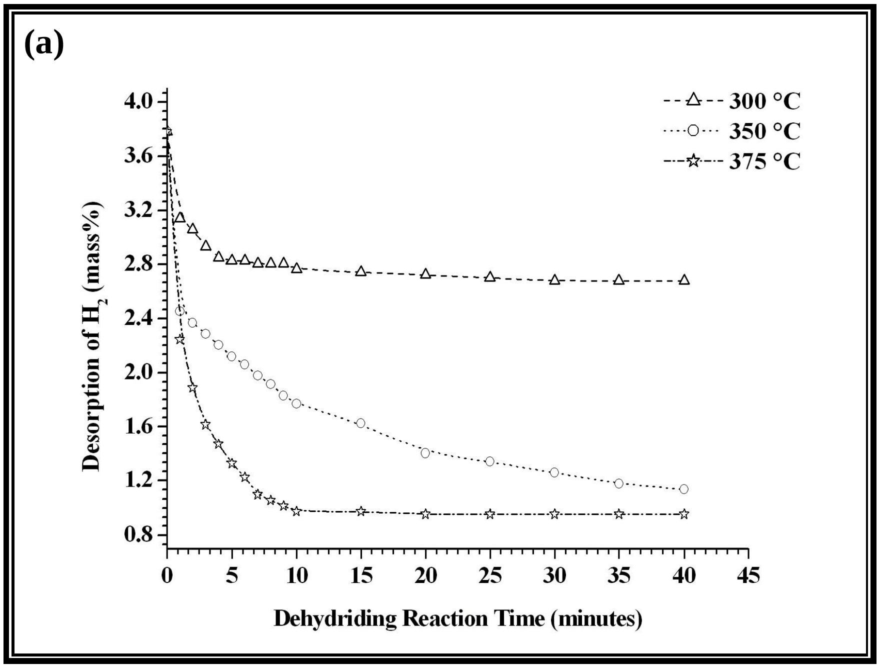

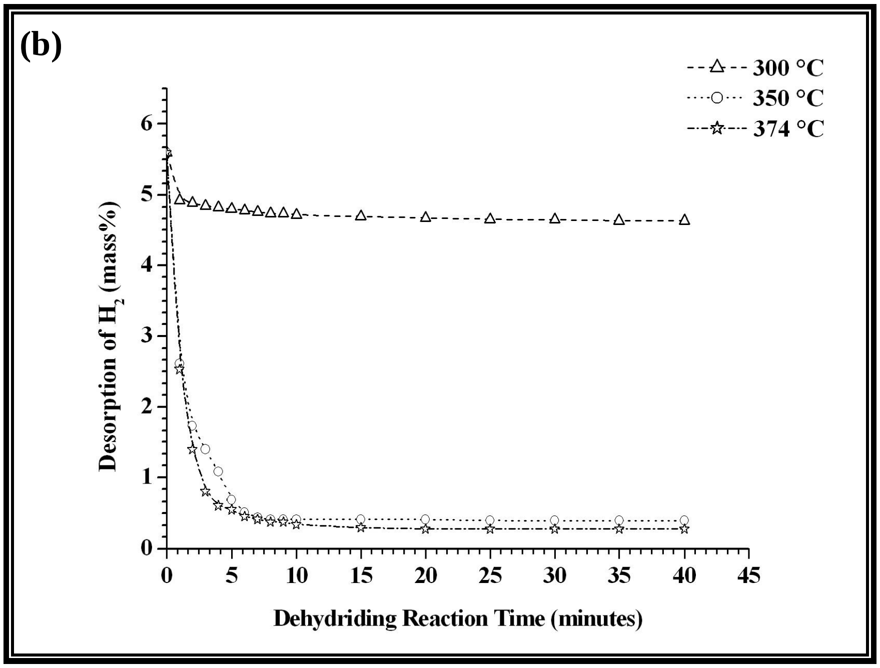

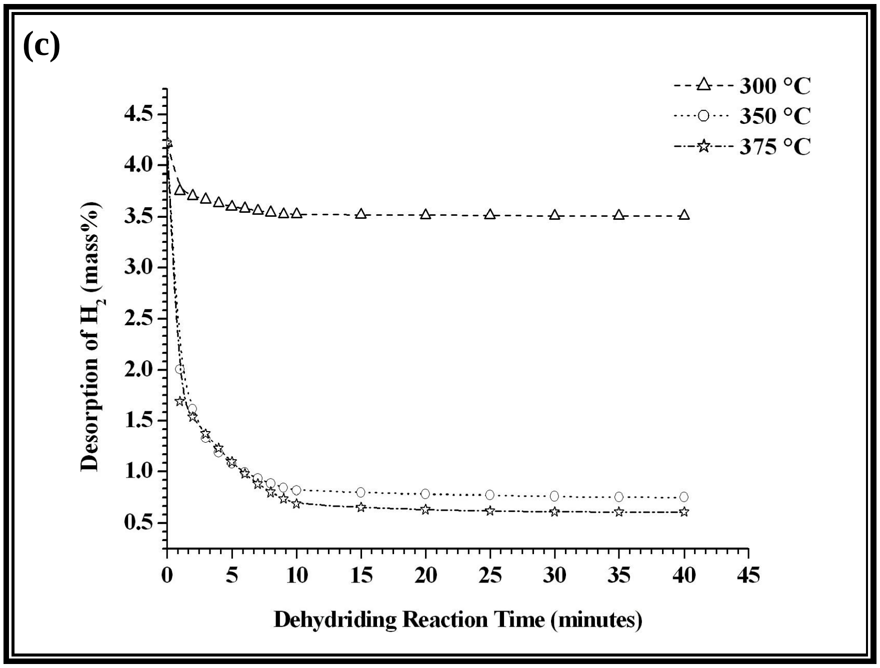

Fig. 4.33: Discharging kinetics of the different Mg–Pd–Ni compositions: (a) MP1, (b) MP2 and (c) MP3

4.4.4 Deviations in Hydriding and Dehydriding Kinetics due to Departure from Ideal Gas Behavior of Hydrogen

In Fig. 4.34(a), the mass% of hydrogen absorbed versus time data, computed using the ideal gas equation as well the three real gas equations of state is presented for the optimized MP2 coded composition. For this alloy, the maximum absorption capacity is computed as 5.90 mass% using the ideal gas equation, and 5.62, 5.63 and 5.61 mass% using Van–der–Waal, Redlich–Kwong and Redlich–Kwong–Soave equations, respectively. The percent deviations from ideal gas computations are plotted as a function of time in Fig. 4.34(b). The percentage deviations in the hydriding kinetics data is obtained as 4.78 %, 4.55 % and 4.85 % for Van–der–Waal, Redlich–Kwong and Redlich–Kwong–Soave equations, respectively. Clearly, significant deviation occurs in predicting the reacted mass of hydrogen using the ideal gas model.

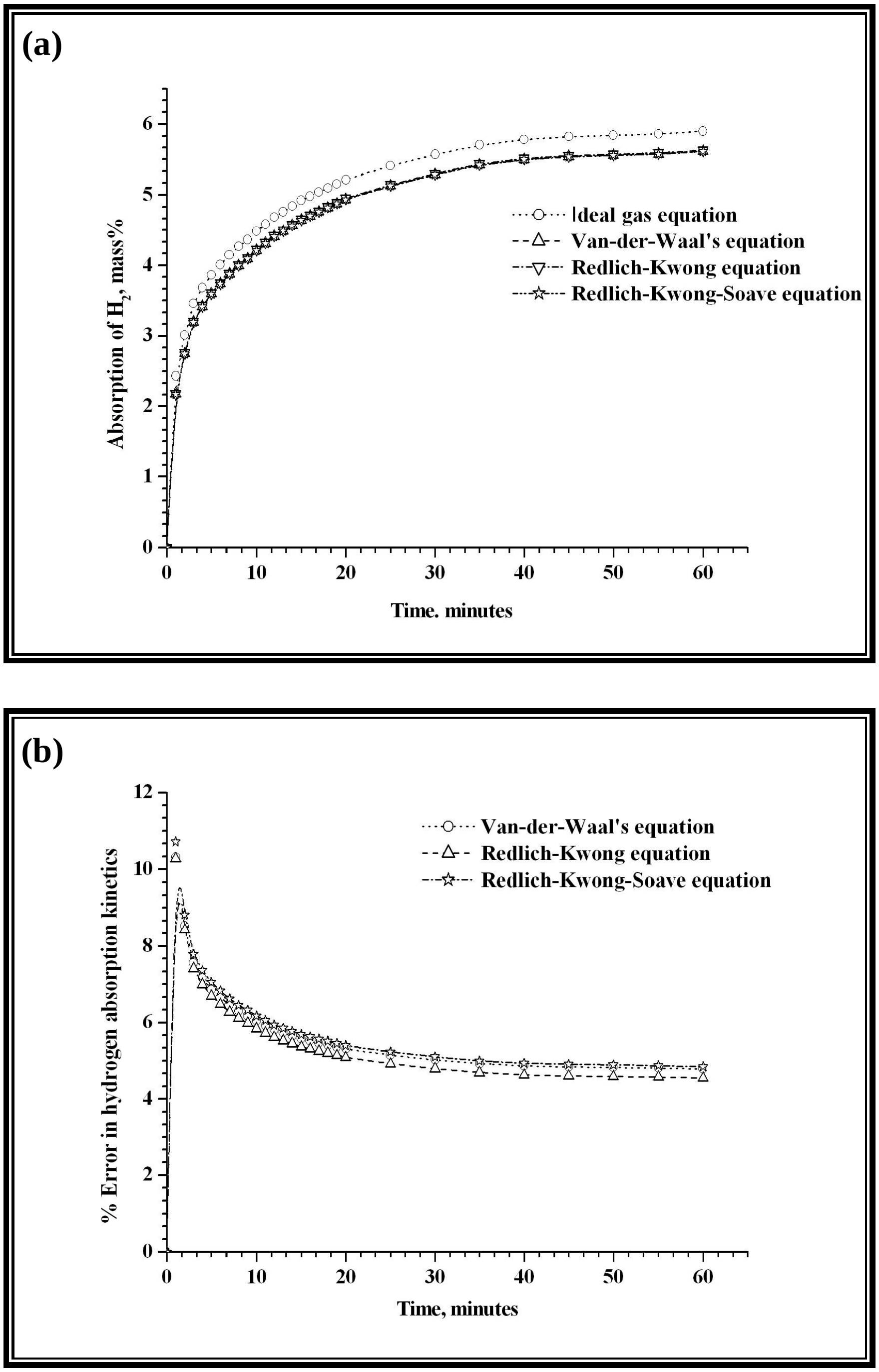

Fig. 4.34: Hydriding characterization of MP2 coded alloy composition using ideal and real gas equations: (a) H_2 absorption versus time and (b) Deviation in absorption from ideal gas equation

In Fig. 4.35(a), the mass % of hydrogen desorbed versus time data is computed using the ideal gas equation as well the three real gas equations of state for the optimized MP2 coded composition. For this composition, the maximum desorption capacity is computed as 5.16 mass% using the ideal gas equation and 4.92, 4.93 and 4.92 mass% using Van–der–Waal, Redlich–Kwong and Redlich-Kwong-Soave equations, respectively. The percent deviations are plotted as a function of time in Fig. 4.35(b). The percentage observed deviation of hydrogen desorption using ideal gas equation with respect to the three real gas equations are obtained as 4.46 %, 4.44 % and 4.46 %, respectively.

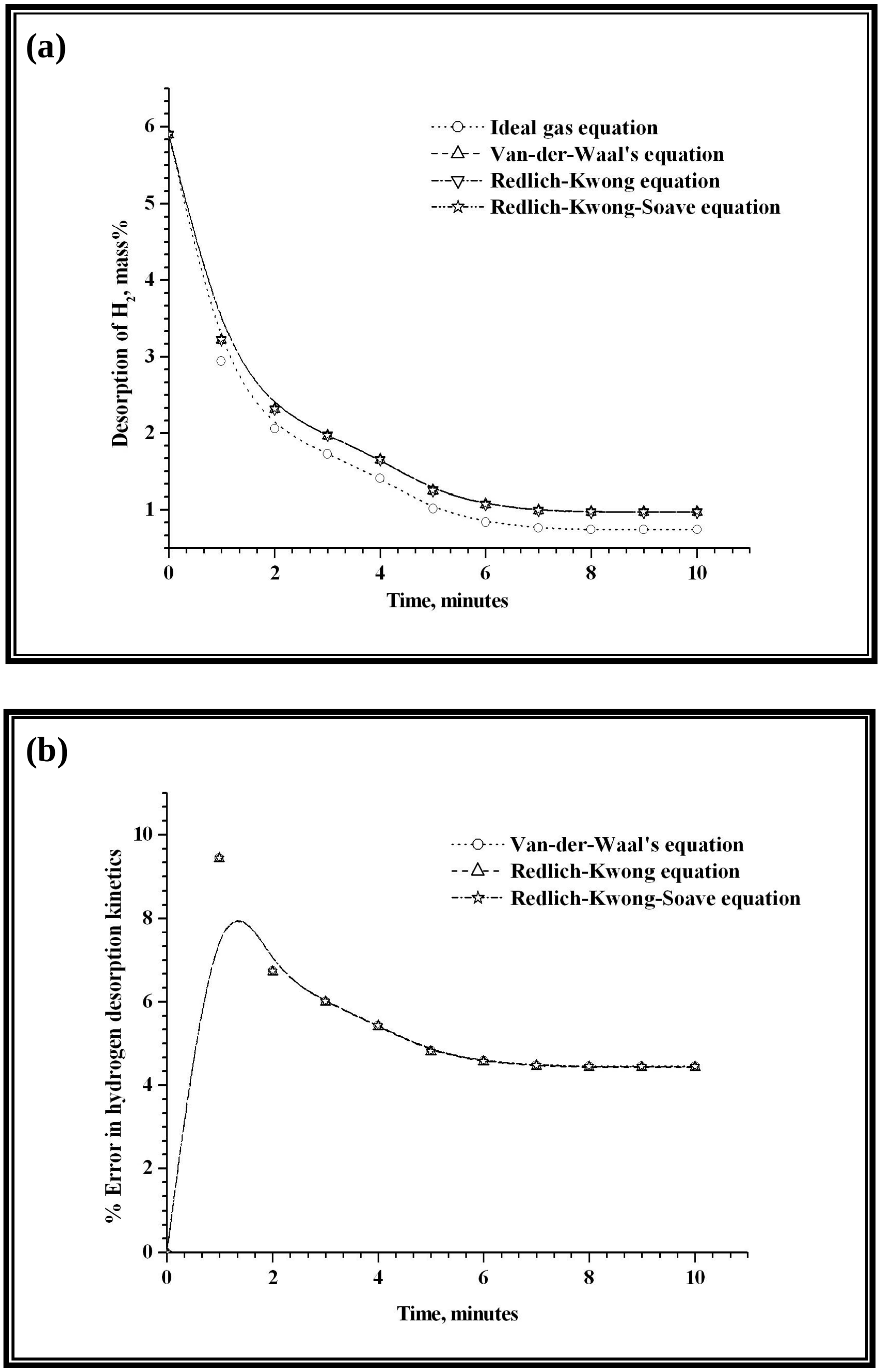

Fig. 4.35: Dehydriding characterization of MP2 coded alloy composition using ideal and real gas equations: (a) H_2 desorption versus time and (b) Deviation in desorption from ideal gas equation

4.4.5 Reaction Kinetics Modelling Analysis

The experimental data of the optimized MP2 coded alloy composition at 200 ºC is first modelled using a first-order lumped exponential response model of the form as presented in chapter 2 (section 2.5.1, Eqns. 2.16 and 2.20). The experimental constants in these two equations are determined using linear regression and predictions of the estimated models are compared with experimental data in Fig. 4.36 (a) and (b). For the charging model, the estimated values of the constants are determined as: $\hat{\alpha}_c = 5.90$ & $\hat{\beta}_c = 0.11$, with coefficient of correlation obtained as:

$$\left(R_0^2\right)_{Ch\arg ing} = 0.88 \qquad \text{--------------------- (4.15)}$$

Similarly, for the discharging model, the estimated constants are determined as: $\hat{\alpha}_d = 5.59$ & $\hat{\beta}_d = 0.38$, with coefficient of correlation obtained as:

$$\left(R_0^2\right)_{Disch\arg ing} = 0.89 \qquad \text{--------------------- (4.16)}$$

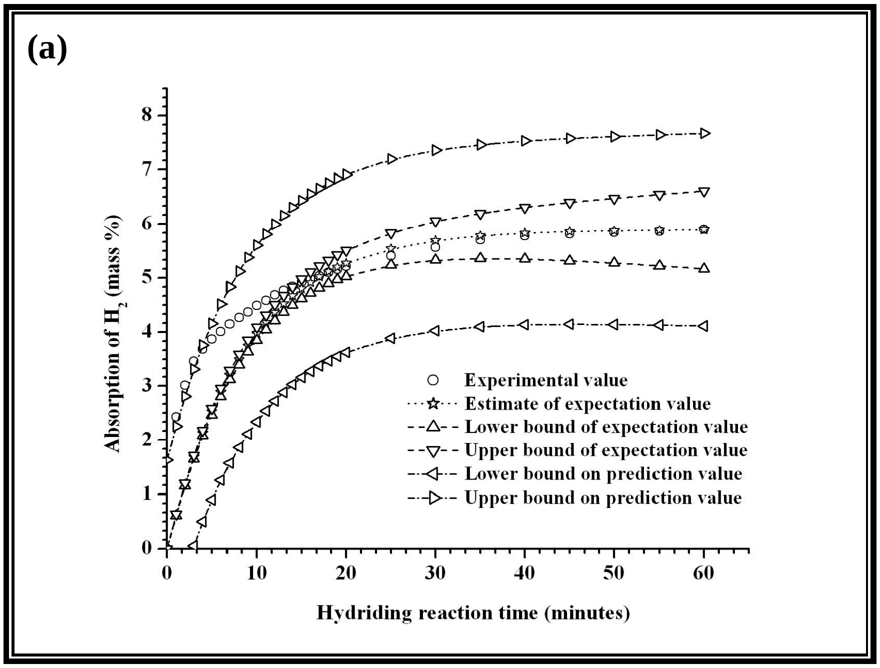

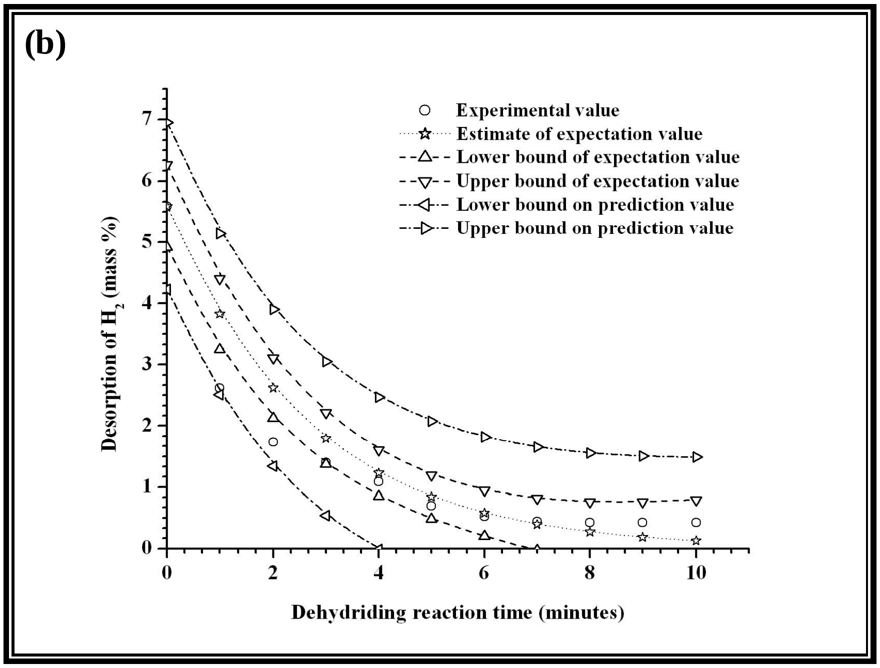

Fig. 4.36: Model fits for experimental data using lumped first order kinetics model for the optimized MP2 coded composition: (a) Charging kinetics and (b) Discharging kinetics

The value of $\left(R_0^2\right)_{Charging}$ indicates that the linear model used is not able to explain 12 % of charging data variability. Similarly, the value of $\left(R_0^2\right)_{Discharging}$ indicates that about 11 % of discharging data variability remains unexplained. While these values indicate reasonable fit, clearly the correlation can be improved by a more elaborate model.

Shrinking core model applies for fitting the hydrogen absorption data for optimized MP2 composition at 200 ºC. Equations described in chapter 2 (section 2.5.2, Eqns. 2.22, 2.23 and 2.24) are compared with the experimental results in Fig. 4.37(a). These graphs indicate that the full form, shrinking core model, given by Eq. (2.22) gives a better estimation of the experimental data. However, clearly both the individual pure chemical and diffusion control models (simplified models) are not adequate to characterize the experimental data. For this purpose of fitting the full Shrinking core model, a numerical statistical factorial experiment in the dimensionless space of t^*, ϕ_1 and ϕ_2 has been used. Using a minimum variance non-linear optimization scheme, the best fit corresponding to mass transfer coefficient in gas phase, k_α of 1 × 10^{-6} m/s and reaction rate constant, k_r of 9 × 10^{-6} m/s have been obtained. For this optimization, value of the diffusion coefficient through species βH_2 of α, D_P is taken as 9.77×10^{-9} m^2/s (reported by Nishimura et al [21]) and mean radius of spherical particles, r_p is 6.14 × 10^{-6} m (measured using SEM).

In Fig. 4.37(b), the Johnson–Mehl–Avrami (JMA) model has fitted, representing a generalized case of random nucleation and growth in the optimized MP2 coded composition. In the JMA model, nucleation occurs randomly. The JMA equation has been given in chapter 2 (section 2.5.3, Eqns. 2.25 and 2.26). For the JMA full linear regression model, a co-efficient of correlation, R^2 is obtained as 0.9932, and the Avrami exponent, n is 0.57. Note also that in about 120 s, the transformed fraction of the hydride reaches about 67 %.

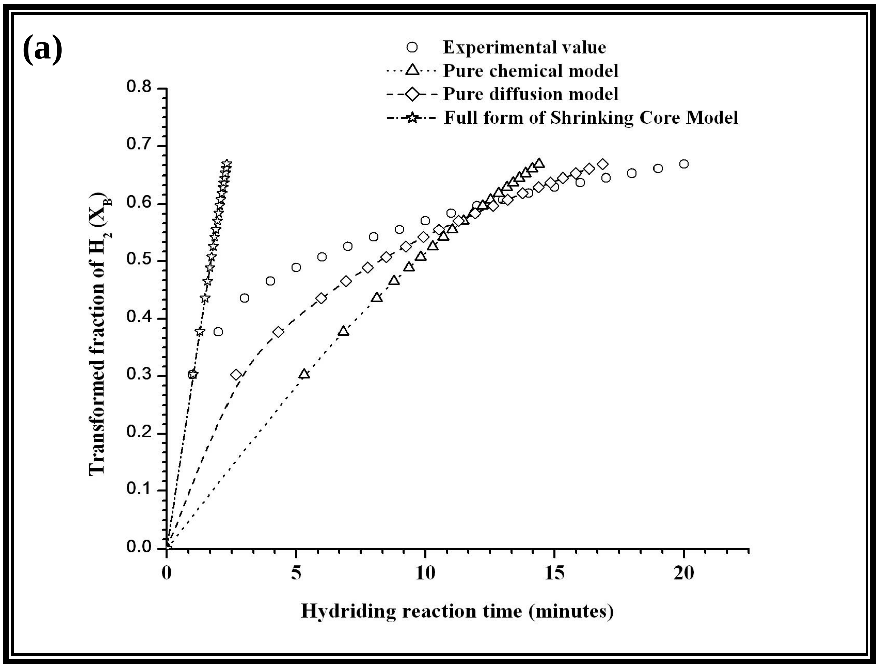

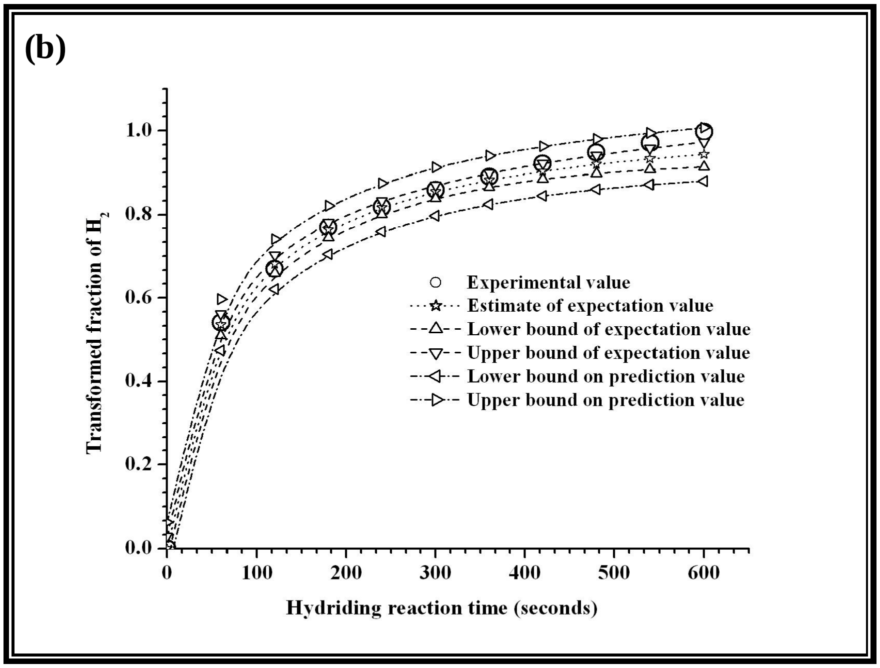

Fig. 4.37: Model fits for experimental data using different models for the optimized MP2 coded composition: (a) Shrinking core model and (b) Johnson–Mehl–Avrami model

4.4.6 Prediction of Formation Enthalpy and Entropy

The formation enthalpy and entropy during dehydriding reaction are estimated by Van't Hoff relation, which is detailed in chapter 3. Using Van't Hoff relation, the enthalpy of formation (ΔH_0) of the optimized MP2 (40 h milled) composition is determined as 71.9 kJ/mole of H_2, and the entropy (ΔS_0) is computed as 126.3 J/mole of H_2 K. Using the experimental results and statistical error expressions, the uncertainty associated with enthalpy is obtained as 7.8 % and uncertainty associated with entropy is 4.8 %. Therefore, the enthalpy of formation can be stated 71.9 ± 5.6 kJ/mole of H_2, and the entropy can be stated as 126.3 ± 6.1 J/mole of H_2 K. The logarithmic plot of equilibrium pressure versus temperature (Van't Hoff relationship) is compared with experimental/obtained values (with the coefficient of correlation, R^2_0 as 0.9333, see Fig. 4.38).

The experimentally extracted value for $\overline{\Delta H}$ by the DSC method (see Fig. 4.39) is 68.2 ± 5.3 kJ per mole of hydrogen for optimized MP2 coded composition. Further, if one assumes the dehydriding reaction in the DSC to be close to equilibrium (which is thermodynamically unlikely), “pseudo specific entropy”, $\overline{\Delta S_{pseudo}}$ can be computed as 116.9 ± 5.6 kJ per (mole of H_2) K. It is to be noted that the pseudo entropy is computed under “far from equilibrium” conditions and, hence, is not expected to be close to the entropy obtained using Van’t Hoff analysis.

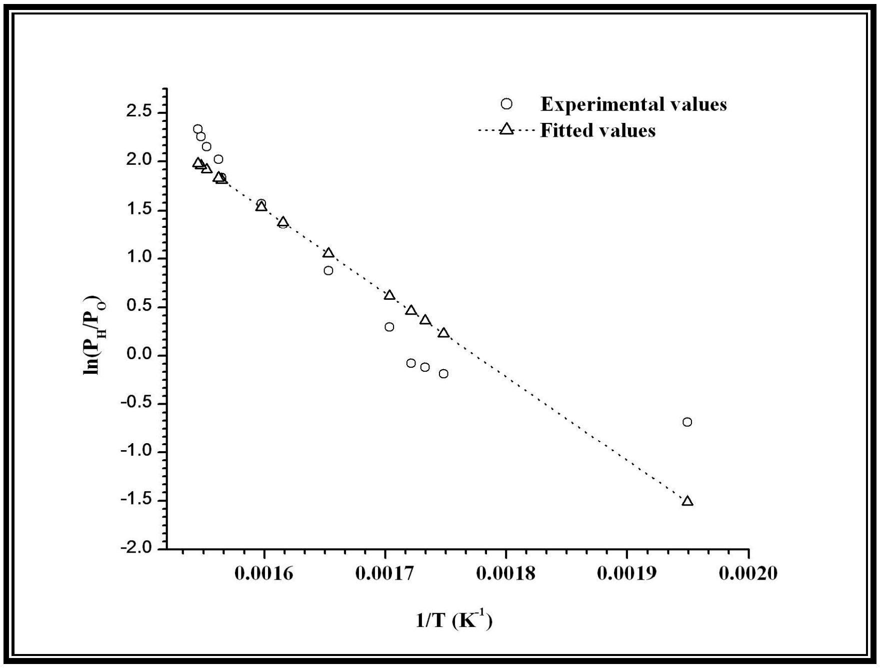

Fig. 4.38: Experimental and derived pressure ratio versus inverse temperature (using Van’t Hoff equation) for optimized MP2 composition

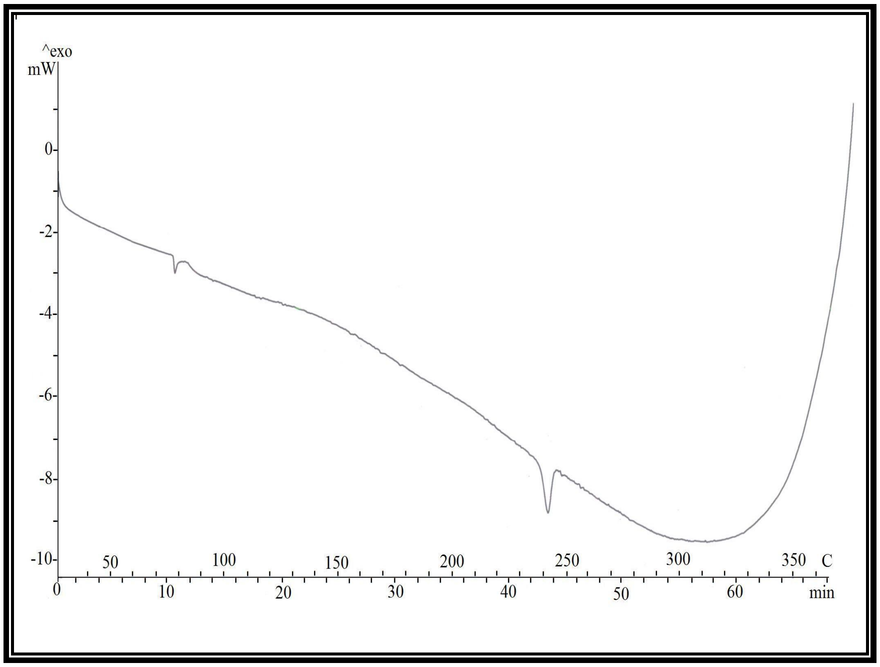

Fig. 4.39: Electrical power absorbed during DSC test versus time/temperature plot for optimized MP2 coded hydride composition

4.5 Quaternary Mg–Zr–Mn–Ni Alloy Compositions

4.5.1 Sample Preparation

The quaternary Mg–Zr–Mn–Ni system is synthesized using Mg, Zr, Mn and Ni powders with a minimum of 99% purity. The milling experiments are conducted in a planetary ball mill. The detailed technical parameters of ball mill are presented in chapter 3. The chemical composition of various Mg–Zr–Mn–Ni compositions are prepared with greater than or equal to 81 at% of Magnesium, 5 at% of Nickel and 2.5 at% to 7.0 at% of (Zr–Mn). The weight calculations of individual elements of these compositions are given as under:

The atomic fraction of each element in the $Mg_{90\%}(Zr–Mn)_{2.5\%}Ni_{5\%}$ composition is computed as below:

$$Mg^{af} = \frac{Mg^{w}/Mg^{aw}}{Mg^{w}/Mg^{aw} + Zr^{w}/Zr^{aw} + Mn^{w}/Mn^{aw} + Ni^{w}/Ni^{aw}} \quad \text{---------------------} \ (4.17)$$

$$Zr^{af} = \frac{Zr^{w}/Zr^{aw}}{Mg^{w}/Mg^{aw} + Zr^{w}/Zr^{aw} + Mn^{w}/Mn^{aw} + Ni^{w}/Ni^{aw}} \quad \text{---------------------} \ (4.18)$$

$$Mn^{af} = \frac{Mn^{w}/Mn^{aw}}{Mg^{w}/Mg^{aw} + Zr^{w}/Zr^{aw} + Mn^{w}/Mn^{aw} + Ni^{w}/Ni^{aw}} \quad \text{---------------------} \ (4.19)$$

$$Ni^{af} = \frac{Ni^{w}/Ni^{aw}}{Mg^{w}/Mg^{aw} + Zr^{w}/Zr^{aw} + Mn^{w}/Mn^{aw} + Ni^{w}/Ni^{aw}} \quad \text{---------------------} \ (4.20)$$

Where, Mg^{af}, Zr^{af}, Mn^{af} and Ni^{af} are the atomic fraction of Mg, Zr, Mn and Ni, respectively; Mg^{w}, Zr^{w}, Mn^{w} and Ni^{w} are the weight of Mg, Zr, Mn and Ni, respectively; and Mg^{aw}, Zr^{aw}, Mn^{aw} and Ni^{aw} are the atomic weight of Mg, Zr, Mn and Ni, respectively.

Next, using Eqns. 4.13 to 4.16, weight of each element in the $Mg_{90\%}$(Zr–Mn)$_{2.5\%}$$Ni_{5\%}$ composition can be computed as:

$$Mg^{w}=\frac{Mg^{aw}\times Mg^{af}}{Mg^{af}+Zr^{af}+Mn^{af}+Ni^{af}}=21.88 \qquad \text{---------------------} \ (4.21)$$

$$Zr^{w}=\frac{Zr^{aw}\times Zr^{af}}{Mg^{af}+Zr^{af}+Mn^{af}+Ni^{af}}=2.28 \qquad \text{---------------------} \ (4.22)$$

$$Mn^{w}=\frac{Mn^{aw}\times Mn^{af}}{Mg^{af}+Zr^{af}+Mn^{af}+Ni^{af}}=1.37 \qquad \text{---------------------} \ (4.23)$$

$$Ni^{w}=\frac{Ni^{aw}\times Ni^{af}}{Mg^{af}+Zr^{af}+Mn^{af}+Ni^{af}}=2.94 \qquad \text{---------------------} \ (4.24)$$

Therefore, for 20 gm composition, the weight of Mg is computed as 15.37 gm, the weight of Zr is 1.60 gm, the weight of Mn is 0.96 gm and Ni is 2.06 gm for $Mg_{90\%}$(Zr–Mn)$_{2.5\%}$$Ni_{5\%}$ composition. Similarly, for $Mg_{85\%}$(Zr–Mn)$_{5\%}$$Ni_{5\%}$ and $Mg_{81\%}$(Zr–Mn)$_{7\%}$$Ni_{5\%}$ compositions, the weights of elements are also computed (see the Table 4.9).

Table 4.9: Elemental mass (for 20 gm) of different Mg–Zr–Mn–Ni compositions

Sr. No.	**Compositions**		**Elements**			
			Mg	**Zr**	**Mn**	**Ni**
1.	MZ1	*Atomic %*	90.00	2.50	2.50	5.00
		Weight %	76.86	8.01	4.82	10.31
		Mass, gm	15.37	1.60	0.97	2.06
2.	MZ2	*Atomic %*	85.00	5.00	5.00	5.00
		Weight %	66.86	14.63	8.95	9.56
		Mass, gm	13.37	2.93	1.79	1.91
3.	MZ3	*Atomic %*	81.00	7.00	7.00	5.00
		Weight %	59.93	19.43	11.70	8.94
		Mass, gm	11.98	3.89	2.34	1.79

4.5.2 Characterization Study

Micrographs showing the morphology of the pure Zirconium and different Mg–Zr–Mn–Ni compositions are shown in Fig. 4.40. The mean particle size of pure Zr is measured as 588 ± 257 µm. Further, the images of the alloy compositions show the presence of secondary particulates in the form of sub-microscopic satellites, which are bonded onto the larger Mg particles, SEM analysis clearly confirmed the brighter satellite particles to be elemental catalyst species (Zr, Mn and Ni). The mean particle size of Magnesium phase is measured as 16.9 ± 4.6 µm, 13.6 ± 3.9 µm, and 11.8 ± 3.7 µm for MZ1, MZ2 and MZ3 compositions, respectively. Moreover, the homogeneity of synthesized alloy compositions is increased with increasing concentration of (Zr–Mn) elements.

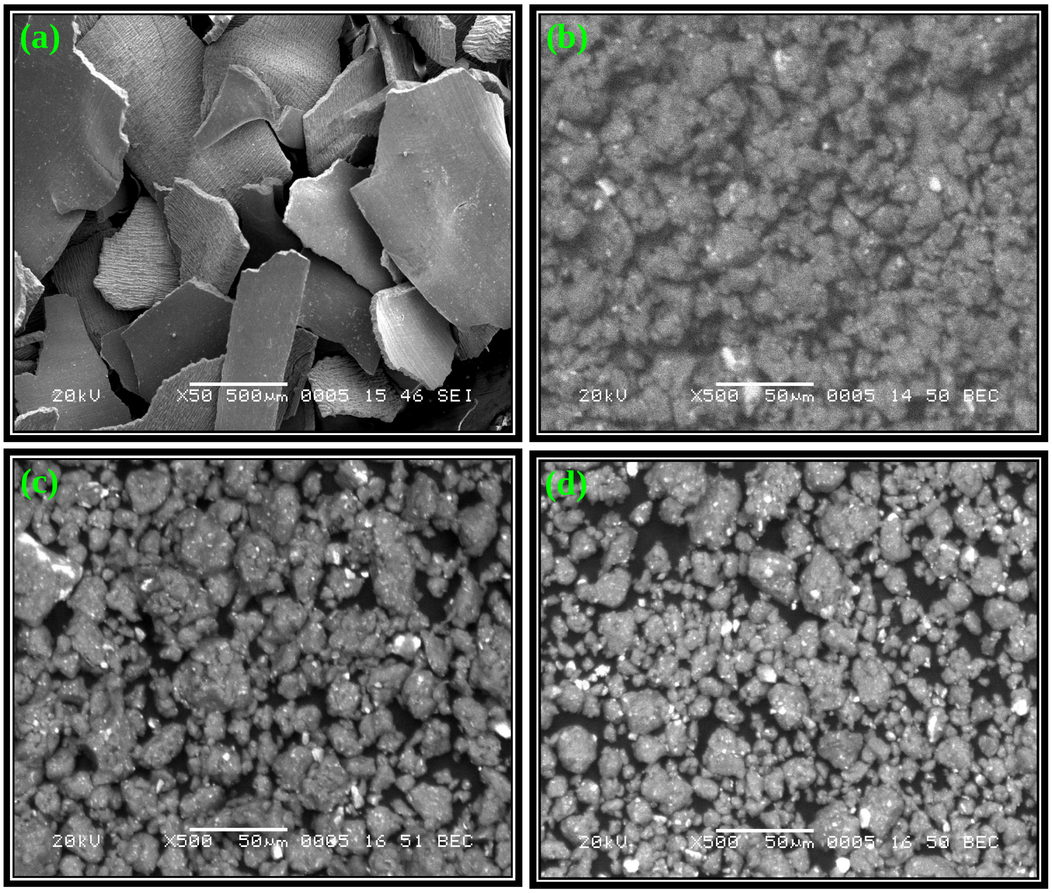

Fig. 4.40: SEM micrographs: (a) Pure Zirconium and synthesized Mg–Zr–Mn–Ni compositions (b) MZ1, (c) MZ2 and (d) MZ3

EDS analysis was conducted in SEI (secondary electron image) mode at accelerating voltage of 20 kV on the three synthesized alloys (coded MZ1, MZ2 and MZ3, respectively). Results (presented in Table–4.10) indicate that the measured elemental compositions are closely matched with those targeted compositions. The EDS spectra of the three alloy compositions are shown in Fig. 4.41.

Table-4.10: The elemental compositions of the synthesized alloys

Sr. No.	**Elements**	**Composition, Atomic %**	**Alloy Code**		
			MZ1	**MZ2**	**MZ3**
1	Mg	Target	90.0	85.0	81.0
		Obtained	92.6	88.9	85.1
2	Zr	Target	2.5	5.0	7.0
		Obtained	1.6	3.9	6.3
3	Mn	Target	2.5	5.0	7.0
		Obtained	1.4	3.0	4.0
4	Ni	Target	5.0	5.0	5.0
		Obtained	4.4	4.2	4.6

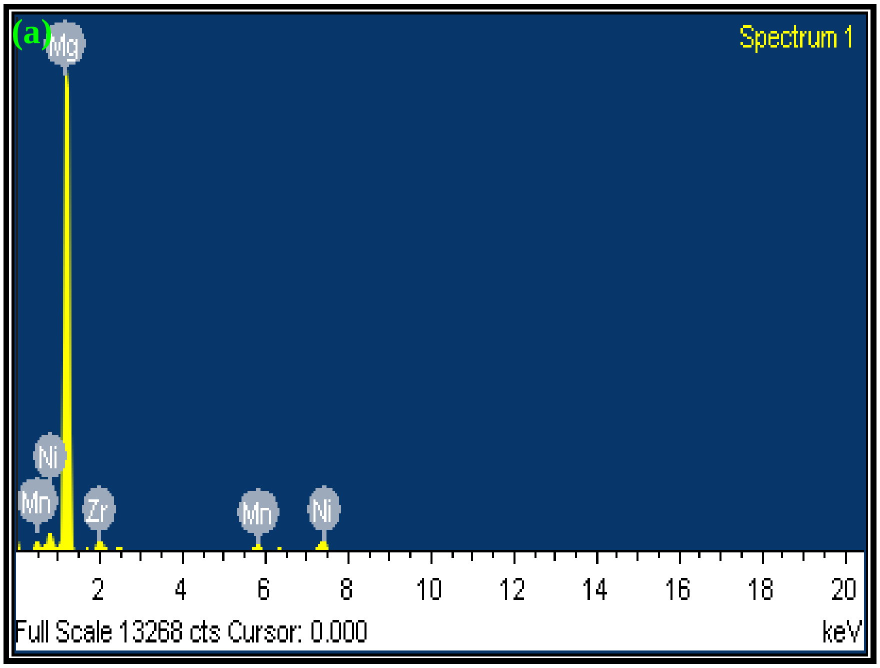

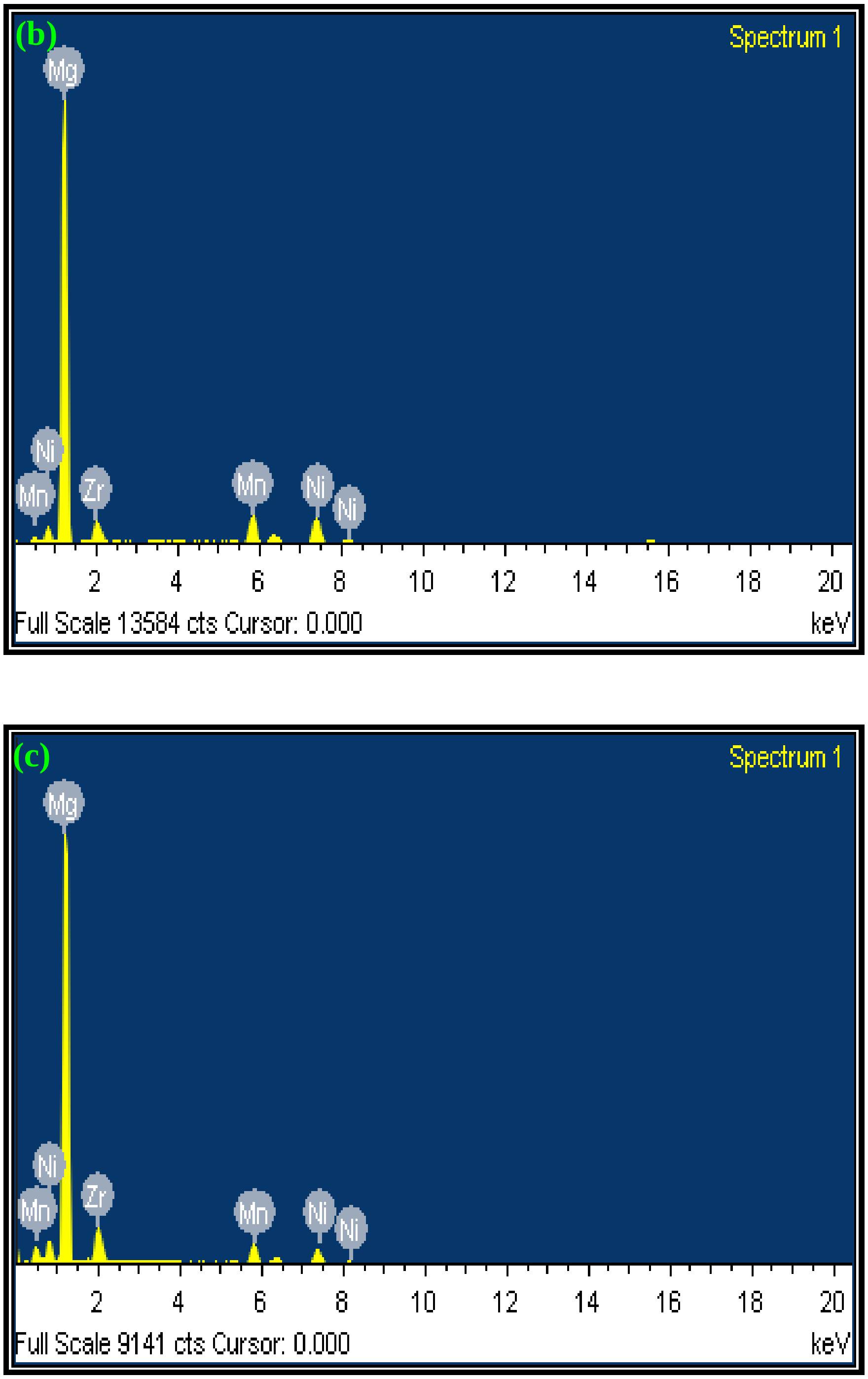

Fig. 4.41: EDS spectra of different Mg–Zr–Mn–Ni compositions for 40 h milled: (a) MZ1, (b) MZ2 and (c) MZ3

The XRD spectra of the various Mg–Zr–Mn–Ni synthesized alloys are presented in Fig. 4.42(a). All the predominant peaks corresponding to Mg, Zr, Mn, Ni and $ZrMn_2$ are seen. The various diffraction peaks could be accurately indexed and correlated with Mg phase, Zr phase, Mn phase, Ni phase and $ZrMn_2$ phase. The hexagonal Bravais lattice system corresponds to Mg, Zr and $ZrMn_2$ phases, and the cubic system for Ni and Mn phases.

Crystallite parameters (presented in Table–4.11) show the mean crystallite/grain size of 7 at% Zr–Mn composition is 10.97 nm, which is lower than the crystallite size for the 2.5 at% Zr–Mn composition after 40 h milling. Increasing addition of Zr and Mn particulates provide zener pinning centres for grain boundaries and hence reversion of refined grains is prevented. As a consequence, grain size is lowered, resulting in increased high velocity hydrogen transport channels for diffusion of hydrogen through the matrix. This increases the absorption kinetics. Further, Table–4.12 clearly shows that milling time has only minor effect on mean crystallite size of Mg phase with respect to concentration variation.

Table–4.11: Crystallite parameters of synthesized alloy compositions after 40h milling

Sr. No.	Alloy Codes	FWHM, °	Crystallite Size, nm	Relative Intensity Ratio
1	MZ1	0.365°	22.29	9
2	MZ2	0.482°	17.36	7
3	MZ3	0.719°	11.32	4

Table–4.12: Crystallite parameters of optimized MZ2 coded alloy composition at different milling time

.Sr. No.	Milling Time	FWHM, °	Crystallite Size, nm	Relative Intensity Ratio
1	15h	0.425°	19.15	8
2	40h	0.482°	17.36	7
3	60h	0.491°	16.55	6

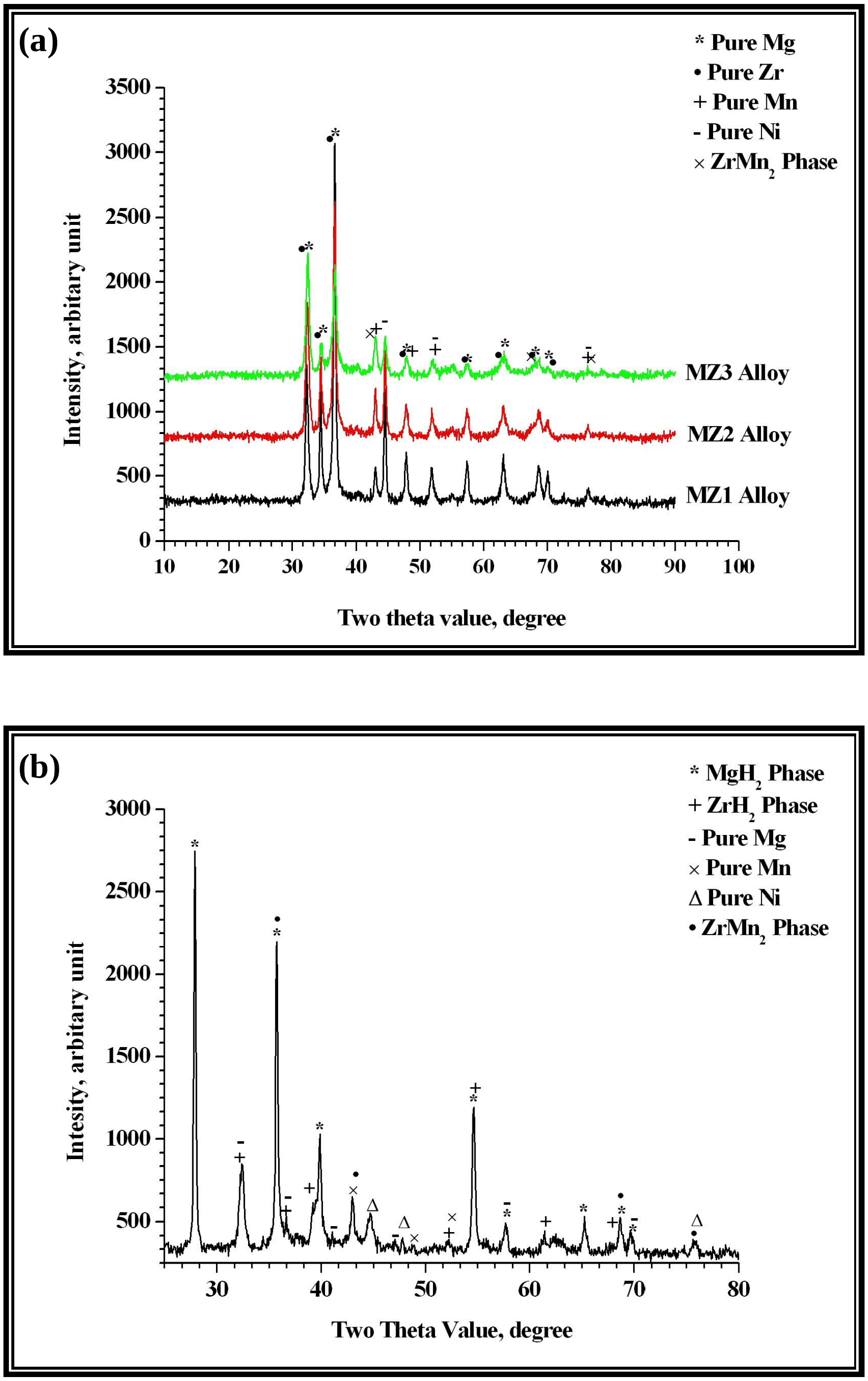

Fig. 4.42: XRD spectra: (a) Unhydrided Mg–Zr–Mn–Ni alloy compositions and (b) Hydrided alloy coded MZ2

The hydrided sample of optimized alloy coded MZ2 was also subjected to XRD analysis. Fig. 4.42(b) shows the diffraction spectra of this alloy. It is seen that the hydrided alloy contains two hydrided phases namely, MgH_2 and ZrH_2 and four unhydrided phases namely, Mg, Mn, Ni and $ZrMn_2$. The mean crystallite/grain size of these phases are 42.27 nm for MgH_2, 17.71 nm for ZrH_2, 9.18 nm for Mg, 33.64 nm for Mn, 17.34 nm for Ni and 8.33 nm for $ZrMn_2$.

4.5.3 Hydriding and Dehydriding Analysis

In Fig. 4.43 show the absorption kinetics plots at 200 °C (initial charging pressure of 30 bars) of alloy coded MZ2 for different milling times. This graph clearly shows that hydrogen up-take increases with milling time, with highest absorption occurring for 60h milled alloy. This increased uptake appears to be associated with the decreased grain size with increased milling time.

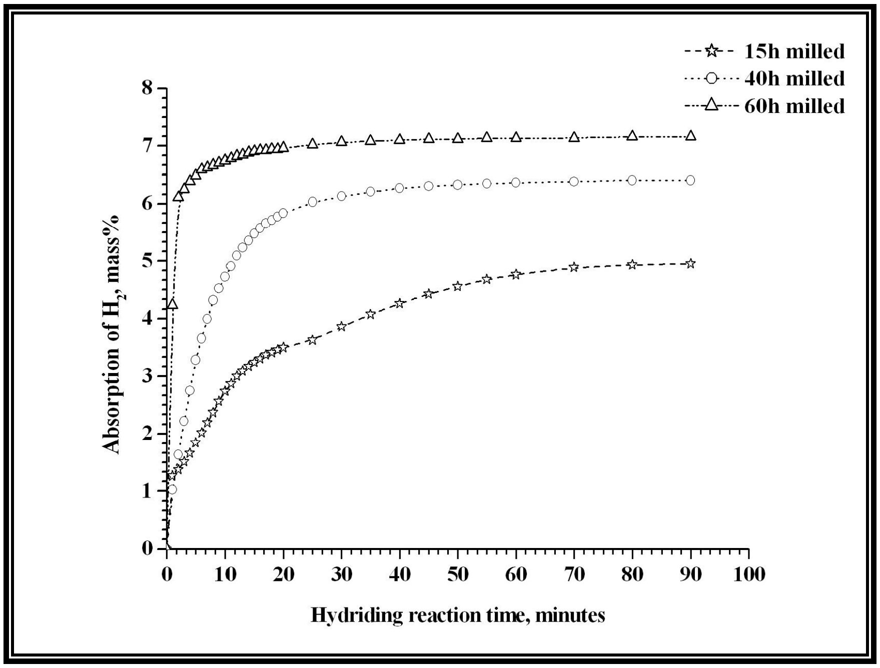

Fig. 4.43: Charging kinetics curve of MZ2 coded composition for different milling times

Fig. 4.44 presents the kinetics plots for the hydriding reaction of 40h milled alloys at different (Zr–Mn) concentrations charged at 200 °C with an initial hydrogen pressure of 30 bars. Note that the alloy coded MZ2 shows highest absorption of about 6 wt%. Further, the hydrogen storage capacity is dramatically decreased, when Zr–Mn concentration is increased or decreased with reference to 5 at% of (Zr–Mn).

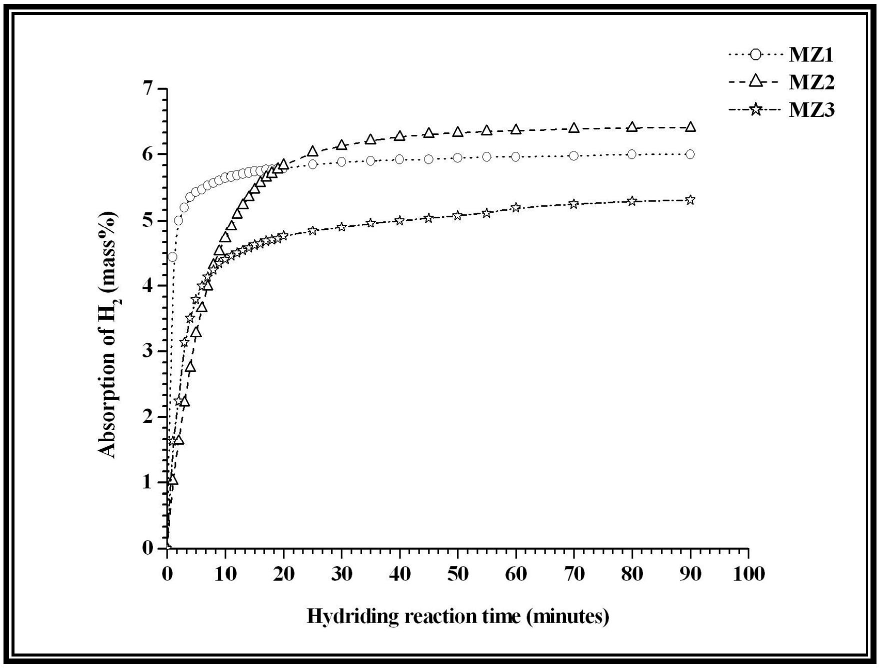

Fig. 4.44: Charging kinetics curve for different Mg–Zr–Mn–Ni compositions

Fig. 4.45 presents the kinetics plots of the hydriding reaction of the synthesized MZ1, MZ2 and MZ3 (40h milled) alloy compositions, at different hydriding temperatures. Note that as the hydriding temperature is increased, the maximum hydrogen absorption capacity increases.

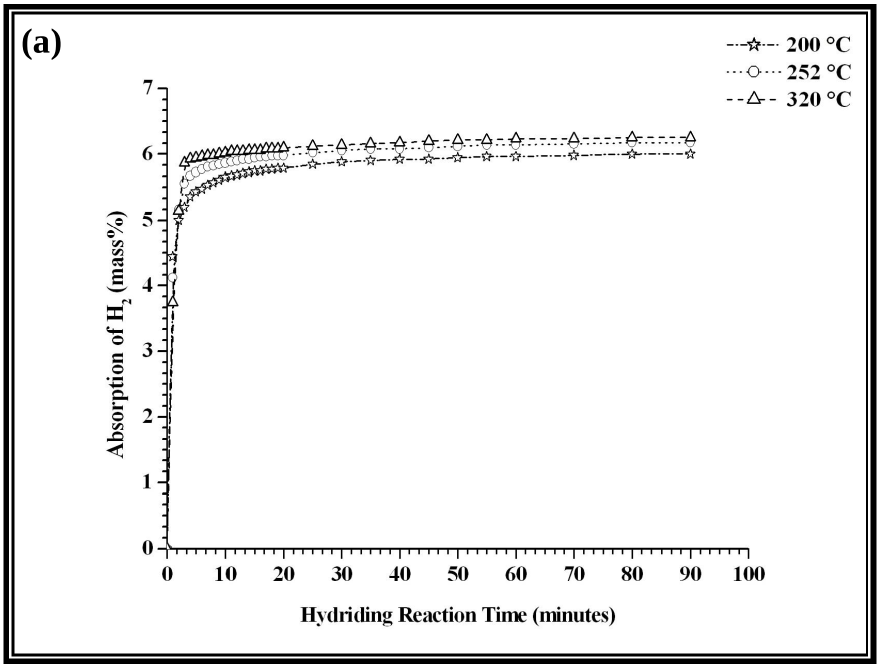

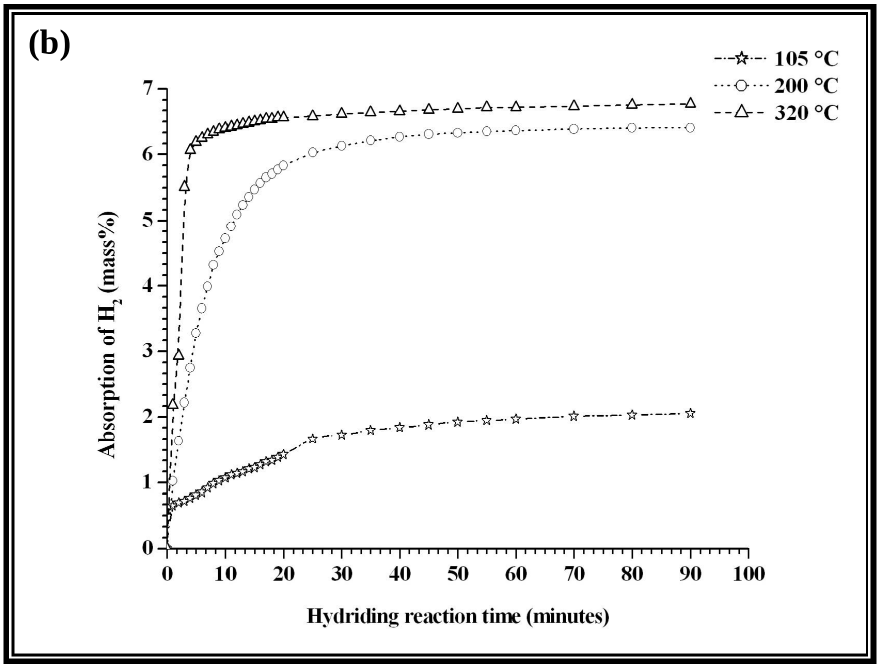

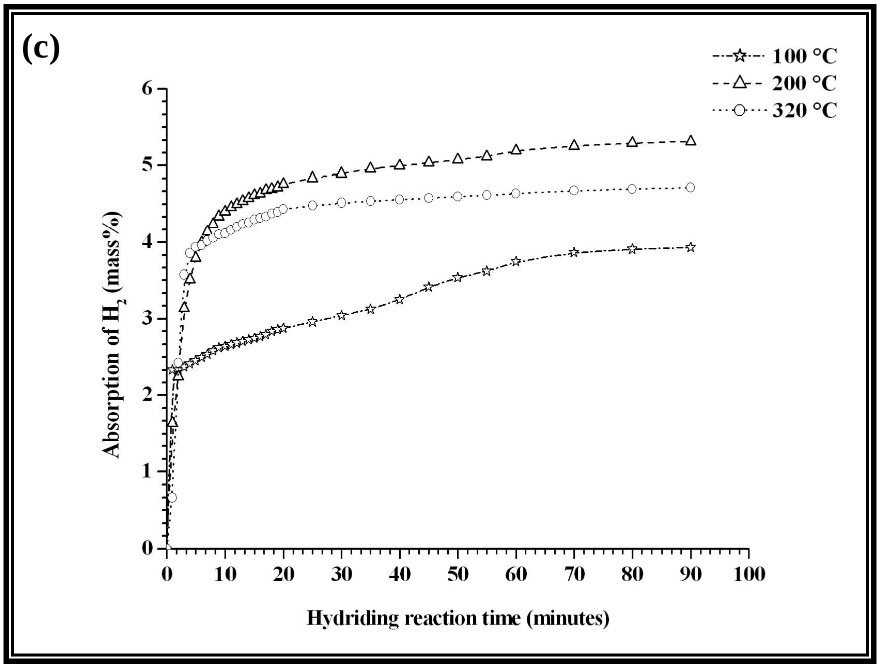

Fig. 4.45: Charging kinetics of the different Mg–Zr–Mn–Ni compositions: (a) MZ1, (b) MZ2 and (c) MZ3

The MZ1 coded alloy composition indicates very high reversible hydrogen storage capacity (greater than 7 mass% of hydrogen stored reversibly at a charging temperature of 201 °C) and this is shown in Fig. 4.46. This graph clearly shows that 95% of hydrogen is absorbed within the first 6 to 10 minutes. The fast charging and discharging is clearly associated with presence of Zr and Mn catalytic action as reported by Majchrzycki et al [14] and Zaluska et al [17]. Similarly, Fig. 4.47 shows the kinetics plots of the dehydriding reaction of the synthesized MZ1, MZ2 and MZ3 (40h milled) alloy compositions at different dehydriding temperatures. This graph clearly indicates that the mass% of desorbed hydrogen increases with dehydriding temperature [25].

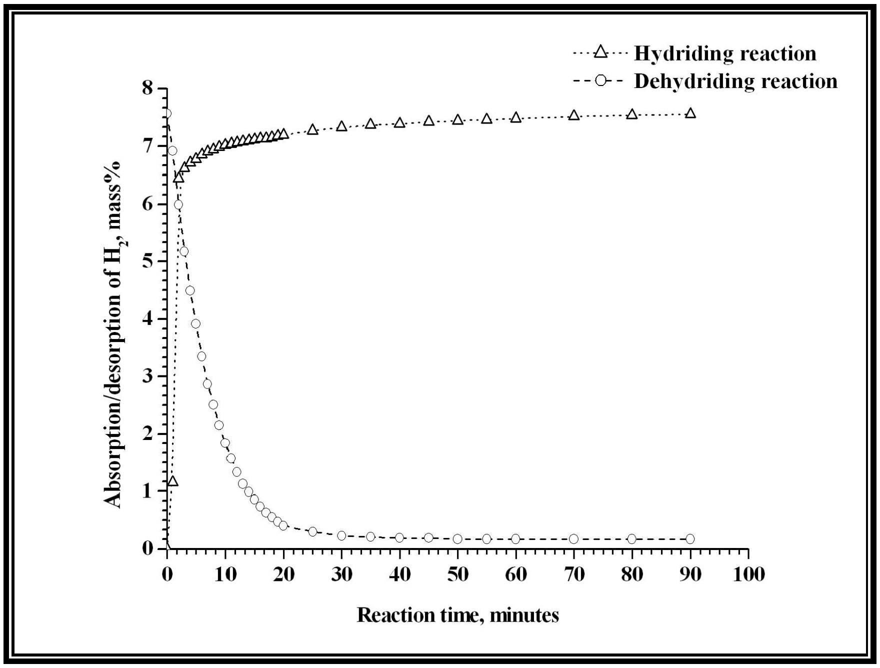

Fig. 4.46: Absorption/desorption kinetics of MZ1 coded composition

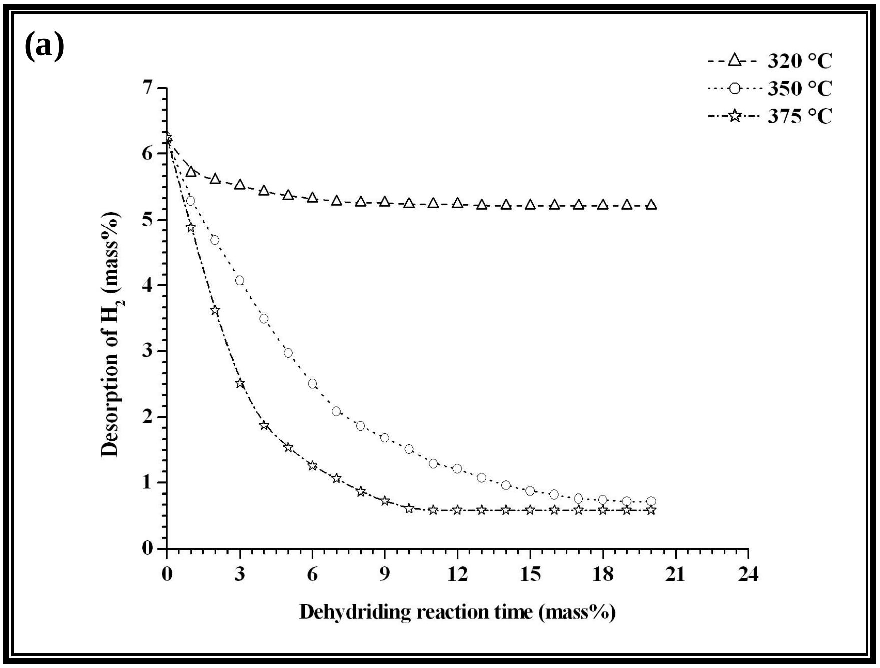

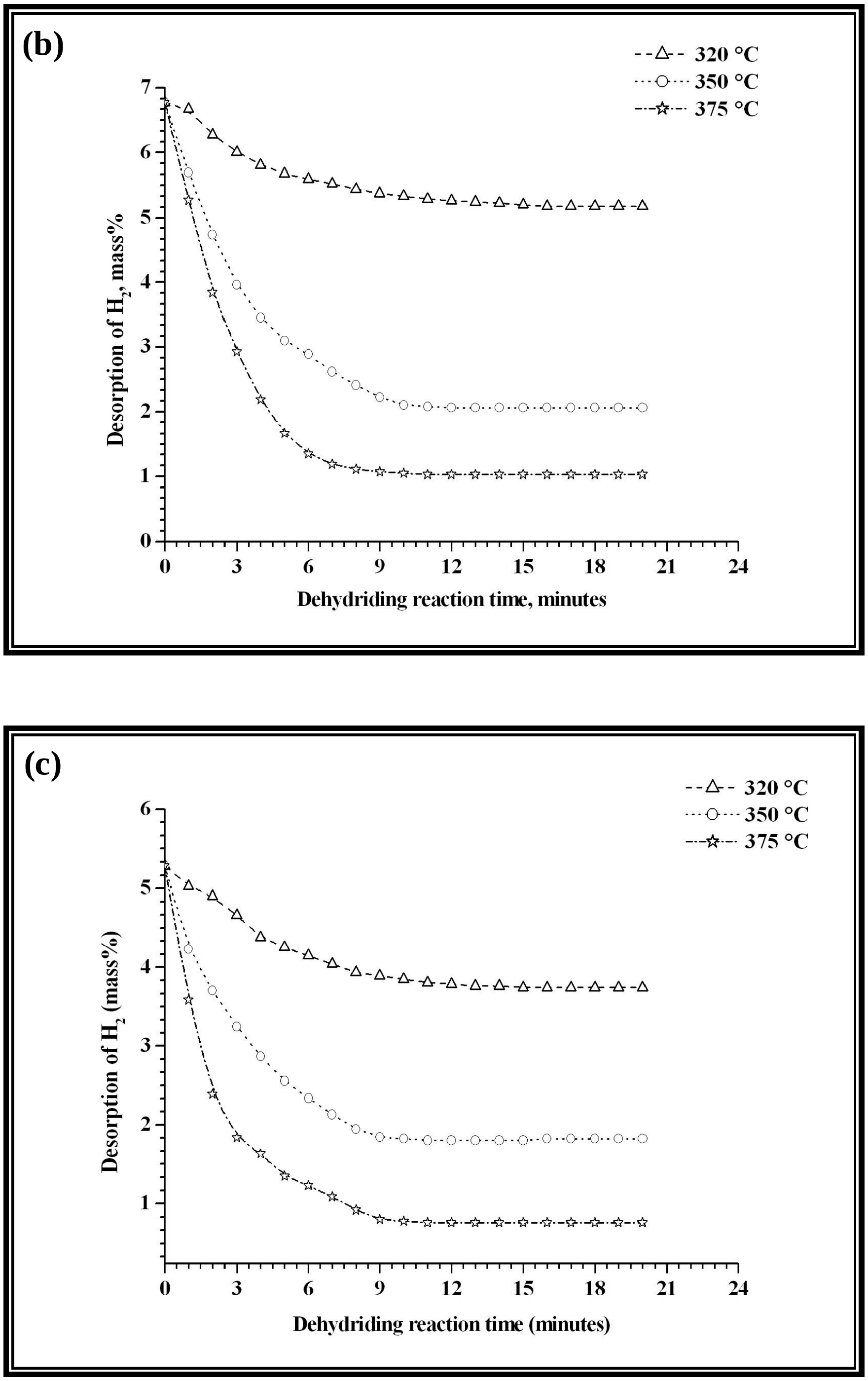

Fig. 4.47: Discharging kinetics of the different Mg–Zr–Mn–Ni compositions: (a) MZ1, (b) MZ2 and (c) MZ3

4.5.4 Deviations in Hydriding and Dehydriding Kinetics due to Departure from Ideal Gas Behavior of Hydrogen

In Fig. 4.48(a), the mass% of hydrogen absorbed versus time data, computed using the ideal gas equation and also with the three real gas equations of state is presented for the optimized MZ2 coded composition. For this alloy, the maximum absorption capacity is computed as 6.36 mass% using the ideal gas equation, and 6.15, 6.09 and 6.07 mass% using Van–der–Waal, Redlich–Kwong and Redlich-Kwong-Soave equations, respectively. The percent deviations from ideal gas computations are plotted as a function of time in Fig. 4.48(b). The percentage deviations in the hydriding kinetics data are obtained as 3.32 %, 4.24 % and 4.61 % for Van–der–Waal, Redlich–Kwong and Redlich–Kwong–Soave equations, respectively. Clearly, significant deviation occurs in predicting the reacted mass of hydrogen using the ideal gas model.

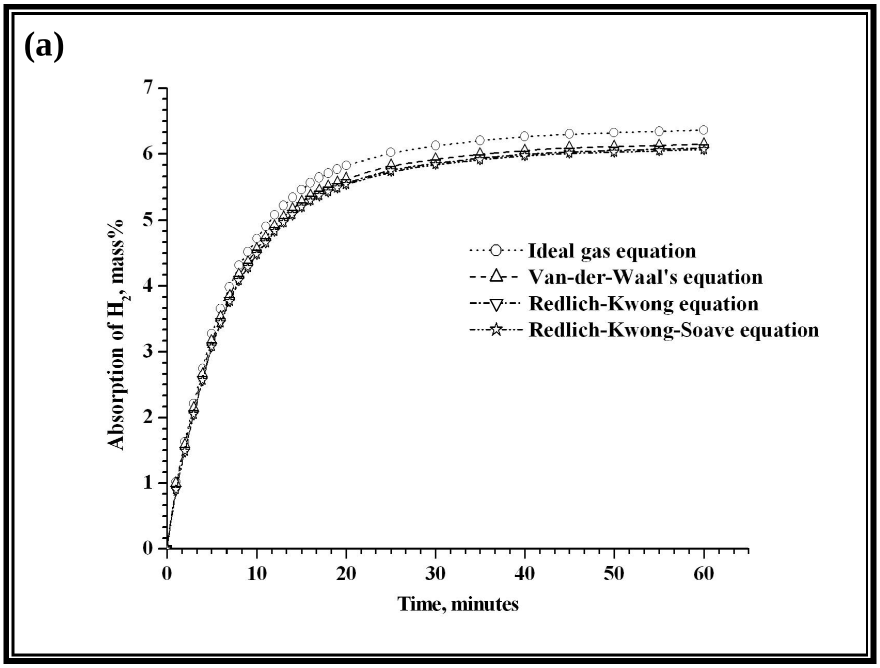

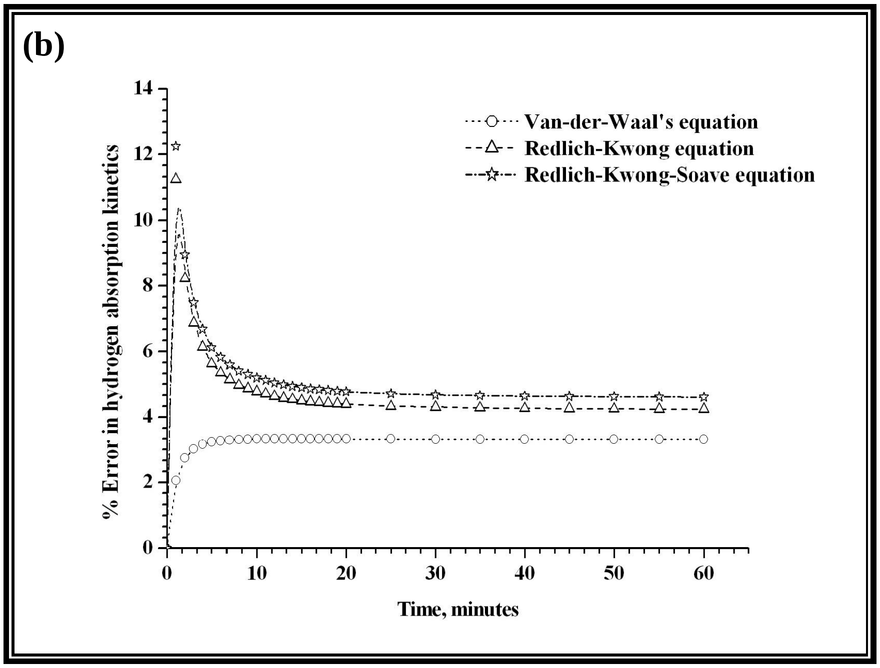

Fig. 4.48: Hydriding characterization of MZ2 coded alloy composition using ideal and real gas equations: (a) H_2 absorption versus time and (b) Deviation in absorption from ideal gas equation

In Fig. 4.49(a), the mass % of hydrogen desorbed versus time data is computed using the ideal gas model along with the three real gas equations of state for the optimized MZ2 coded composition. For this composition, the maximum desorption capacity is computed as 5.75 mass% using the ideal gas equation and 5.74, 5.74 and 5.71 mass% using Van–der–Waal, Redlich–Kwong and Redlich–Kwong–Soave equations, respectively. The percent deviations are plotted as a function of time in Fig. 4.49(b). The percentage deviation of hydrogen desorption using ideal gas equation with respect to the three real gas equations are obtained as 0.16 %, 0.16 % and 0.71 % for Van–der–Waal, Redlich–Kwong and Redlich–Kwong–Soave equations, respectively. However, this deviation due to the ideality assumption is smaller than that obtained for the absorption kinetics

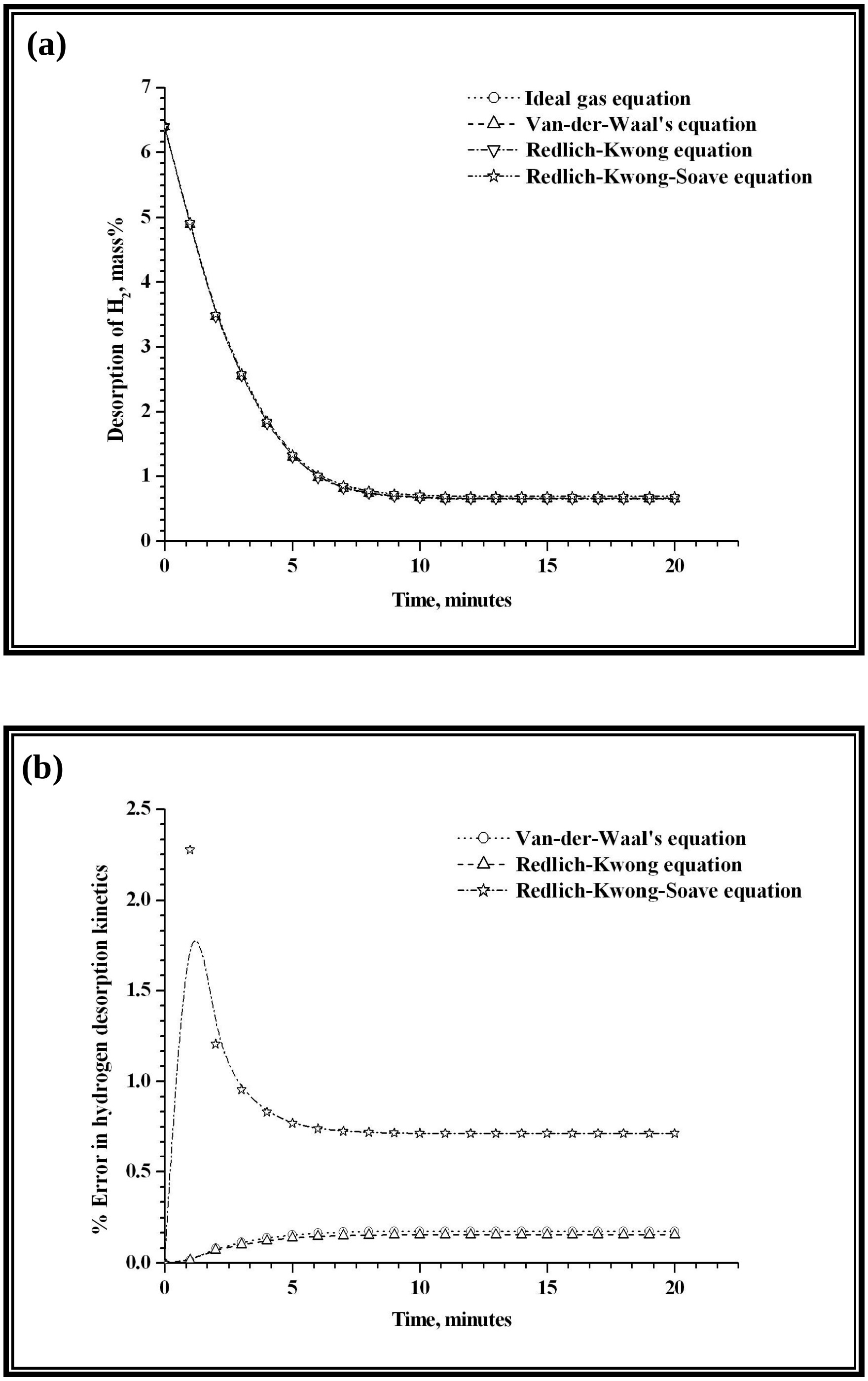

Fig. 4.49: Dehydriding characterization of MZ2 Coded alloy composition using ideal and real gas equations: (a) H_2 desorption versus time and (b) Deviation in desorption from ideal gas equation

4.5.5 Reaction Kinetics Modelling Analysis

The experimental data of the optimized MZ2 coded alloy composition at 210 ºC is first modelled using a first-order lumped exponential response model of the form presented in chapter 2 (section 2.5.1, Eqns. 2.16 and 2.20). The experimental constants in these two equations are determined using linear regression and predictions of the estimated models are compared with experimental data in Fig. 4.50(a) and (b). For the charging model, the estimated values of the constants are determined as: $\hat{\alpha}_c = 6.37$ & $\hat{\beta}_c = 0.13$, with coefficient of correlation obtained as:

$$\left(R_0^2\right)_{Charging} = 0.98 \qquad \text{---------------------} \tag{4.25}$$

Similarly, for the discharging model, the estimated constants are determined as: $\hat{\alpha}_d = 6.37$ & $\hat{\beta}_d = 0.33$, with coefficient of correlation obtained as:

$$\left(R_0^2\right)_{Discharging} = 0.96 \qquad \text{--------------------} \tag{4.26}$$

These high values of coefficient of correlation indicate that the linear model is able to explain charging as well as discharging data variability.

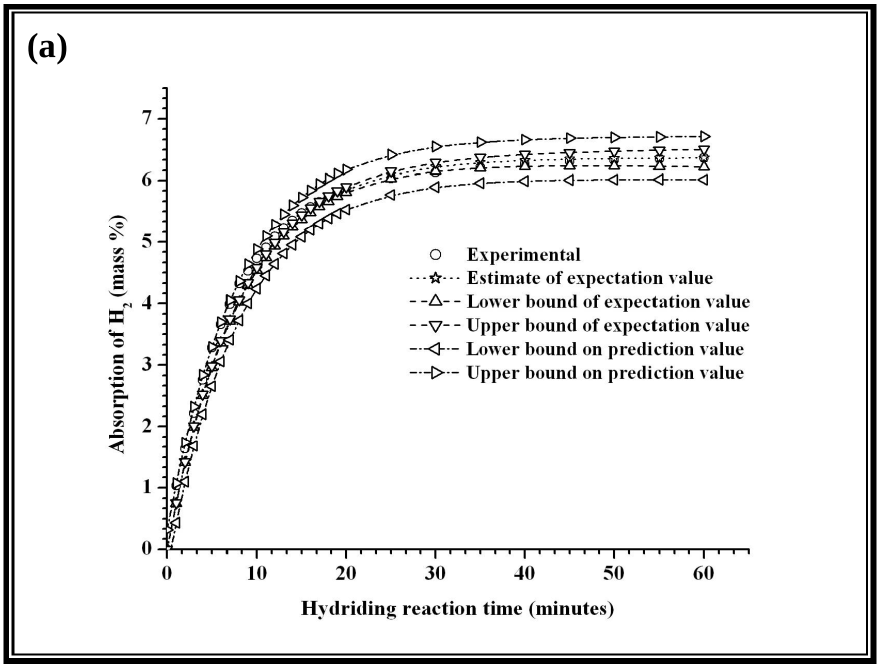

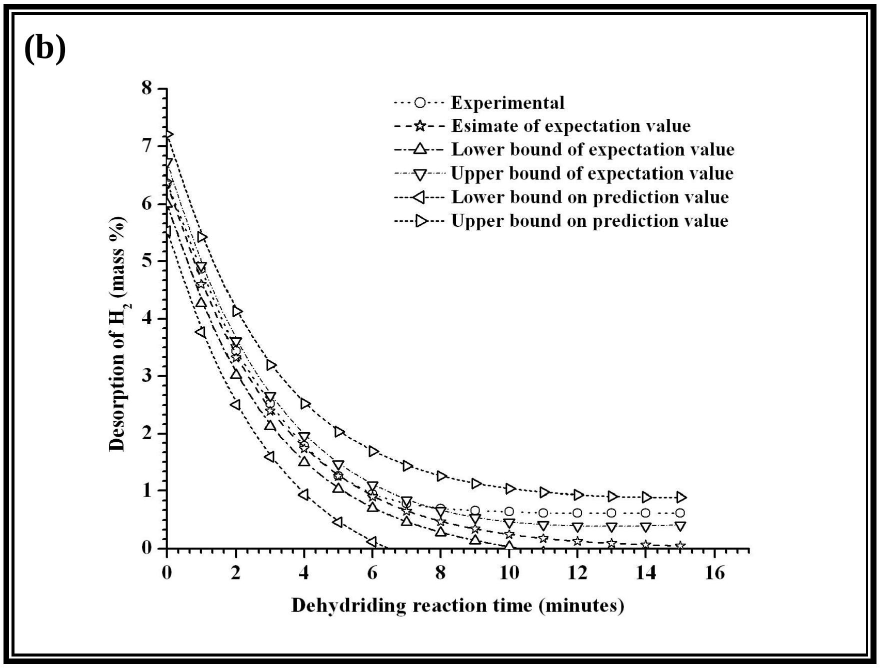

Fig. 4.50: Model fit for experimental data using lumped first order kinetics model for the optimized MZ2 coded composition: (a) Charging kinetics and (b) Discharging kinetics

Shrinking core model applies for fitting the hydrogen absorption data for optimized MZ2 composition at 210 ºC. Equations described in chapter 2 (section 2.5.2, Eqns. 2.22, 2.23 and 2.24) are compared with the experimental results in Fig. 4.51(a). This graph indicates that the full form, shrinking core model, given by Eq. (2.22) gives a better estimation of the experimental data. However, clearly both the individual pure chemical and diffusion control models (simplified models) are not adequate to characterize the experimental data. For the purpose of fitting the full Shrinking core model, a numerical statistical factorial experiment in the dimensionless space of t^*, ϕ_1 and ϕ_2 has been used. Using a minimum variance non-linear optimization scheme, the best fit corresponding to mass transfer coefficient in gas phase, k_α of 0.5×10^{-6} m/s and reaction rate constant, k_r of 16×10^{-6} m/s have been obtained. For this optimization, value of the diffusion coefficient through species βH_2 of α, D_P is taken as 9.77×10^{-9} m^2/s (reported by Nishimura et al [21]) and mean radius of spherical particles, r_p as 4.18×10^{-6} m (measured using SEM).

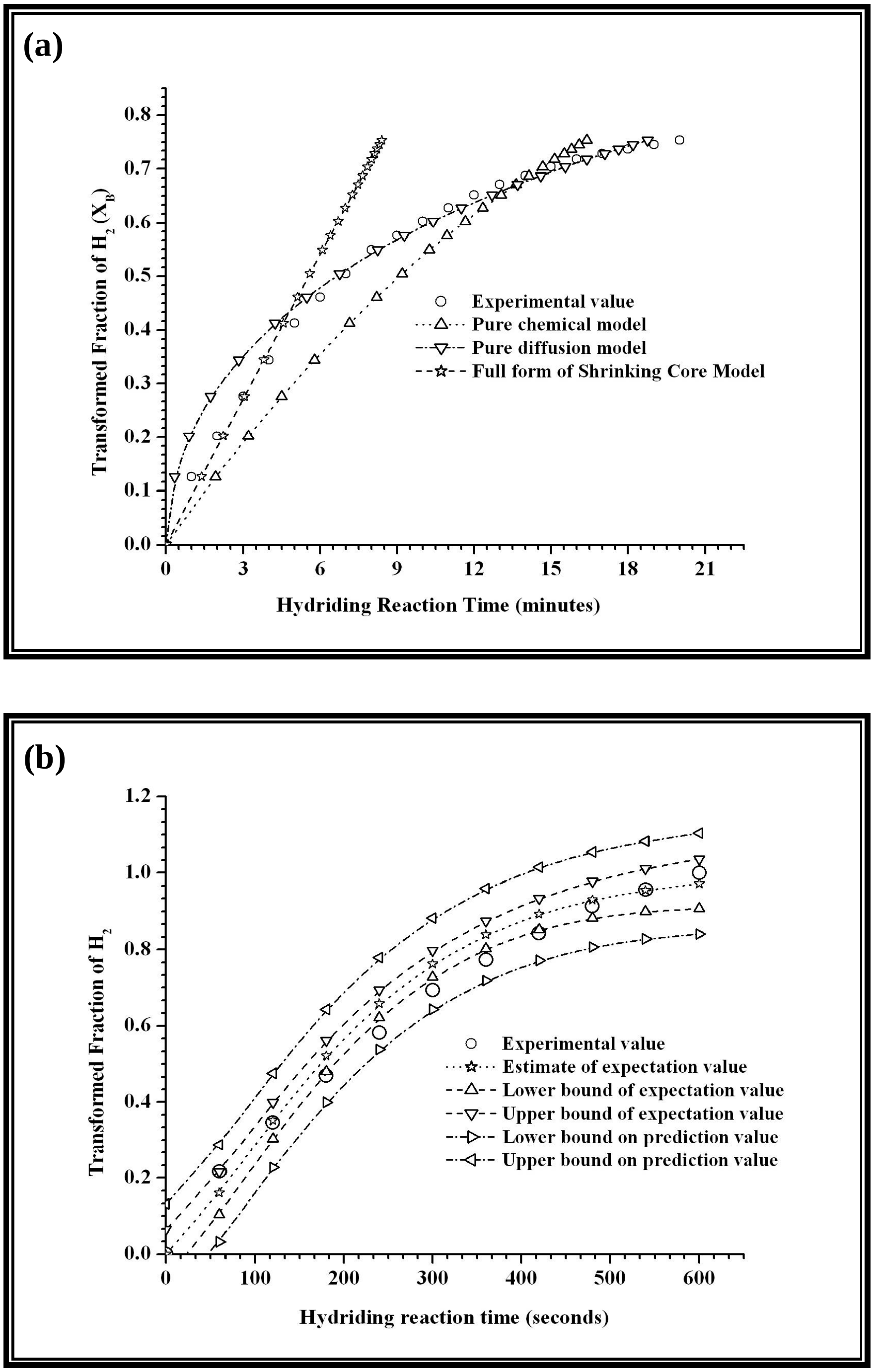

Fig. 4.51: Model fit for experimental data using different model for the optimized MZ2 coded composition: (a) Shrinking core model and (b) Johnson–Mehl–Avrami model

In Fig. 4.51(b), the Johnson–Mehl–Avrami (JMA) model represents a generalized case of random nucleation and growth in the optimized MZ2 coded composition. In the JMA model, nucleation occurs randomly. The JMA equation has been given in chapter 2 (section 2.5.3, Eqns. 2.25 and 2.26). However, for the JMA full linear regression model, a co-efficient of correlation, R^2 is obtained as 0.9771, and Avrami exponent, n as 1.31. Note also that in about 300 s, the transformed fraction of the hydride reaches about only 69 %.

4.5.6 Prediction of Formation Enthalpy and Entropy

The formation of enthalpy and entropy during dehydriding reaction are estimated by Van't Hoff relation, which is detailed in chapter 3. Using Van't Hoff relation, the enthalpy of formation (ΔH_0) of the optimized MZ2 (40 h milled) composition is determined as 80.9 kJ/mole of H_2, and the entropy (ΔS_0) is computed as 128.5 J/mole of H_2 K. Using the experimental results and statistical error expressions, the uncertainty associated with enthalpy is obtained as 8.2 % and uncertainty associated with entropy is as 5.4 %. Therefore, the enthalpy of formation can be stated as 80.9 ± 6.6 kJ/mole of H_2, and the entropy can be stated as 128.5 ± 6.9 J/mole of H_2 K. The logarithmic plot of equilibrium pressure versus temperature (Van't Hoff relationship) is compared with experimental/obtained values (with the coefficient of correlation, R^2_0 as 0.9931, see Fig. 4.52).

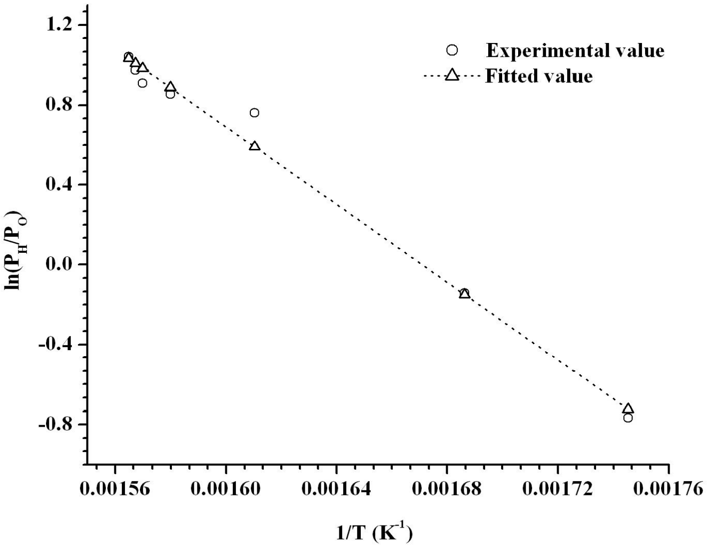

Fig. 4.52: Experimental and derived pressure ratio versus inverse temperature (using Van't Hoff equation) for optimized MZ2 composition

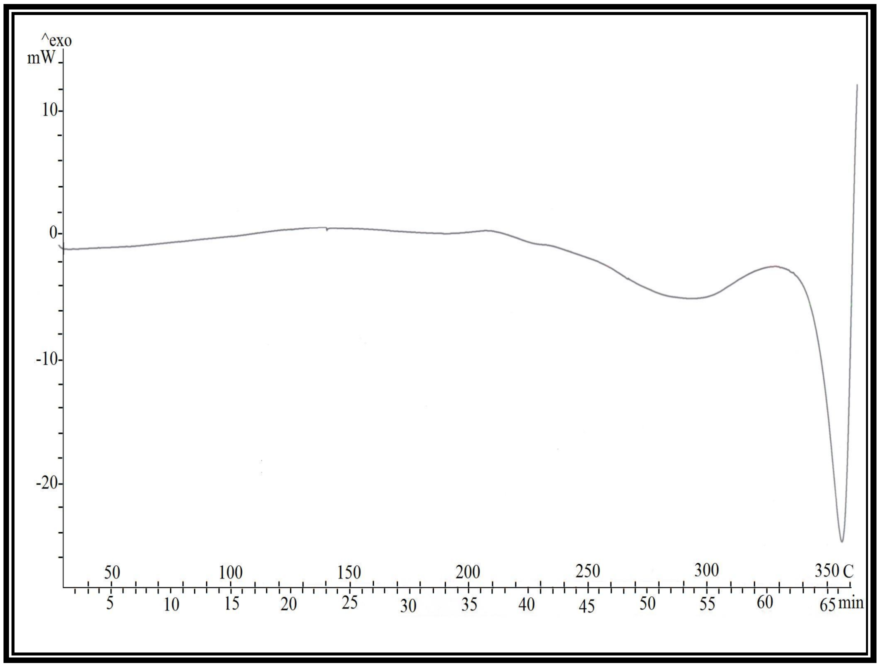

Fig. 4.53: Electrical power absorbed during DSC test versus time/temperature plot for optimized MZ2 coded hydride composition

The experimentally extracted value for $\overline{\Delta H}$ by the DSC method (see Fig. 4.53) is obtained as 74.4 ± 6.1 kJ per mole of hydrogen for hydride optimized MZ2 coded composition. Further, if one assumes the dehydriding reaction in the DSC to be close to equilibrium (which is thermodynamically unlikely), "pseudo specific entropy", $\overline{\Delta S_{pseudo}}$ can be computed as 119.5 ± 6.5 kJ per (mole of H_2) K. It is to be noted that the pseudo entropy is computed under "far from equilibrium" conditions and, hence, is not expected to be close to the entropy obtained using Van't Hoff analysis.

REFERENCES

1. S. R. Ovshinsky, M. A. Fetcenko, B. Reichman, K. Young, B. Chao and J. Im, Electrochemical hydrogen storage alloys and batteries fabricated from Mg containing base alloys, (1997) *Patent No. US5616432*.
2. R. Schulz, J. Strom-Olsen, L. Zaluski and A. Zaluska, Nanocrystalline Mg or Be based materials and use thereof for the transportation and storage of hydrogen, (1999) *Patent No. US5964965*.
3. S. R. Ovshinsky and R. T. Young, High storage capapcity alloys enabling a hydrogen based ecosystem, (2001) *Patent No. US6193929B1*.
4. M. A. Fetcenko, Mg–Ni hydrogen storage composite having high storage capacity and excellent room temperature kinetics, (2007) *US patent*.
5. J. H. Shim, S. A. Jin and Y. W. Cho, Method for fabricating magnesium based hydrogen storage material, (2007) *Patent No. 2011/939636*.
6. P. S. Yen, C. J. Huang, J. R. Ku, B. H. Chen, M. S. Jeng, F. Tsau, S. C. Lo and T. Chen, Nanotization of magnesium based hydrogen storage material, (2010) *Patent No. 2010/0044478*.
7. Suleyman Er, Hydrogen storage materials: a first principles study, *Pd. D. dissertation* (2006) 29 – 44.
8. E. Enescu, P. Lungu, I. Pasuk and G. Stoian, J. *of Optoelectronics and Advanced Materials,* **8 (2)** (2006) 699–701.
9. M. Kandavel and S. Ramaprabhu, Hydrogen absorption properties of Mg-based composite materials, *International symposium of research students on material science and engineering, December 20-22, 2004, Chennai, India.*
10. M. A. Fetcenko, K. Young, C. Tung and S. R. Ovshinky, Catalyzed hydrogen desorption in Mg based hydrogen storage material and methods for production thereof, (2005) *Patent No. US2005/0126663A1*.
11. K. Sapru, L. Ming and S. Ramachandran, Magnesium mechanical alloys for thermal hydrogen storage, (1999) *Patent No. US591381*.
12. K. G. Bambhaniya, G. S. Grewal, V. Shrinet, N. L. Singh and T. P. Govindan, Kinetic Study of Nano–Structured Mg_2Ni Alloy for Safe Hydrogen Storage, *International Conference and Workshop on Nanostructured Ceramics and Other Nanomaterials (ICWNCN–2012),* March 13 – 16, 2012, University of Delhi, India (poster presented).

13. Z. Dehouche, R. Djaozandry, J. Goyette and T. K. Bose, *J. of Alloys and Compounds,* **288** (1999) 312–318.
14. W. Majchrzycki, E. Jankowska, M. Nowak, I. Okonska and M. Jurczyk, Amorphous Mg–Ni–M type alloys as a hydrogen source in fuel cells, 5th advanced batteries and accumulators – ABA – 2004.
15. T. Spassov, V. Rangelova, P. Solsona, M. D. Baro, D. Zander and U. Koster, *J. of Alloys and Compounds,* **398** (2005) 139–144.
16. K. G. Bambhaniya, G. S. Grewal, V. Shrinet, N. L. Singh and T. P. Govindan, Synthesis & Reaction Kinetics of an Mg–Ni–Fe–Mn Alloy System for Hydrogen Storage, *J. of Chemical Engineering Communication (communicated).*
17. A. Zaluska, L. Zaluski and J. O. Strom–Olsen, *J. of Alloys and Compounds,* **288** (1999) 217–225.
18. M. V. Lototsky, *Int. J. of Energy Research,* **33 (13)** (2009) 1114 – 1125.
19. K. G. Bambhaniya, G. S. Grewal, V. Shrinet, N. L. Singh and T. P. Govindan, Synthesis, Characterization and Reaction Kinetics of Nano–Structured Mg–V–Ni Composites for Solid–State Hydrogen Storage, *Int. J. of Energetic Materials and Chemical Propulsion (communicated).*
20. K. G. Bambhaniya, G. S. Grewal, V. Shrinet, N. L. Singh and N. J. Buch, Rationalization for Use of Ideal Gas Law Analysis in Optimizing Solid State Alloys for Hydrogen Storage, *Int. J. of Applied Chemistry (communicated).*
21. C. Nishimura, M. Komaki and M. Amano, *J. of Alloys and Compounds,* **293–295** (1999) 329–333.
22. K. G. Bambhaniya, G. S. Grewal, V. Shrinet and N. L. Singh, Study on Synthesis and Reaction Mechanisms of Doped Mg based Nano–Structured Solid State Hydrides, *International conference proceeding as 2011 World Congress on Engineering and Technology, Oct. 28 – Nov.2, 2011, Shanghai, China,* IEEE, **04** (2011) 172–175.
23. T. Ma, Y. Hatano, T. Abe and K. Watanabe, *J. of Alloys and Compounds,* **372** (2004) 251–258.
24. K. G. Bambhaniya, H. I. Patel, G. S. Grewal, V. Shrinet, T. P. Govindan, and N. L. Singh, “Synthesis and Absorption/Desorption Study on Mg–Pd–Ni Compisitions as a Solid Solution for Hydrogen Storage” (*prepared*).
25. K. G. Bambhaniya, G. S. Grewal, V. Shrinet, N. L. Singh and T. P. Govindan, *Int. J. of Hydrogen Energy,* **37** (2012) 3671–3676.